High resolution UV spectroscopy and laser-focused nanofabrication

High resolution UV spectroscopy and laser-focused nanofabrication

een wetenschappelijke proeve op het gebied van
de Natuurwetenschappen, Wiskunde en Informatica

Proefschrift

ter verkrijging van de graad van doctor
aan de Radboud Universiteit Nijmegen,
op gezeg van de Rector Magnificus prof. dr. C.W.P.M. Blom,
volgens besluit van het College van Decanen
in het openbaar te verdedigen op
donderdag 8 september 2005,
des namiddags om 1.30 uur precies

door

Grzegorz Myszkiewicz

geboren op 29 mei 1974
te Warschau, Polen

to my beloved wife Monika and our daughter Izabela

Forword

In this thesis I describe my adventures with the applications of narrow-band UV lasers to the High Resolution Laser Induced Fluorescence Spectroscopy (LIF) of small aromatic molecules and with use of Laser Focusing of atoms for Nanofabrication. There are many aspects which connect these two, at first sight very different, techniques. Most importantly, the exited electronic states of the molecules and the atoms used in both experiments have similar lifetimes (on the order of nanoseconds), which result in similar natural linewidths of their electronic transitions (several MHz). This dictates the needed high spectral resolution and consequently similar equipment requirements for both LIF and the manipulation of atoms. However, not only the laser parts are alike, but also both experiments make use of molecules or atoms in the gaseous state under clean high vacuum conditions. In the LIF experiments a molecular beam is created from a supersonic expansion, while a thermal atomic beam is used in the laser-focused nanofabrication experiments.

Obviously, there are also differences between these two techniques. The main is the aim of the experiments. In the high resolution LIF spectroscopy we want to study a variety of molecular properties. The manipulation of atoms to grow solid-state materials is the purpose of the laser-focused nanofabrication. This possibly leads to new photonic or magnetic nanostructures. Other differences arise from different specific requirements of each of the techniques. For example, the manipulation of atoms requires stabilization of a single frequency laser to an absolute frequency reference, such as for example an atomic transition. On the other hand the high resolution LIF relies on both the absolute frequency as well as accurate relative frequencies over a whole frequency region. The relative frequency scale is obtained from interference fringes from a temperature-stabilized, pressure-sealed Fabry-Perot interferometer. The absolute frequency is derived from a high resolution iodine spectra. Other differences will become apparent in the introductions to both experiments.

In the first part of my thesis, Chapters $1 - 6$, with its introduction in Chapter 1 I present my research on small aromatic molecules studied by high resolution LIF spectroscopy. The main motivation for these studies was to get better insight into the structure in both electronic states of the studied molecules and other properties like the lifetime of the excite state, the transition dipole moment, the influence of the floppy parts of molecules on the overall rotation and the different dynamical processes that occur after absorption of a photon. In particular it was interesting to investigate the structure of the weakly bound van der Waals complexes of tetracene with rare gas atoms (Chapter 2) and of the water complex of 4-methylphenol (also known as p-cresol, Chapter 4). The internal rotation effects of the floppy methyl group were inspiring for the o-, m-cresols (Chapter 3) and 4-methylphenol (Chapter 4) as well as the biological importance of resorcinol (Chapter 5) with its similarity to phenol. At

last, but not least, the long ongoing debate on the connection between the structure of 4,4'-dimethylaminobenzonitrile (DMABN) in the excited electronic state and its 'unusual' fluorescence spectrum has led to a paper that for the first time gives the basis for the explanation how the dual fluorescence mechanism may be linked to the DMABN excited electronic state structure (Chapter 6).

The second part of this thesis has arisen from the collaboration with Erich Jurdik and the Solid State Physics Department. It has its own introduction in Chapter 7. In this second part we try to push the limits of the laser-focused nanofabrication technique to obtain a quasicrystal pattern of chromium (Chapter 8) and to extend the method to another technologically important material – iron (Chapter 9). In particular the quasiperiodic structures, if perfected, could lead to the development of photonic materials with a complete photonic band gap, even for materials with low refractive index. The extremely coherent iron nanolines are an important step towards the fabrication of periodic magnetic nanostructures, which can aid the studies of magnetic interactions, switching behavior and may lead to novel phenomena like magnetic photonic band gaps. They might also be applied to future magnetic data storage at ultra-high densities.

CONTENTS

Introduction to rotationally resolved ultraviolet experiments in molecular beams

"The idea that molecules have well-defined shapes is surely the most pervasive idea in chemistry. [...] In brief, a detailed understanding of molecular shapes explains virtually all of chemistry! The development and elaboration of such a widely useful idea is surely the greatest accomplishment of chemical theory. Naturally, almost all branches of chemistry now devote their efforts to obtaining even more detailed accounts of the distribution of atoms in space."

<div align="right">

Carl Trindle, 1980.
Isr. J. Chem. **19**, 47

</div>

1.1   Introduction

I came across the quote from an article by Carl Trindle, while reading David Pratt's review on "High resolution spectroscopy in the gas phase" [1]. The Trindle and Pratt articles certainly give good arguments why scientists wanted to study structures of molecules, defined as the distribution of atoms in space. Not surprisingly, due to very many ways atoms can combine into a chemical entity, we are still studying the molecular structures. In the last decades much progress has been made to refine and develop high resolution experimental techniques, as well as in the ways to analyse the spectra. We increasingly see the need to treat larger molecules, ultimately aiming at biological macromolecules, like proteins, enzymes, DNA-chains, ... Although, at present this is still a dream, we try to approach it by studying small biomolecules or molecules that closely resemble in molecular shapes the biologically important species as well as biomimetics. In this way we hope that the small building blocks, after being

Table 1.1: Doppler $\Delta\nu_D$ and pressure (collision) broadening $\Delta\nu_p$ of the pure rotational transition $18_{6,12} \leftarrow 17_{6,11}$ in microwave (MW) region and one of the rovibronic transitions from $S_1 \leftarrow S_0$ transition in the UV ($\nu = 36009.60$ cm^{-1}), both for resorcinol A molecule. The average distance between the single transitions in the spectrum $< \Delta\nu_n >$ is also given. All numbers are in MHz, except for pressure expressed in mBar. $T = 20$ °C. $M(\text{resorcinol}) = 110$ a.m.u..

transition	ν	ν_D	$< \Delta\nu_n >$	p	$\Delta\nu_p$ [a)]
$18_{6,12} \leftarrow 17_{6,11}$	6.072077×10^4	7.04×10^{-2}	250	1 000	10 000
$S_1 \leftarrow S_0$	1.079568×10^9	1.25×10^3	100	1	10
				0.001	0.01

[a)] Calculated for a typical broadening parameter of 10 MHz/mBar.

connected together, will still retain most of their properties. This will enable us to get a better understanding of the 'big' molecules.

The parameters most directly related to the molecular geometry are principal moments of inertia of the molecule $I_g = \sum_{i=1}^{N} m_i r_{i\perp g}^2$, where m_i and $r_{i\perp g}$ are mass and distance from the principal g axis of atom i, respectively: $g = a, b, c$ and N stands for the total number of atoms. The rotational constants $B_g = \hbar/4\pi I_g$ can be determined from rotationally resolved spectra [2]. It looks very simple, but there are a few major problems with this approach. Firstly, for a non-linear molecule one needs $3N - 5$ rotational constants in order to obtain all molecular parameters (bond lengths and angles). Obviously, already for a very low N, a single rotationally resolved spectrum is not enough to derive all structural information. This can be solved by measuring different isotopomers (isotopically substituted molecules) and assuming that this does not change the electron distribution in the molecule. However, with increasing N the amount of data required for a complete determination of the structure grows rapidly. For example with $N = 20$, one needs 55 rotational constants, obtained from at least 19 different isotopomers. It is clear that the accumulation and analysis of data may be difficult and tedious.

The second problem concerns the experimental resolution. Nowadays, very narrowband, coherent radiation sources are available in a very large part of the electromagnetic spectrum: from klystrons and carcinotrons in the microwave to frequency doubled lasers in the UV. One of the main problems in achieving rotational resolution is determined by the linewidth and the density of transitions. To illustrate this we give an example of the broadening of a pure rotational and rovibronic transition in the resorcinol A molecule (studied in this thesis in Chapter 5). The Doppler $\Delta\nu_D$

and pressure (collision) broadening $\Delta\nu_p$ [2, 3] for different experimental conditions is given in Table 1.1. This table also lists the average distance between single lines in a spectrum $< \Delta\nu_n > =$ (spectrum span)/(No. of transitions). The value of $< \Delta\nu_n >$ indicates the minimum resolution required to resolve single transitions. From the table it is immediately apparent that under ambient conditions both, a pure rotational spectrum in the MW and a rovibronic spectrum in the UV have insufficient resolution. The first is limited by $\Delta\nu_p$ and the latter by $\Delta\nu_D$. To improve this situation experimentalists are using low pressure conditions in the MW (with $p = 1 - 0.001$ mBar), which reduces collision broadening to a few kHz. Another widely used technique both in MW and UV experiments is the application of supersonic expansion in molecular beams. This method strongly reduces Doppler broadening and has an additional advantage to cool the internal degrees of freedom of the molecules so that only the lowest energy levels are populated and therefore reduces the complexity of the spectra. If the laser beam crosses the molecular beam perpendicularly, a (transversal) Doppler broadening of ~ 1 MHz can be achieved even for UV transitions [3]. Other Doppler-free techniques like saturation, polarization and multiphoton spectroscopy can also be applied to obtain the sub-Doppler resolution, but fall outside the scope of this thesis [3].

One other important limiting factor can be the natural linewidth of a level $(\Delta\nu_L)$ determined by its lifetime τ $(\Delta\nu_L = 1/(2\pi\tau))$. In MW experiments the lifetimes of the states are very long and hence do not contribute to a broadening of transitions. However, in UV experiments the excited state lifetimes are typically of the order of ns, which corresponds to a linewidth of several MHz. The lifetimes of electronically excited states can be shortened due to many different non-radiative decays, such as Intersystem Crossings and Intra Vibrational Relaxation, which broaden the experimental linewidths. For more information the reader is referred for example to Ref. [2, 3].

An important issue is the analysis and assignment of the rotationally resolved spectra. From the discussion at the beginning of this section one can expect that many complicated spectra have to be analyzed. For example, a UV spectrum under optimal experimental conditions possesses easily 600 rotational transitions. In many cases the spectra are further complicated by internal rotations of the floppy parts of the molecules (see Chapter 3, 4 and 6), by vibrational Coriolis couplings, centrifugal distortions and other effects [2]. For example, the complicated UV rovibronic spectra of DMABN ($N = 21$) contain over 5 000 lines (Chapter 6). Additionally, isotopomers of the same molecule are often sharing the same spectral regions, which also leads to a high congestion of the rotational spectrum (Chapter 5). Yet another complication is the fact that with increasing mass of the molecule, its rotational constants decrease, which inevitably leads to an extremely congested rotational spectra. It is obvious that the 'classical' analysis (assigning quantum numbers to most of the transitions in the spectrum) becomes very difficult and tedious, if not impossible. It is clear that

there is a need for automated ways to assign the spectra.

In an attempt to solve this problem the group of Neusser [4] has developed a procedure, which directly fits the experimental data, without prior assignments. This method, which is called 'correlation automated rotational fitting', has been pioneered by Levy and coworkers [5–7], and uses the correlation between the experimental and the simulated spectrum as a measure of the quality of the fit. Unfortunately, the method still has limited applicability. At our university a very versatile automated assignment has been developed that makes use of a genetic algorithm approach (GA) (for details see Section 1.3). It has proven to be very successful and has been applied in the analysis of almost all spectra discussed in this thesis.

1.2   The experimental setup

The apparatus for the rotationally resolved laser induced fluorescence (LIF) is shown in Fig. 1.1. The experimental setup comprises basically of two parts: the molecular beam machine and the laser system [8].

1.2.1   Molecular beam machine

The vacuum part consists of four vacuum chambers: a source with the quartz sample container, buffer I, experimental I and a quadruple mass spectrometer. The molecular beam is formed by seeding the molecules of interest in $\sim$ 600 mbar argon and a subsequent supersonic expansion of the mixture through a $\sim$ 100 μm wide quartz nozzle into the vacuum. In order to increase the vapour pressure of the studied molecules, the source container can be heated up to $\sim$ 500 °C.

The molecular beam from the source chamber is doubly skimmed, at first by the conical skimmer with a $\varnothing$1.5 mm orifice and secondly by a diaphragm with a similar opening. The first skimmer separates buffer I from the source chamber and the second one buffer I from the experimental I chamber. When the molecular beam enters the experimental I section is has a very small transversal velocity spread. In the same chamber, 30 cm from the nozzle, the frequency scanned narrow band UV laser crosses the molecular beam perpendicularly and electronically excites molecules (see Fig. 1.2). The molecules fluoresce back to different rovibrational states of the ground electronic state within typically several nanoseconds.[1] The total fluorescence is collected by collection optics and imaged on a photomultiplier tube. After digitizing with a photon counter the final signal is stored by a computer. In this way the *excitation spectrum* of the molecule is recorded, which under favourable conditions is identical with the absorption spectrum of this molecule. The apparatus allows for an experimental resolution of $\sim$ 15 MHz.

---

[1]The molecules studied in this thesis have lifetimes of the excited electronic state between 1.6 to 26.7 ns
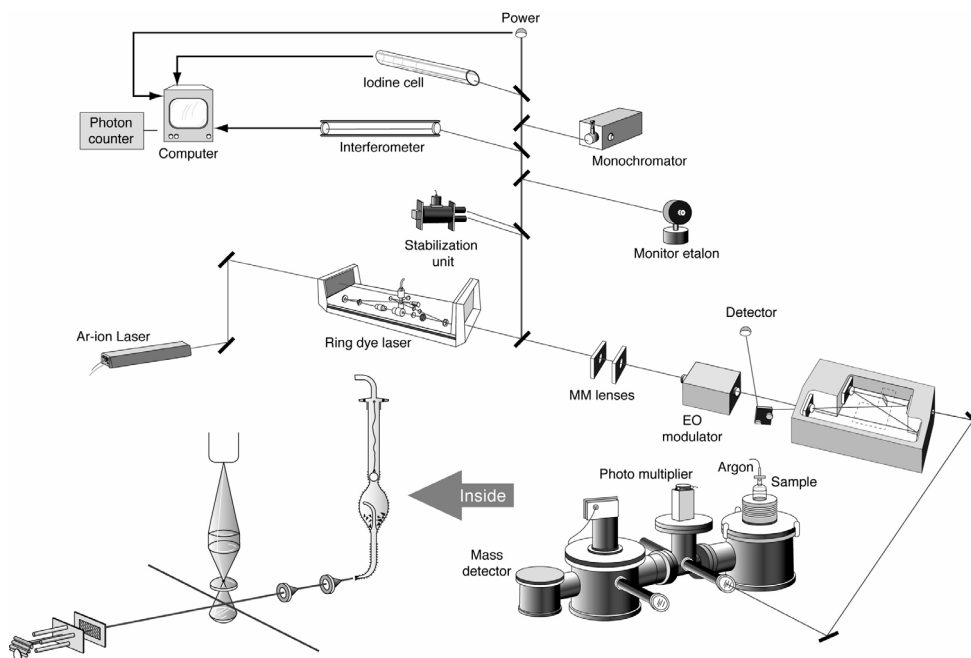
Figure 1.1: The experimental setup used for the high resolution UV measurements. The Ar$^+$ ion laser, ring dye laser and doubling cavity are shown. Also some other equipment used for the frequency calibration, stabilization and monitoring are depicted. On the bottom part of the figure the overall molecular beam machine (on the right) and the inside of this apparatus (on the left) are presented.

Finally, at the end of the system a mass spectrometer serves as a reference for the alignment and optimization of the molecular beam. Typical pressures with the molecular beam on are following: in the experimental I section below 1×10^{-6} mbar and in the mass spectrometer $\sim 1 \times 10^{-9}$ mbar. These conditions assure a collision-free environment during the experiments.

1.2.2   Laser system

The laser system comprises of an Ar$^+$ ion laser, a ring dye laser and an external enhancement resonator for the second harmonic generation (SHG).

The Ar$^+$ ion laser (Spectra Pysics, Stabilite 2016) produces typically 6 W all lines and it pumps a single frequency ring dye laser (a modified Spectra Physics 380D).
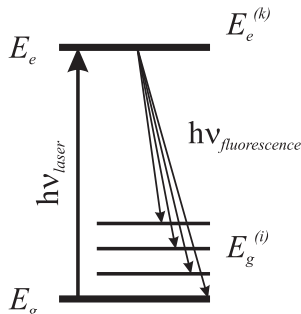
Figure 1.2: Principles of the LIF technique. E_g and E_e designate the ground and excited electronic states, respectively, with their rovibrational level structures $E_g^{(i)}$ and $E_e^{(k)}$.

In order to achieve single frequency narrow band operation, this laser cavity contains a Lyot filter, a thin etalon and a thick (scanning) etalon. Single lasing direction is enforced by a Faraday rotator with a quarter-wave plate ($\lambda/4$). Furthermore, the laser cavity length is actively stabilized to a side of a fringe of a thermally-isolated reference cavity (Fabry-Perot interferometer). Continuous scans of ~ 30 GHz are possible with a pair of Brewster plates in the laser cavity. The linewidth of this laser is estimated to FWHM $\leqslant 4.1$ MHz (Full Width at Half Maximum), based on the doubling cavity measurements presented in Section 1.2.3.

An example of the performance of the ring dye laser operating with dye Rhodamine 110 is presented at Fig. 1.3. The wavelength dependency was obtained by mode-hoping the thin etalon in steps of 900 GHz, which corresponds to ~ 0.9 nm around 550 nm.

1.2.3   External enhancement doubling cavity

One of the aims during this research was to upgrade the ring dye laser from the intra-cavity doubling [9] to UV generation by an external enhancement doubling cavity. This was done in order to decouple the laser from the UV generation step. Another aim was to increase the UV power needed in studies of molecules with weaker fluorescence (e.g. biomolecules) and/or increase the signal to noise ratio in our experiments. The typical UV output power generated in an intra-cavity setup in the wavelength region $\lambda = 265 - 290$ nm was $P_{UV} = 50 - 500$ μW [10–12]. In the following sections it is shown that the external doubling cavity increases the UV power by approximately a factor of 50. Most of the measurements performed with this doubling cavity were taken at a fundamental wavelength $\lambda \sim 550$ nm.
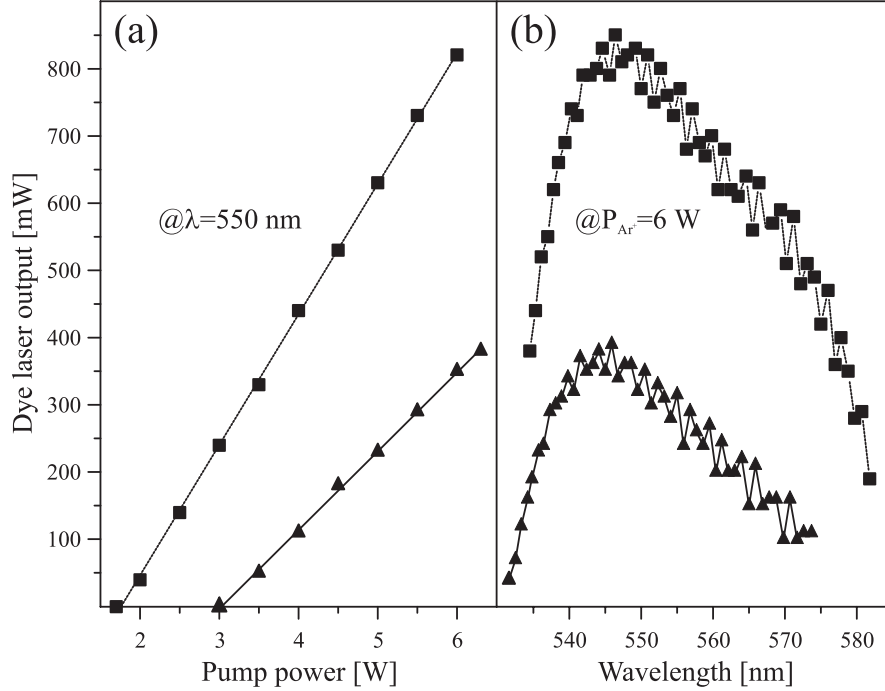
Figure 1.3: Ring dye laser output dependencies on (a) the pump power at the fixed wavelength $\lambda = 550$ nm and (b) the operating wavelength at the fixed pump power $P_{Ar+} = 6$ W. Black squares on the dotted line represent measurements taken with the fresh dye (Rhodamine 110) solution and the triangles on the solid line correspond to the ~ 3.5 months old dye solution.

Theory of second harmonic generation

We assume a plane wave with a frequency ω_i, wave-vector $\mathbf{k}_i$ and an electric field defined as

$$\mathbf{E}_{\omega_i}(t) = \mathbf{E}(\omega_i)e^{i(\omega_i t - \mathbf{k} \cdot \mathbf{r})}. \tag{1.1}$$

If such electromagnetic wave propagates through a medium it can induce a polarization $\mathbf{P}(2\omega)$ that radiates at the second-harmonic of the fundamental frequency ω. This is induced by the nonlinearity of the susceptibility. Here

$$\mathbf{P}(2\omega) = \epsilon_0 \chi^{(2)}(-2\omega, \omega, \omega)\mathbf{E}(\omega)\mathbf{E}(\omega)e^{i[(\mathbf{k}_{2\omega} - 2\mathbf{k}_\omega) \cdot \mathbf{r}]}, \tag{1.2}$$

where $\chi^{(2)}$ is the third rank nonlinear susceptibility tensor for SHG. This tensor has non-vanishing bulk components only in media without inversion symmetry. The
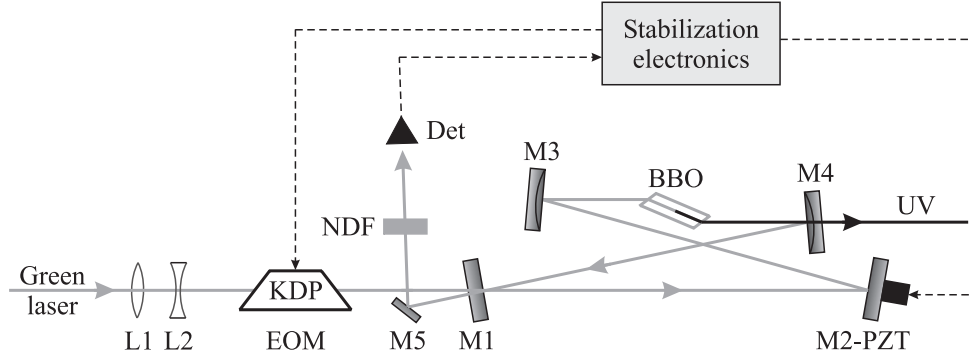
Figure 1.4: Doubling cavity schematics. L_1, L_2 – mode matching lenses; EOM – electro-optic modulator based on the KDP crystal; M_1 to M_4 – doubling cavity mirrors with BBO crystal; M_5 – aluminum coated mirror; NDF – neutral density filter with T = 1%; Det – detector for monitoring the reflected light from the doubling cavity.

macroscopic SHG process requires energy and momentum conservation. The first condition is $2\omega = 2 \times \omega$ and is reflected in the notation of $\chi^{(2)}(-2\omega, \omega, \omega)$. The second is called the phase-matching condition and is written as $\mathbf{k}_{2\omega} - 2\mathbf{k}_\omega = 0$. For the latter relation to be fulfilled the refractive indices at ω and 2ω must be equal: $n(2\omega) = n(\omega)$.

This can only be realized along certain directions in anisotropic crystals and can be achieved by angle tuning of the crystal orientation with respect to the fundamental beam propagation direction or by temperature tuning of the crystal. The first is referred as critical and the second as non-critical phase-matching.

In the nonlinear crystal the 2ω photon is always polarized in the direction that gives it the lowest of the two possible refractive indices. The two fundamental photons can have either the same or orthogonal polarizations. The first is called type I and the second type II phase-matching. The choice of the phase-matching type depends on the nonlinear properties of the chosen crystal.

More details on theory of the SHG process can be found in [13–20].

Realization of doubling cavity

We based the mechanical design of the external doubling cavity and a part of the stabilization on the cavity built by E. Jurdik [21, 22]. The doubling cavity schematics is presented in Fig. 1.4. It is a ring cavity that comprises of four mirrors. The fundamental light at $\sim$ 550 nm is coupled in by the plane M1 input coupler with transmission T $\sim$ 2.1%. The back side of M1 is anti-reflection (AR) coated for

$\lambda \sim 540 - 590$ nm. Mirror M2 is a small, plane mirror, high reflective (HR) coated for $\lambda \sim 540 - 590$ nm and mounted on a piezoelectric transducer (PZT). M3 and M4 are spherical mirrors with a radius of curvature -100 mm, both HR coated for $\lambda \sim 540 - 590$ nm. M4 is a short band pass filter with T $\sim 90\%$ at $\lambda \sim 270 - 295$ nm. M3 and M4 mirrors are tilted with differential screws for fine adjustments.

The output mode of the ring dye laser is mode-matched to the doubling cavity mode by a pair of lenses L1 and L2, with focal lengths of $f_{L1} = -50$ and $f_{L2} = 100$ mm and both AR coated for $\lambda \sim 540 - 590$ nm. Additionally, the L2 is mounted on a translator. The length of the doubling cavity is locked to the wavelength of the ring dye laser by a frequency modulation (FM) technique proposed for microwave oscillators by Pound [23] and extended to optical cavities by Drewer [24]. This technique is preferred over the polarization spectroscopy (PS) developed by Hänsch and Couillaud [25]. The reason is that it has virtually background free stabilization signals, which is very important for long frequency scans.

A Brewster cut, type I critically phase-matched BBO crystal ($BaB_2O_4 - \beta$-barium borate) is used to generate UV between $\lambda = 269 - 282$ nm. The dimensions of the crystal are $4 \times 4 \times 10$ mm^3 (h $\times$ w $\times$ l). The crystal is mounted on a stage, which allows for two angular adjustments and all three translations.

FM spectroscopy

To demonstrate the FM locking technique we present a short introduction to FM spectroscopy. It was pioneered in the early 80's by Bjorklund [26] and Hall [27]. The following discussion is based on the elegant approach developed by Supplee *et al.* [28].

We assume a probe laser beam with frequency ω, phase modulated (for example by an electro-optic modulator) at frequency Ω. The electric field of this wave is given by

$$E(t) = E_0 e^{i(\omega t + M \sin(\Omega t))}, \tag{1.3}$$

with M the so-called modulation index. The phase modulation term can be expanded in a series of n-th order Bessel functions J_n, which describe the different frequency components of the modulated wave spectrum. Subsequently it is assumed that the probe wave passes an absorption feature with spectral width FWHM $= \Gamma$ (in our case the doubling cavity resonance). For every frequency component ω_n from the probe spectrum the complex transmission is given by $T(\omega_n) = e^{-\alpha_n/2 - i\beta_n}$. Here α_n denotes the absorption coefficient and the β_n is responsible for the phase change at ω_n by the absorbing medium. In the case of a cavity it describes the phase shift acquired during subsequent round-trips through the cavity. The transmitted field can be expressed as

$$E_T(t) = E_0 e^{i\omega t} \sum_{n=-\infty}^{\infty} T(\omega_n) J_n(M) e^{in\Omega t}. \tag{1.4}$$

Restricting to conditions in the doubling cavity yields $M \ll 1$ and $\Omega \gg \Gamma$. In this case terms with $J_n(M)$ for $n > 1$ can safely be neglected and $J_n(M) \approx M^n/(2^n n!)$. Additionally, from properties of the Bessel function $J_{-1}(M) = -J_1(M)$. It is furthermore assumed that absorption and dispersion differ only slightly for the n and $n+1$ probe wave frequency components, while the overall absorption and dispersion is weak. Finally, the frequency component Ω is selected from the transmitted signal $|E_T(t)|^2$ with a lock-in amplifier tuned at Ω. This yields

$$I_T^\Omega(t) = |E_T^\Omega(t)|^2 = E_0^2 e^{-\alpha_0}[1 \quad + \quad M/2(\alpha_{-1} - \alpha_1)\cos(\Omega t)$$
$$+ \quad M(\beta_{-1} - 2\beta_0 + \beta_1)\sin(\Omega t)]. \qquad (1.5)$$

The term with $\cos(\Omega t)$ represents the absorption profile. The signal, phase shifted by $\pi/2$ from the absorption (the $\sin(\Omega t)$ component), represents a superposition of the dispersion signals of the carrier and the two sidebands. The dispersion sidebands have opposite phase (slope) from the carrier. It allows for an easy stabilization on the carrier dispersion signal, which is important for the stabilization purposes.

The absorption near resonance is given by [19]

$$\alpha(\nu) = A\frac{(\Delta\nu/2)^2}{(\nu - \nu_0)^2 + (\Delta\nu/2)^2}, \qquad (1.6)$$

and the dispersion by

$$\beta(\nu) = \frac{2(\nu - \nu_0)}{\Delta\nu} \times \alpha(\nu). \qquad (1.7)$$

Here $\omega = 2\pi\nu$, ν_0 is the resonance frequency, $\Gamma = 2\pi\Delta\nu$ and A represents the amplitude of a Lorentz absorption function. The reflected intensity by the doubling cavity from M1 $I_R(t) = 1 - I_T(t)$ and hence the in-phase ($\cos(\Omega t)$) component of $I_R(t)$ is given by

$$I_R^\Omega(t, \cos(\Omega t)) = \frac{A_{eff}}{2}e^{-\alpha_0}\left[\frac{(\Delta\nu/2)^2}{(\nu - \Omega/2\pi - \nu_0)^2 + (\Delta\nu/2)^2}\right.$$
$$\left. -\frac{(\Delta\nu/2)^2}{(\nu + \Omega/2\pi - \nu_0)^2 + (\Delta\nu/2)^2}\right], \qquad (1.8)$$

with an effective amplitude A_{eff}. Similarly, the quadrature ($\sin(\Omega t)$) part of the reflected intensity equals

$$I_R^\Omega(t, \sin(\Omega t)) \quad = \quad \frac{2A_{eff}}{\Delta\nu}e^{-\alpha_0}\left[\frac{(\nu - \Omega/2\pi - \nu_0)}{(\nu - \Omega/2\pi - \nu_0)^2 + (\Delta\nu/2)^2}\right.$$
$$+ \quad \left.\frac{(\nu + \Omega/2\pi - \nu_0)}{(\nu + \Omega/2\pi - \nu_0)^2 + (\Delta\nu/2)^2} - 2\frac{(\nu - \nu_0)}{(\nu - \nu_0)^2 + (\Delta\nu/2)^2}\right]. (1.9)$$
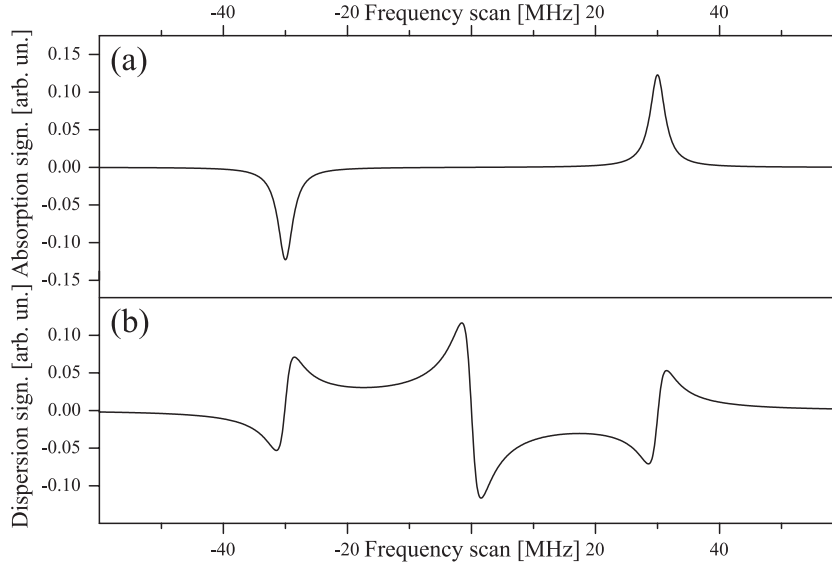
Figure 1.5: Calculated FM signals corresponding to (a) absorption part and (b) dispersion part of the signal from the lock-in amplifier. The simulation parameters were following $\Delta\nu = 2.9$ MHz, $\Omega/2\pi = 30$ MHz, $A_{eff} = 0.123$ arb.un. (arbitrary units). The frequency scale is relative to ν_0.

Fig. 1.5 visualizes Eq. 1.8 and Eq. 1.9 for realistic experimental conditions $\Delta\nu = 2.9$ MHz and $\Omega/2\pi = 30$ MHz relative to ν_0. It should be noted that this simple model reproduces very well the experimental curves observed from the doubling cavity, as discussed in the following section.

A more thorough and elaborate treatment of the FM and wavelength modulation spectroscopy one can find in [23, 24, 26–29].

Stabilization

The phase of the green fundamental beam is modulated by applying a sine voltage with $\Omega/2\pi = 30$ MHz over an elevated background voltage to an electro-optic modulator (Fig. 1.4). The electro-optic modulator (EOM) consists of a KDP crystal (KH_2PO_4 – potassium di-hydrogen phosphate) in transverse configuration. To shield the modulating 30 MHz signal, the crystal is housed in a thick iron box coated with gold. The in- and output holes in the box are sealed by a brewster cut windows. This is necessary, because the KDP crystal is strongly hygroscopic.

After passing the EOM the fundamental laser beam with two sidebands is coupled
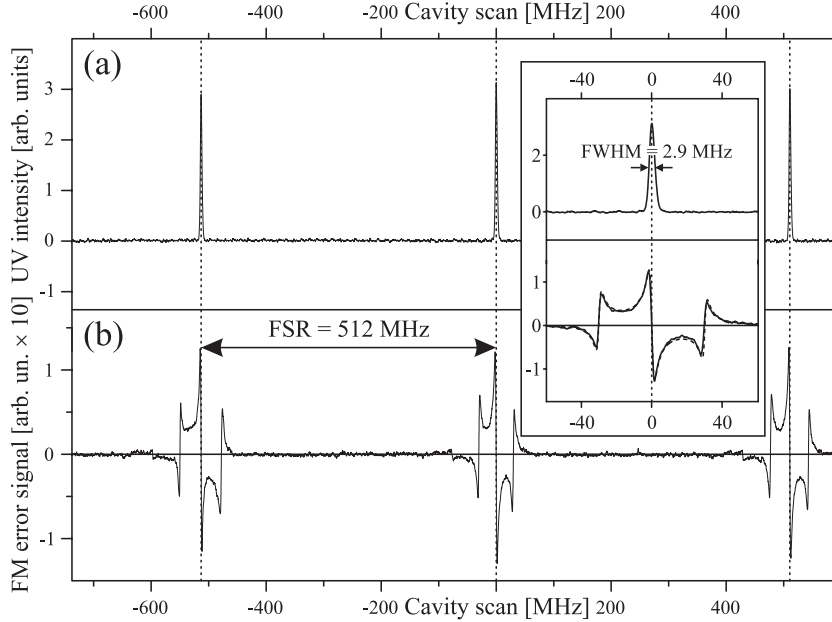
Figure 1.6: Doubling cavity signals obtained with cavity scan. (a) UV intensity peaks at each cavity resonance. (b) Heterodyne beat (dispersion) signals of FM spectroscopy measured on the green beam reflected from the cavity input coupler. Free spectral range (FSR) of the doubling cavity is also shown. The inset depicts a zoom in to the vicinity of one of the UV resonance peaks with the depicted linewidth of FWHM = 2.9 MHz. In the lower part of the inset the experimental FM dispersion signal (solid line) is compared with a simulated one (dashed line). The frequency scale is relative to one of the cavity resonances.

into the doubling cavity. Part of this beam passes M1 and circulates in the cavity, where in every subsequent round trip it slightly leaks out of the cavity via M1 and recombines with the initially reflected beam. The total reflected beam is attenuated by a neutral density filter NDF with T = 1% and detected with a photodiode (Det). The signal from Det is fed to a lock-in amplifier built in the stabilization electronics. Both the in-phase and quadrature signals can be monitored on an oscilloscope.

A typical heterodyne beat signal obtained from the fundamental beam reflected by M1 is shown in Fig. 1.6 and compared with a simulated dispersion signal from Eq. 1.9. The experimental signal was obtained by scanning the cavity with the piezo-mounted M2 mirror over ~ 2.5 times the cavity free spectral range (FSR). Fig. 1.6 clearly shows three cavity resonances in the generated UV signal and the dispersed
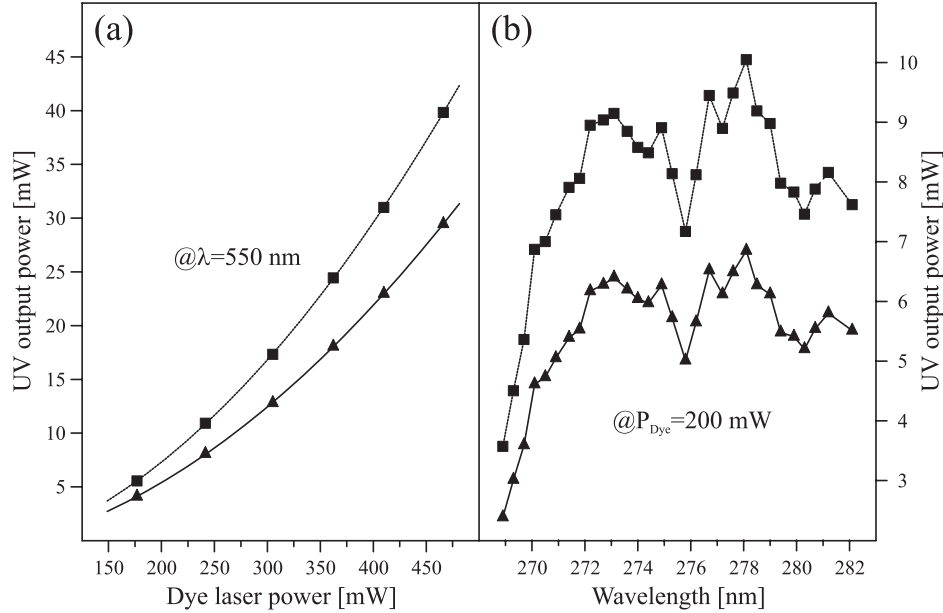
Figure 1.7: UV output power *versus* (a) ring dye laser power at a fixed wavelength $\lambda = 550$ nm and (b) different wavelengths at the fixed dye laser power $P_{\mathrm{dye}} = 200$ mW. The black squares on the dotted line represent the total UV power, generated in the BBO crystal, while the triangles on the solid line correspond to the UV power coupled out of the doubling cavity.

reflection signal. It should be noted that such 'clean' signals are only obtained in a well aligned cavity running single TEM_{00} mode. Otherwise many resonances can be present, corresponding to higher TEM modes.

If the cavity is aligned such that the TEM_{00} mode is dominant, the length of the cavity can be manually locked to the dispersion signal. The locking point is the intersection of the steep slope with zero. If locked, the electronics compensates for deviation of the cavity length by applying the appropriate voltage to the piezo M2 mirror. The mechanism, which automatically finds the lock point is described in the Section "The UV frequency scans".

Cavity performance

The dependency of the generated UV power on the fundamental power at $\lambda = 550$ nm is shown in Fig. 1.7(a). The 'total' UV power denotes the sum of the main UV beam (measured behind the output coupler M4), two UV reflections from the BBO crystal

faces, which constitute $\sim 10\%$ of the main UV beam and the UV losses caused by the M4 transmission of $\sim 90\%$. From theory the dependency of the total UV power P_{UV}^{tot} *versus* fundamental power P_{dye} should be quadratic, however our curve can be fitted with the following equation: $P_{UV}^{tot} = 1.42 \times 10^{-4} P_{dye}^2 + 2.3 \times 10^{-2} P_{dye} - 1.4$. As discussed by E. Jurdik [21, 22], the linear term originates from the fact that the cavity is not an empty resonator. Its enhancement factor depends on the losses, which increase with increasing SHG conversion efficiency $\eta = P_{UV}^{tot}/P_{dye}$ and η also increases with P_{dye}. The result is that although with increasing fundamental power η increases, at the same time the enhancement factor in the cavity decreases and a linear term arises in $P_{UV}^{tot} = f(P_{dye})$.

As can be seen from Fig. 1.7(a) the maximum obtained UV power at $\lambda = 275$ nm was $P_{UV} = 32$ mW ($P_{UV}^{tot} = 40$ mW), which implies a conversion efficiency of $\eta = 8.6\%$. A much higher conversion efficiency of 53% was reported for this cavity design pumped with 1 W of a narrow-band (FWHM ~ 660 kHz) Ti:Sapphire laser at $\lambda \sim 850$ nm with LBO (LiB_3O_5 – lithium tri-borate) as doubling crystal [22]. The difference can be attributed mainly to the lower conversion efficiency of the BBO crystal, different fundamental powers and to the much broader linewidth (FWHM $\leqslant 4.1$ MHz) of our ring dye laser.

Fig. 1.7(b) shows the wavelength dependence of the generated UV power at fixed fundamental power $P_{dye} = 200$ mW. The data was acquired by mode-hoping the thin etalon of the ring dye laser in steps of ~ 0.9 nm and subsequent complete realignment of the doubling cavity with the crystal. At $\lambda < 270$ nm we observe a steep cut-off. This is caused by the increasing transmission of the HR coatings of the cavity mirrors at $\lambda < 540$ nm. Otherwise the dependency is quite flat, which indicates that similar conversion efficiencies should be possible over the whole range of the cavity mirrors ($\lambda \sim 270 - 295$ nm). In Fig. 1.7 (b) only part of this wavelength region is shown. This is because we ran out of the phase-matching angular adjustment of the used crystal, the next region needs a crystal with another cut.

The UV beam is astigmatic due to a walk-off between the fundamental and the generated UV beams in the critically phase-matched crystal. This is not a serious problem for our spectroscopic applications and can be compensated for if necessary.

The UV frequency scans

It is essential for our spectroscopic applications to be able to scan the UV frequency over relatively large frequency intervals. The ring dye laser can be scanned 30 GHz, which results in 60 GHz in the UV. In order to scan the UV, the length of the doubling cavity has to be varied during the laser scan. The M2 mirror is mounted on PZT, which allows for a maximum travel of 9.1 μm. Since $\delta L = -\lambda \delta \nu / \text{FSR}$, the maximum scan is limited to $\delta \nu = 8.5$ GHz at $\lambda = 550$ nm ($\delta \nu = 17$ GHz in the UV). Larger scans can be made by tuning the cavity with a pair of Brewster plates, placed in the
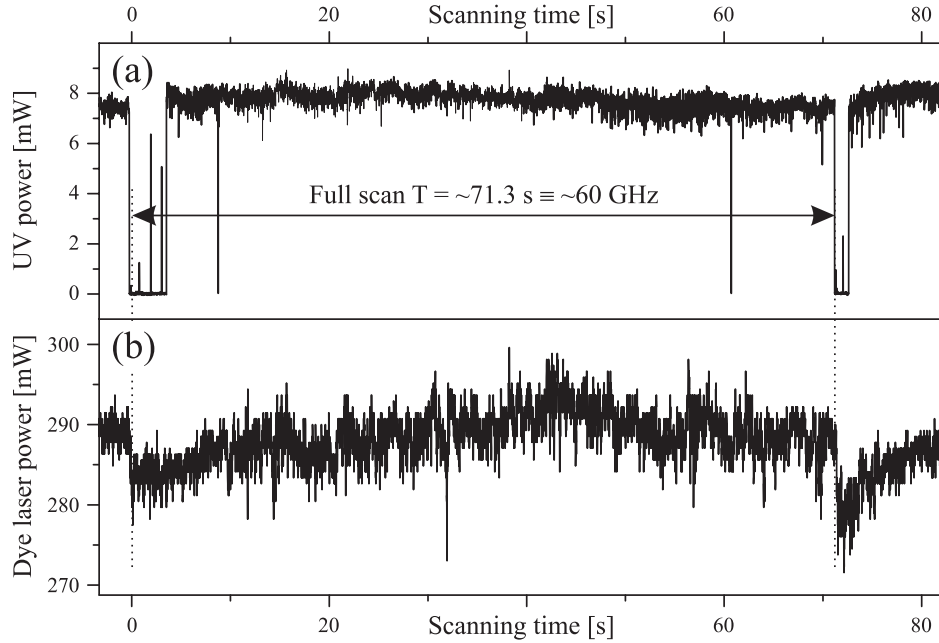
Figure 1.8: (a) 60 GHz UV frequency scan with (b) corresponding 30 GHz ring dye laser frequency scan. The scan speed is 8.4 MHz/point in the UV, where one point corresponds to 10 ms.

cavity. However, this introduces extra intra cavity elements with possible additional losses.

A different approach was therefore implemented. If the frequency of the fundamental beam is scanned in frequency, the cavity M2-PZT mirror follows the frequency change through the stabilization loop. If the PZT reaches the end of its range, the stabilization electronics unlocks the cavity and sets the PZT voltage close to the opposite end of the displacement. The electronics then relocks the cavity. This procedure is relatively fast ($t \lesssim 1$ ms) and we call it autolocking.

The autolock has another important feature. In case of an instability, which unlocks the cavity, the autolock is capable to relock it. The reflected intensity from the cavity input coupler is used to monitor the lock/unlock status of the cavity. If this intensity is above a certain preset value (or equals zero), the cavity is unlocked and actively relocks. To prevent fictitious autolock actions a waiting time of 10 ms is built in (a changeable value). If after 10 ms the unlock detection is still present the autolock is executed. If it fails, the stabilization loop is opened and an error is
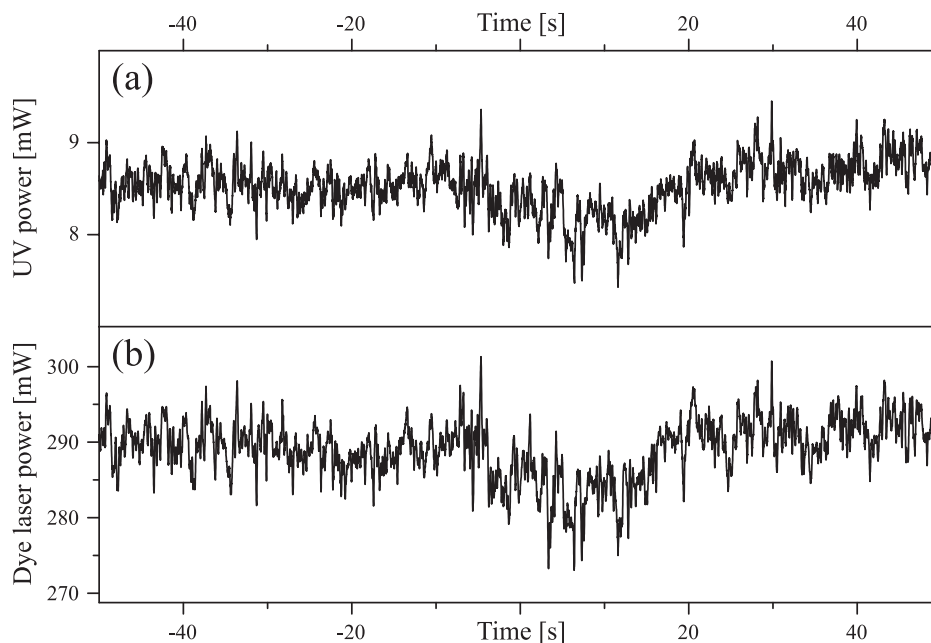
Figure 1.9: (a) UV power as a function of time with (b) the corresponding ring dye laser power at the fixed wavelength $\lambda = 550$ nm. The time resolution is 0.1 s.

displayed.

Let us now compare these timings with those required in an experiment, where a 60 GHz UV scan was typically taken in 15 min. To obtain a spectrum with a good resolution a minimum of about 10 points/spectral linewidth are needed. The apparatus linewidth (FWHM) is 15 MHz and the Lorentz linewidths of the molecules that can be investigated are larger than 10 MHz. The acquisition rate in the LIF high resolution experiments should therefore be 27 points/s, so one point corresponding to 38 ms. Clearly this can be handled by the stabilization electronics without loosing any data points. A reasonable maximum acquisition rate would be 200 points/s (5 ms/point), where the 'waiting' time is shortened to 5 ms. This corresponds to the full 60 GHz UV scan taken in 2 min.

A fast 60 GHz scan around $\lambda = 275$ nm with a rate of 200 points/s and waiting time of 10 ms is shown in Fig. 1.8. The fundamental power is also displayed. Fig. 1.8 shows that with such high acquisition rate a few points are lost during a scan (in this case two).

The UV frequency and power stability

The linewidth of the UV generated in the doubling cavity is estimated to 2.9 MHz (FWHM) from a Lorentz fit to the UV peaks from Fig. 1.6(a). This is similar to the UV linewidth obtained from the intra-cavity doubling of the same ring dye laser.

   The stability of the UV power during a frequency scan can be derived from Fig. 1.8. The relative UV power stability over a full 60 GHz scan equals 5.0% (RMS/Average × 100%). The corresponding dye laser power stability is 1.0%. The power stability at a fixed wavelength (275 nm) as a function of time is presented in Fig. 1.9. In that figure one data point was acquired in 0.1 s. The relative stability of the UV power and dye laser power were 3.1% and 1.3%, respectively.

1.3   Automated assignment of spectra – genetic algorithms

1.3.1   The genetic algorithms

Most of the spectra discussed in this thesis were analyzed using automatic assignments with genetic algorithms (GA). A detailed description of the GA can be found in [30, 31]. The genetic algorithm is a global optimizer, which utilizes concepts copied from natural reproduction and selection processes. For a detailed description of the GA the reader is referred to the original literature [32–34]. The full GA evaluation contains the following steps, also presented schematically in Fig. 1.10:

- Initialization. In this step the initial values for all parameters (genes) are set to random values between lower and upper limits imposed by the user. No prior knowledge of the parameters is necessary. A vector of all genes, describing completely the analyzed spectrum in called a chromosome. A total number of 300 - 500 chromosomes is randomly generated and forms a population.

- Evaluation. The solutions (chromosomes) are evaluated by a fitness function F_i, which is a measure for the quality of the individual solution. The fitness function which is used here, is described in the following section. Only a certain part of the best chromosomes is taken to the next step.

- Reproduction. Pairs of chromosomes are combined via a crossover process. This might be a one-point, two-point or uniform crossover. This process basically explores the error landscape.

- Mutation. The value of a small number of genes is changed randomly. Mutation mainly reduces the chance of a fit to get stuck in a local minimum. The best solutions within a generation are excluded from mutation to prevent them from being lost (so-called elitism).
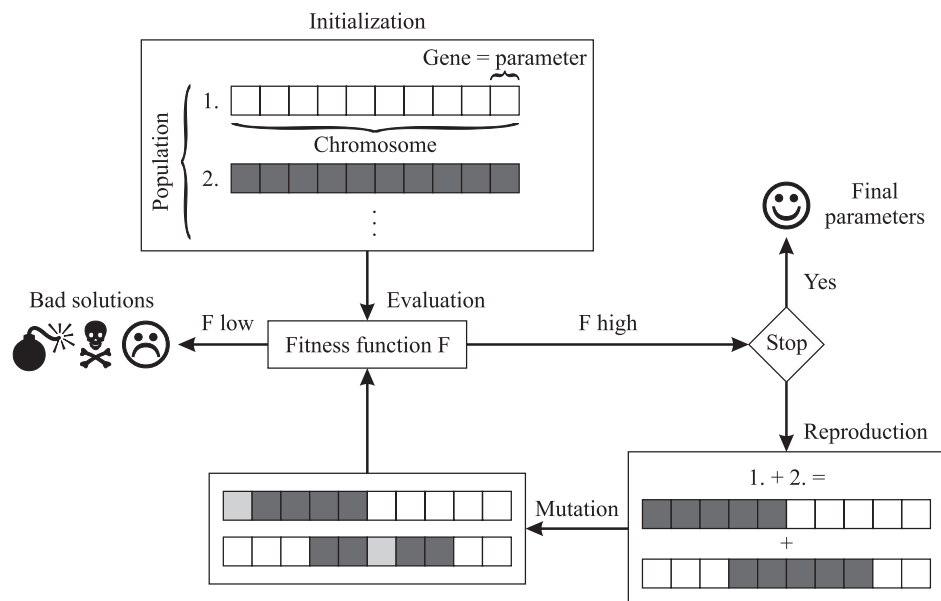
Figure 1.10: Schematics of the GA optimization process.

- Stop. One optimization cycle, including evaluation of the fitness of all chromosomes is called a generation. The whole process repeats until the preset number of generations is reached. In the case of our high resolution spectra the fit requires mostly $300 - 500$ generations to converge.

The performance of the GA depends on the internal parameters like mutation rate, elitism, crossover probability and the population size. These should be optimized for a given problem. Fortunately, this meta-optimization results in similar parameters for a family of similar problems, like fitting high resolution spectra to different rotational Hamiltonians. For this case the meta-optimization for some of the parameters is described in [31].

1.3.2   The Fitness Function

The fitness function is very critical for the GA to be successful. A more elaborate discussion on the choice of this function can be found elsewhere [30, 31]. The function used here is defined by Hageman *et al.* [30] and can in the mathematical shorthand

form be expressed as [31]

$$F_{fg} = \frac{(\boldsymbol{f}, \boldsymbol{g})}{\|\boldsymbol{f}\| \, \|\boldsymbol{g}\|}, \tag{1.10}$$

where $\boldsymbol{f} = [f_i]$ and $\boldsymbol{g} = [g_j]$ for $i, j = 1, \ldots, N$, represent the experimental and calculated spectra, respectively, with N number of points. The inner product $(\boldsymbol{f}, \boldsymbol{g})$ is defined with the metric $\boldsymbol{W}$

$$(\boldsymbol{f}, \boldsymbol{g}) = \boldsymbol{f}^T \boldsymbol{W} \boldsymbol{g} \tag{1.11}$$

and the norm of $\boldsymbol{f}$ defined as $\|\boldsymbol{f}\| = \sqrt{(\boldsymbol{f}, \boldsymbol{f})}$ (a similar definition holds for $\boldsymbol{g}$). $\boldsymbol{W}$ has the matrix elements $W_{ij} = w(|j - i|) = w(r)$. For $w(r)$ we used a triangle function [30] with a user controlled width of the base Δw

$$w(r) = \begin{cases} 1 - |r| / \left(\tfrac{1}{2}\Delta w\right) & \text{for } |r| \leqslant \tfrac{1}{2}\Delta w \\ 0 & \text{otherwise.} \end{cases} \tag{1.12}$$

In order for F_{fg} to serve as a good fitness function for the quality of the fit, it should have the property that it reaches its maximum value if and only if $\boldsymbol{f}$ and $\boldsymbol{g}$ are identical (apart from a normalization). This condition is fulfilled provided the matrix $\boldsymbol{W}$ is positive definite. The proof that this holds for w defined in Eq. (4.14) can be found in Appendix A of Ref. [31].

The broadening of the spectra, introduced by the weight function $w(r)$ critically determines the ability and speed of the GA to converge to the global minimum. Let's take a simple analogy of finding the deepest valley in a very ruffled blanket. It is a difficult and slow process, because there are so many valleys and some of them far away form each other. Furthermore, once one gets trapped in one of the valleys, one is unable to see the others, which might be deeper. Now, if we pull the blanket (not too hard), we shallow the whole error landscape and effectively allow ourselves to quickly find the leftover minima and choose the deepest one. So, the weight function smoothes out the error landscape (stretches the blanket) allowing GA to quickly and reliably find a global minimum.

In the first GA calculation generally large limits are given to the starting parameters, which imply a large error landscape with possible many local minima. To account for that the $w(r)$ should be chosen relatively wide. We typically used $\Delta w \sim 15$ times the linewidth of an individual rovibronic line from the fitted spectrum (Δ_{LW}). The resulting first set of the molecular parameters (if reasonable, which is tested *by eye*) still has to be refined with the GA, now with smaller limits for parameters and correspondingly narrower weight function. The final fit is made with $w(r) = 0$ and a lineshape function represented by a Voigt profile.

A lineshape fit if needed is always made at the end, if all other parameters are known. Since the GA performs a lineshape fit of the complete spectrum, much better information on the linewidth is obtained than from a lineshape fit to a few individual

lines. To improve the intensity fit we utilize in all our fits the two temperature model [7].

Automatic assignments using GA can be performed for a variety of spectra arising from different model Hamiltonians, from (overlapping) multiple spectra obtained from different molecules and/or isotopomers. The Hamiltoinians that are supported in the current version range from a symmetric top, a simple asymmetric rotor, spectra from molecules with internal rotation from a CH_3 group (threefold or sixfold barrier case) as well as the two-fold barrier case. The Hamiltonian for the 3-fold two rotor case is also supported but limited to the special case of two identical rotors, symmetric to the a-axis, with their torsional axes in the ab-plane. All kind of combinations, even of different types of spectra, can be made. The various individual cases are used in the following chapters of this thesis.

References

[1] D. Pratt. High resolution spectroscopy in the gas phase: Even large molecules have well-defined shapes. *Annu. Rev. Phys. Chem.*, 49:481–530, 1998.

[2] E.W. Gordy and R. L. Cook. *Microwave Molecular Spectra*. John Wiley & Sons, New York, 3rd edition, 1984.

[3] W. Demtröder. *Laser Spectroscopy*. Springer-Verlag, Berlin, 1981.

[4] R. Helm, H. P. Vogel, and H. Neusser. Highly resolved UV spectroscopy: structure of S_1 benzonitrile and benzonitrile-argon by correlation automated rotational fitting. *Chem. Phys. Lett.*, 270:285–292, 1997.

[5] Ch. A. Haynam, D. V. Brumbaugh, and D. H. Levy. The spectroscopy, photophysics, and photochemistry of the dimer of dimethyl tetrazine. *J. Chem. Phys.*, 81:2282–2294, 1984.

[6] L. A. Philips and D. H. Levy. The rotationally resolved electronic spectrum of indole in the gas phase. *J. Chem. Phys.*, 85:1327–1332, 1986.

[7] Y. R. Wu and D. H. Levy. Determination of the geometry of deuterated tryptamine by rotationally resolved electronic spectroscopy. *J. Chem. Phys.*, 91:5278–5284, 1989.

[8] W. A. Majewski and W. L. Meerts. Near-UV spectra with fully resolved rotational structure of naphthalene and perdeuterated naphthalene. *J. Mol. Spectr.*, 104:271–281, 1984.

[9] W. A. Majewski. A tunable, single frequency UV source for high resolution spectroscopy in the 293–330 nm range. *Opt. Comm.*, 45:201–206, 1983.

[10] P. Uijt de Haag. *Energy Redistribution in Photoexcited Molecules.* PhD thesis, Katholieke Universiteit Nijmegen, 1990.

[11] G. Berden. *High Resolution UV Spectroscopy of Aromatic Molecules.* PhD thesis, Katholieke Universiteit Nijmegen, 1995.

[12] K. Remmers. *Small Aromatic Molecules Studied by Spectroscopy.* PhD thesis, Katholieke Universiteit Nijmegen, 2000.

[13] Y.R. Shen. *The Principles of Nonlinear Optics.* John Wiley & Sons, New York, 1984.

[14] R.W. Boyd. *Nonlinear Optics.* Academic Press, San Diego, CA, 1992.

[15] D.L. Mills. *Nonlinear Optics: Basic Concepts.* Springer-Verlag, Heidelberg, 1991.

[16] P.N. Butcher and D. Cotter. *The Elements of Nonlinear Optics.* Cambridge University Press, Cambridge, 1990.

[17] A. Yariv. *Quantum Electronics.* John Wiley & Sons, New York, 1989.

[18] A. Yariv and P. Yeh. *Optical Waves in Crystals.* John Wiley & Sons, New York, 1984.

[19] B.E.A. Saleh and M.C. Teich. *Fundamentals of Photonics.* John Wiley & Sons, New York, 1991.

[20] Ch. Davis. *Lasers and Electro-Optics.* Cambridge University Press, Cambridge, 1996.

[21] E. Jurdik. *Laser manipulation of atoms and nanofabrication.* PhD thesis, Katholieke Universiteit Nijmegen, 2001.

[22] E. Jurdik, J. Hohlfeld, A.F. van Etteger, A.J. Toonen, W.L. Meerts, H. van Kempen, and Th. Rasing. Performance optimization of an external enhancement resonator for optical second-harmonic generation. *J. Opt. Soc. Am. B*, 19:1660, 2002.

[23] R.V. Pound. Electronic stabilization of microwave ocillators. *Rev. Sci. Instrum.*, 17:490–505, 1946.

[24] R.W.P. Drewer and J.L. Hall and F.V. Kowalski and J. Hough and G.M. Ford and A.J. Munley and H. Ward. Laser phase and frequency stabilization using an optical resonator. *Appl. Phys. B*, 31:97–105, 1983.

[25] T.W. Hänsch and B. Couillaud. Laser frequency stabilization by polarization spectroscopy of a reflecting reference cavity. *Opt. Commun.*, 35:441–444, 1980.

[26] G.C. Bjorklund. Frequency-modulation spectroscopy: a new method for measuring weak absorptions and dispersions. *Opt. Lett.*, 5:15–17, 1981.

[27] J.L. Hall, L. Hollberg, T. Baer, and H.G. Robinson. Optical heterodyne saturation spectroscopy. *Appl. Phys. Lett.*, 39:680–682, 1981.

[28] J.M. Supplee, E.A. Whittaker, and W. Lenth. Theoretical description of frequency modulation and wavelength modulation spectroscopy. *Appl. Opt.*, 33:6294–6302, 1994.

[29] R. Arndt. Analytical line shapes for lorentzian signals broadened by modulation. *J. Appl. Phys.*, 36:2522–2524, 1965.

[30] J. A. Hageman, R. Wehrens, R. de Gelder, W. Leo Meerts, and L. M. C. Buydens. Direct determination of molecular constants from rovibronic spectra with genetic algorithms. *J. Chem. Phys.*, 113:7955–7962, 2000.

[31] W. Leo Meerts, M. Schmitt, and G. Groenenboom. New applications of the genetic algorithm for the interpretation of high resolution spectra. *Can. J. Chem.*, 82:804–819, 2004.

[32] J. H. Holland. *Adaption in Natural and Artificial Systems*. MI: The University of Michigan Press, Ann-Arbor, 1975.

[33] D. E. Goldberg. *Genetic Algorithms in search, optimisation and machine learning*. Addison-Wesley, Reading Massachusetts, 1989.

[34] I. Rechenberg. *Evolutionsstrategie - Optimierung technischer Systeme nach Prinzipien der biologischen Evolution*. Frommann-Holzboog, Stuttgart, 1973.

TWO

Structure of tetracene-argon and tetracene-krypton complexes from high resolution laser experiments at 450 nm [1]

Abstract

The partly rotationally resolved spectra of tetracene-Ar and tetracene-Kr are revisited. In a previous study it was not possible to assign experimental spectra. The spectra were obtained from high resolution laser experiments around 450 nm. With state of the art fast computers and recently developed software and algorithms we succeed in explaining the observed spectra. Rotational constants of the complexes are obtained from which the structures of the clusters are deduced. It is found that the noble gas is located above the middle of one of the central benzene rings of the tetracene molecule with distances to the plane of 3.42 and 3.65 Å for Ar and Kr, respectively.

2.1   Introduction

In the study of a van der Waals cluster, its structure is perhaps the most important property and is essential for understanding the reactivity and dynamics within the complex. A great database of structures for all kinds of weakly bound complexes in both ground and excited states was derived by high resolution studies over last 20 years. We will focus here on the clusters of aromatic molecules with argon (Ar) and krypton (Kr) atoms.

---

[1] I. Szydłowska, G. Myszkiewicz and W. L. Meerts, *Chemical Physics* **283** (2002) p. 371-377.

The $S_1 \leftarrow S_0$ transition in the tetracene-Ar_n ($n = 1 - 26$) and tetracene-Kr_n ($n = 1 - 14$) complexes were investigated under vibrational resolution by Ben-Horin *et al.* [1]. The same transition in tetracene-Ar_n ($n = 1 - 5$) complex was also studied under low resolution by Hartmann *et al.* [2] in He droplets. However, because these studies were performed at vibrational resolution, the structures of the tetracene-Ar, Kr complexes could not be deduced. More work has been carried out on the complexes of benzene with noble gas atoms [3]. High resolution spectra are available and structures of the complexes with noble gases from He to Xe are known [4, 5].

The tetracene molecule consists of four fused benzene rings in a row. The molecule is planar and belongs to D_{2h} point group. The ground and first singly excited electronic states are characterized by A_g and B_{2u} symmetries, respectively.[1] The $S_1 \leftarrow S_0$ transition in the bare tetracene molecule was investigated under vibrational resolution in a seeded molecular beam with a pulsed laser [6–8] and more recently in He droplets [2]. Amirav *et al.* [6] assigned several vibrational states of this transition. Their conclusion was that the S_1 state in tetracene consists of three different vibrational regions: the sparse level structure for $E_v = 0 - 1000$ cm^{-1}, intermediate region of increasing Fermi resonances resulting in quasicontinuum above $E_v \geqslant 1800$ cm^{-1}.

Three vibrational states from the lowest energy regime were studied under rotational resolution by van Herpen *et al.* [9]. Two of them belong to a_g-type totally symmetric vibrational mode (0-0 and 311 cm^{-1}). They are both active in the $S_1(^1B_{2u}) \leftarrow S_0(^1A_g)$ symmetry allowed electronic spectrum and were identified under rotational resolution as b-type transitions. The third one, the nontotally symmetric b_g-type mode (471 cm^{-1}) was also observed, because it gains intensity from a coupling with the higher in energy ^1B_u electronic state. The corresponding transition showed up as a-type band under rotational resolution. Van Herpen *et al.* [9] were able to fully assign the rotational transitions in these bands and determined the rotational constants A, B and C in the ground and S_1 states.

In supersonic molecular beams the molecules are cooled rotationally to temperatures of $2 - 4$ K. This leads to a considerable reduction in the amount of transitions in the spectrum and its simplification. However, in spite of the use of supersonic beams, van Herpen *et al.* [9] were not able to assign the spectra of tetracene-Ar and tetracene-Kr complexes. Their analysis was hampered by the congestion and lack of fast computers with appropriate software. The complexity of the spectra is due to very small rotational constants of these heavy clusters. This causes both strong overlap as well as coincidental accumulation of transitions. In this paper we present a successful assignment of tetracene-Ar and tetracene-Kr complexes. The success of the present work comes from the fact that in the past years the power of computers has strongly increased while new software and algorithms have been developed.

---

[1] The axis system is chosen as $\{x, y, z\} = \{c, b, a\}$. The origin of the (x, y, z) coordinate system is in the center of mass of the tetracene, the y and z axis are in the tetracene plane with the z axis along the center of the four rings. The x axis is perpendicular to the tetracene plane.

Several attempts were recently undertaken to automate the interpretation of rotational spectra. The group of Neusser *et al.* [10] developed the so-called correlation automated rotational fitting algorithm. The program directly fits experimental data without any preceding assignment of lines. This method still requires accurate initial estimates of the rotational constants obtained from other experiments and has a limited applicability. Another, more general approach using the genetic algorithm (GA) was presented by Hageman *et al.* [11]. The idea of this approach is taken from the theory of evolution used in GA as a global optimization procedure. The procedure by itself needs only rough estimates of the molecular parameters at the start and therefore does not require accurate knowledge of these parameters. It even tends to work better if larger search regions are used.

The recently developed program by Plusquallic *et al.* JB95 [12] provides the user with an on-screen graphical display of the calculated and experimental spectra, with options to easily and very fast search the parameter space while observing the effect on the simulated spectrum instantly. The details of the program will be discussed below. With this program we succeeded in the assignment of the tetracene-Ar and tetracene-Kr spectra.

In this paper we report the rotational parameters and the deduced structures for the tetracene-Ar and tetracene-Kr complexes. The obtained structural parameters compare very well with that of benzene-Ar and benzene-Kr complexes.

2.2   Experiment

A molecular beam combined with a high resolution laser source was used to measure rotationally resolved spectra of tetracene-X (X = Ar, Kr) van der Waals complexes [9]. The experimental setup was described previously [13, 14] hence only the main features will be summarized here. A sample of tetracene was heated to approximately 210 °C in a quartz source. The vapour was mixed with a carrier gas (Ar or Kr) and expanded through a 100 μm nozzle into a vacuum chamber. The Doppler linewidth was reduced to about 15 MHz by doubly skimming the molecular beam. The interaction zone with the laser beam was 30 cm from the orifice. The undispersed laser-induced fluorescence was collected and imaged onto the photocathode of a photomultiplier.

Laser radiation around 450 nm with $\sim$ 3 MHz bandwidth was generated by a single frequency cw dye laser system operating on stilbene 3. For relative frequency marking a sealed-off, temperature stabilized Fabry-Perot interferometer with a 150 MHz free spectral range was utilized. Absolute frequency measurements were performed with a home-built wavelength meter [13] based on a Michelson interferometer, which compares the dye laser wavelength with the accurately known wavelength of a reference HeNe laser. The spectrometer was interfaced with a computer, where all the data were stored and analyzed.

2.3 Analysis of the spectra

2.3.1 Computational approach

The $S_1 \leftarrow S_0$ transition in tetracene-Ar and tetracene-Kr was observed by van Herpen *et al.* but they were not able to perform a detailed analysis and assignment. This was due to a strong overlap of the rotational transitions and to a relatively low computer power at that time. It turned out that with current state-of-the-art fast computers, newly developed software and algorithms we were able to successfully reinvestigate spectra of the tetracene-Ar and tetracene-Kr complexes.

The utilized methods are based on the following principles. Rather than fitting individual transitions, which are almost not present in the spectra of the complexes of tetracene, a global overall fit of the shape of the spectra is performed. Two fitting schemes have been applied: (a) a fully computer controlled technique using the GA and (b) a man controlled method by visual inspection of the spectra using the JB95 program [12].

GA's are a group of programs for solving global minimization problems based on the theory of evolution. It has been shown [11] that this technique was very successful in routine-like analysis of (partly) resolved rotational transitions. For more information about GA itself we refer to Ref. [15] and [16].

The JB95 program is a very powerful tool in analysis of the rotationally resolved spectra. The program visually displays the observed and predicted spectra on the screen. It has basically two options. The standard option is a step by step assignment of the individual rotational transitions with their full quantum numbers and a subsequent fit of the molecular parameters. The screen output can be used to judge the result and to make more assignments. In the second option again the observed and calculated spectra are shown on the screen for some starting values of the parameters. In addition each parameter can be changed directly by mouse control track bars that provide a smooth variation of the molecular constants while displaying the effect immediately on the screen. Effectively, hundreds of calculations can be made this way and the effect can be judged immediately. Although the problem is still multidimensional, it turned out that the effects of different parameters on the shape of the spectra can be judged instantly. Finally, the program uses a user-friendly windows environment.

All the rotational spectra were predicted using the asymmetric rotor Hamiltonian with the two temperature model [17].

2.3.2 Tetracene-Ar complex

The initial ground state rotational constants of tetracene-Ar complex were estimated using the information from the fully analyzed tetracene parent molecule, combined with an estimate of the position of the Ar atom, based on a simple theoretical

model [9, 18]. The model used a Lennard-Jones 6-12 potential with pairwise interactions between the Ar atom and the atoms in the tetracene molecule. Not unexpectedly, a favorable position of Ar was found above the center of one of the inner rings in tetracene with a distance from the tetracene molecular plane of 3.43 Å. The type of the transition was fixed to the b-type, based on the symmetry arguments and on the assumption that the transition dipole moment was that of the tetracene chromophore.

At first GA were employed. Because of a lack of any information about the excited state rotational constants large regions were assumed for the search. Although the GA program did not give satisfactory results, it allowed for narrowing down the uncertainties in the excited state rotational constants. In the next step the JB95 program was successfully used to determine the final parameters for the tetracene-Ar complex. The best overall fit of the spectrum is compared with the experimental one in Fig. 2.1. The quality of the predicted spectrum is surprisingly good taking into account the extreme complexity of the underlying transition. All major branches are reproduced and especially the changes in the *distances* between the branch-heads are well reproduced.

The best rotational parameters for 0-0 rovibronic band of the tetracene-Ar complex are presented in Table 2.1. The uncertainties in the rotational constants are estimated to be 1 MHz, while the changes upon electronic excitation ($\Delta A_g = A'_g - A''_g$) are accurate to 0.1 MHz. These estimates are based on visual changes in the spectral shapes under the change of rotational parameters. The 311 cm^{-1} rovibrational band can be described with the parameters identical within the experimental accuracy. Unfortunately, we were not able to analyze the third 471 cm^{-1} transition, because the experimental data were not available any more.

As shown by Meerts *et al.* [19] the position of the Ar in the complex can be determined from only the moments of inertia[2] of the bare molecule and those of the corresponding complex. This allows for the structure determination of the complex even without accurate knowledge of the structure of the bare molecule. Based on the symmetry arguments we assumed for teracene-Ar complex $y = 0$, while x and z were fitted using Eq. [6] from Ref. [19]. The necessary moments of inertia of the complex were calculated from the results of Table 2.1 and the moments of inertia of the bare tetracene were taken from Ref. [9]. The results are given in Table 2.2. The Ar atom is located above the center of one of the inner rings in tetracene and the distance from the tetracene plane equals 3.42 Å. The results of the simple model calculation (3.43 Å) compare very well with the experimentally determined value.

Since tetracene consists of four benzene-like rings we can expect a similar interactions within the complex as in the benzene-Ar complex. Weber *et al.* [4] obtained an Ar to benzene distance of 3.581 Å from the rotationally resolved studies of

---

[2]The rotational constants (A_g) are related to the corresponding moments of inertia (I_g) by $A_g = \hbar^2/2I_g$.
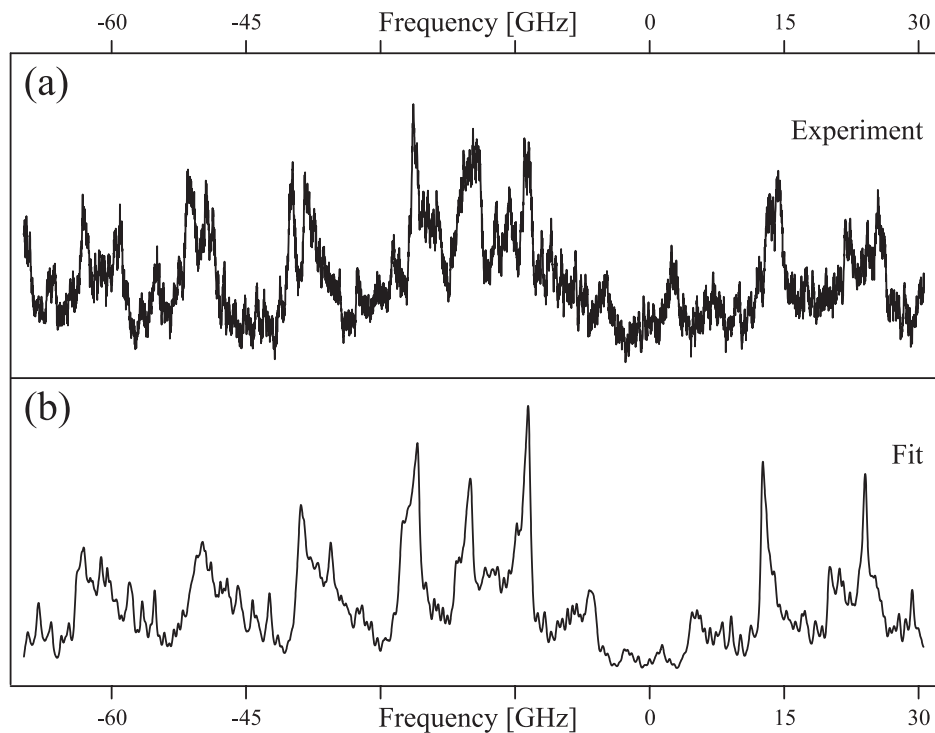
Figure 2.1: Comparison of the experimental (a) and calculated (b) spectra of the 0-0 band in the tetracene-Ar complex. The origin of this band is located at 22 354.86 cm^{-1}. The parameters for the calculated spectrum are taken from Table 2.1.

the benzene-Ar complex. This is consistent with an earlier microwave measurement (3.586 Å) [5]. The benzene-Ar complex was also studied theoretically by Koch *et al.* [20, 21]. They have calculated by the *ab initio* coupled cluster method the geometry, potential energy surface and dissociation energy for the benzene-Ar complex. The result for the distance of Ar to benzene plane was 3.555 Å.

It is clear that the presently obtained geometry of the tetracene-Ar complex compares very well with that of the benzene -Ar complex. The results suggest a shortening of the Ar – ring plane distance in tetracene compared to benzene. This might be explained by the attractive interactions of the other rings of tetracene.

Table 2.1: Rotational constants in the ground (S_0) and excited state (S_1) of the tetracene-Ar and tetracene-Kr complexes ($\Delta A = A' - A''$, $\Delta B = B' - B''$, $\Delta C = C' - C''$). All values are expressed in MHz. The estimated uncertainties are 1 MHz and 0.1 MHz for the rotational constants and Δ's, respectively.

tetracene-Ar				tetracene-Kr			
S_0		S_1		S_0		S_1	
A''	718	ΔA	−22.1	A''	468	ΔA	−29.7
B''	189	ΔB	−0.8	B''	180	ΔB	1.2
C''	178	ΔC	2.6	C''	154	ΔC	−4.1

Table 2.2: The noble gas position in tetracene-Ar and tetracene-Kr complexes. All values are expressed in Å. The (x, y, z) frame is defined in the text. The uncertainties are approximated to 0.1 and 0.2 Å for the tetracene-Ar and -Kr complexes, respectively.

	Argon	Krypton
x	3.42	3.65
y	0	0
z	1.2	1.2

2.3.3   Tetracene-Kr complex

The procedure used for analysis of the tetracene-Kr complex was similar to that of tetracene-Ar. Based on the simple theoretical model the distance between tetracene molecule and Kr atom in the complex was estimated to 3.50 Å. Again we fixed the transition type in the tetracene-Kr complex to a b-type. The GA was not of much use for the assignment of the tetracene-Kr spectra. The reason is basically the strong overlap of very many lines. This is discussed in some more detail below.

Unlike with tetracene-Ar the JB95 program did not allow us to unambiguously determine a unique set of physically acceptable parameters for the tetracene-Kr complex. With different sets of parameters we were more or less able to simulate the experimental spectrum, although a perfect simulation was never realized. The reason
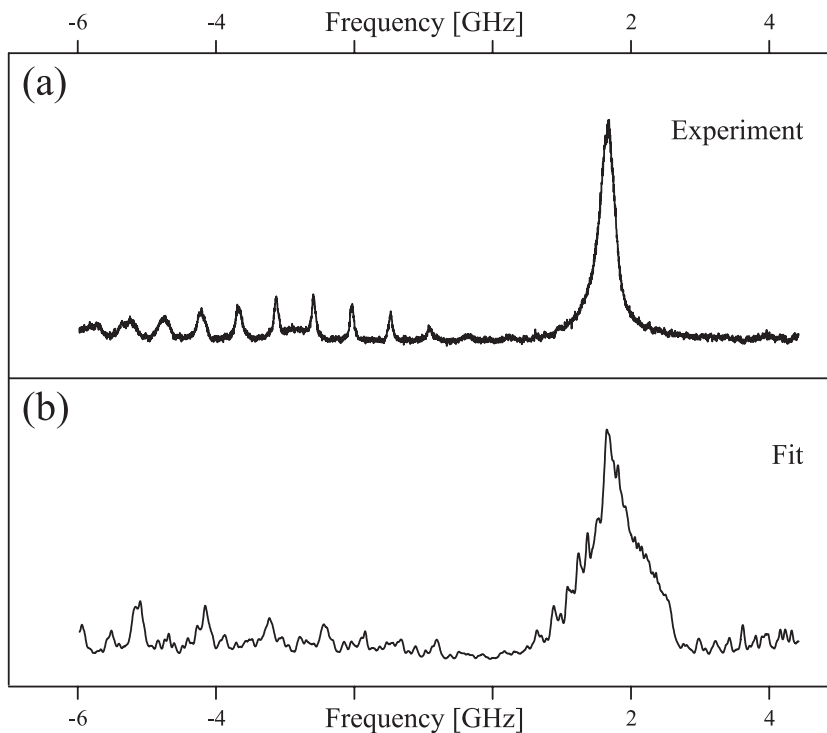
Figure 2.2: Comparison of the experimental (lower panel) and calculated (upper panel) spectra of the 0-0 band in the tetracene-Kr complex. The origin of this band is located at 22 329.63 cm^{-1}. For the calculated spectrum we used the set of physically acceptable parameters given in Table 2.1.

is found in the structure of the observed spectrum. It can be seen from Fig. 2.2 that very few spectroscopic features are present. This is caused by a strong overlap of very many individual lines. A reproduction of about 10 broad peaks (full width at half maximum $\geqslant$ 70 MHz) using thousands of lines with comparable intensities, which is characteristic for a b-type transition, may be achieved with more than one set of parameters. Fortunately, most of the sets lead to physically unacceptable values. The results, presented in Table 2.1, yield the best overall agreement with the experimental spectrum as well as a set of physically significant parameters.

During the analysis of our spectrum we noticed that in general we obtained better results using a two temperature model [22] for the calculated intensities. This is understandable since we know from our previous experience [22] that in the molecular beam higher J-states are cooled less efficiently than lower J-states. This results in a

non-Boltzmann rotational states population. The typical values used in the analysis of tetracene-Kr complex spectrum were: $T_1 = 3.6$ K, $T_2 = 11$ K and W= 0.4.

Using the obtained rotational constants (see Table 2.1) we calculated the distance between Kr atom and the tetracene molecular plane to 3.65Å (see Table 2.2). This distance compares quite well with: 3.676 Å in benzene-Kr [4], 3.977 Å in CO-Kr [23] and 4.573 Å in HCN-Kr [24]. One actually would like to compare the difference in the distances between Ar and Kr atoms to tetracene in the tetracene-Ar, Kr complexes. This difference for the tetracene-Ar, Kr is 0.2 Å. In the other complexes it evaluates to 0.1 Å, 0.13 Å and 0.2 Å for benzene, CO and HCN, respectively. Although our result for tetracene-Kr seems to be acceptable, we would like to emphasize that a unique fit of the data for tetracene-Kr cluster was not achieved.

The assignment of two other rovibronic bands: 311 and 471 cm^{-1} was not obtained. Unlike in tetracene-Ar the 311 cm^{-1} band is completely different from the 0-0 band. It consists of some unrecognizable broad shallow patterns on high background. The 471 cm^{-1} shows up a small hump on a broad background, without any further structure. The reason for this behavior has already been discussed by van Herpen *et al* [9]. The main distortions in the spectra may be attributed to $S - T$ intersystem crossing, $S_1 - S_0$ state mixing or even to a coupling of the S_1 state with higher energy levels. Although the distortions in the tetracene-Ar spectrum are small, they are much stronger in the tetracene-Kr, especially in the 311 and 471 cm^{-1} bands. In general they become more pronounced with the higher energy states and with the heavier rare gas atoms. The fact that the coupling with the background states is more pronounced in the Kr complexes than in the Ar complexes may be connected with a different polarizabilities of these atoms. For the more detailed discussion of that problem we refer to Ref. [9].

2.4   Conclusions

With the help of fast modern computers and recently developed software tools we were able to analyze the high resolution spectra of tetracene-Ar and tetracene-Kr van der Waals complexes. The rotational parameters of the 0-0 and 311 cm^{-1} bands in tetracene-Ar complex were determined using the GA and the JB95 programs. Based on these parameters the structure of the complex could be determined. The obtained structure for the tetracene-Ar complex compares very well with the geometry of the benzene-Ar. The distance of Ar to the tetracene plane in the complex is slightly shorter than in the benzene-Ar complex. This suggests a stronger dispersion interaction between Ar and tetracene caused by the other rings.

Although it was not possible to obtain a unique set of rotational parameters in the tetracene-Kr case, physically acceptable values were found that allow for a good estimate of the position of the Kr atom in the tetracene-Kr complex. This estimate agrees with the results from other van der Waals complexes with Kr, like: benzene-Kr,

CO-Kr and HCN-Kr. Especially the difference in the distances between the rare gases (Ar, Kr) and the aforementioned molecules (and tetracene) was in a good agreement.

Due to the considerable distortions in the 311 and 471 cm^{-1} rovibronic bands of tetracene-Kr complex the assignment of these spectra was not possible. The distortions are attributed to the S_1 state interactions with background states.

References

[1] N. Ben-Horin, U. Even, and J. Jortner. Spectroscopy and nuclear dynamics of tetracene-rare gas heteroclusters. *J. Chem. Phys.*, 97:5296–5315, 1992.

[2] M. Hartmann, A. Lindinger, J. P. Toennies, and A. F. Vilesov. Laser-induced fluorescence spectroscopy of van der Waals complexes of tetracene-Ar (n $\leqq$ 5) and pentacene-Ar within ultracold liquid he droplets. *Chem. Phys.*, 239:139–149, 1998.

[3] H. J. Neusser and K. Siglow. High-resolution ultraviolet spectroscopy of neutral and ionic clusters: Hydrogen bonding and the external heavy atom effect. *Chem. Rev.*, 100:3921–3942, 2000.

[4] Th. Weber, E. Riedle, H. J. Neusser, and E. W. Schlag. Van der Waals bond lengths and electronic spectral shifts of the benzene-Kr and benzene-Xe complexes. *Chem. Phys. Lett.*, 183:77–83, 1991.

[5] Th. Brupbacher and A. Bauder. Rotational spectrum and dipole moment of the benzene-argon van der Waals complex. *Chem. Phys. Lett.*, 173:435–438, 1990.

[6] A. Amirav, U. Even, and J. Jortner. Energetics and intramolecular dynamics of the isolated ultracold tetracene molecule in its first excited singlet state. *J. Chem. Phys.*, 75:3770–3793, 1981.

[7] I. Raitt, A. M. Griffiths, and P. A. Freedman. The electronic spectra of argon-tetracene van der Waals complexes. *Chem. Phys. Lett.*, 80:225–228, 1981.

[8] A. Amirav and J. Jortner. Non-additivity of spectral shifts of tetracene·Ar$_n$ complexes. *Chem. Phys.*, 85:19–22, 1984.

[9] W. M. Van Herpen, W. Leo Meerts, and A. Dymanus. Rotationally resolved laser spectroscopy of teracene and its van der Waals complexes with inert gas atoms. *J. Chem. Phys.*, 87:182–190, 1987.

[10] R. Helm, H. P. Vogel, and H. Neusser. Highly resolved UV spectroscopy: structure of S_1 benzonitrile and benzonitrile-argon by correlation automated rotational fitting. *Chem. Phys. Lett.*, 270:285–292, 1997.

[11] J. A. Hageman, R. Gelder, W. L. Meerts, and L. M. C. Buydens. Direct determination of molecular constants from rovibronic spectra with genetic algorithms. *J. Chem. Phys.*, 113:7955–7962, 2000.

[12] D. F. Plusquellic, R. D. Suenram, B. Mate, J. O. Jensen, and A. C. Samuels. The conformational structures and dipole moments of ethyl sulfide in the gas phase. *J. Chem. Phys.*, 115:3057–3067, 2001.

[13] J. P. Bekooy, W. L. Meerts, and A. Dymanus. High-resolution laser-rf spectroscopy on the $A^2\Pi_{3/2} - X^2\Pi_{3/2}$ system of iodine oxide (IO). *J. Mol. Spectrosc.*, 102:320–343, 1983.

[14] W. A. Majewski and W. L. Meerts. Near-UV spectra with fully resolved rotational structure of naphthalene and perdeuterated naphthalene. *J. Mol. Spectr.*, 104:271–281, 1984.

[15] R. Wehrens and L. Buydens. Evolutionary optimisation: a tutorial. *Trends Anal. Chem.*, 17:193–203, 1998.

[16] K. Harris, R. Johnston, and B. Kariuki. The genetic algorithm: Foundations and apllications in structure solution from powder diffraction data. *Acta Crystallogr., Sect. A: Found. Crystallogr.*, 54:632–645, 1998.

[17] Y. R. Wu and D. H. Levy. Determination of the geometry of deuterated tryptamine by rotationally resolved electronic spectroscopy. *J. Chem. Phys.*, 91:5278–5284, 1989.

[18] M. J. Ondrechen, Z. Berkovitch-Yellin, and J. Jortner. Model calculations of potential surfaces of van der Waals complexes containing large aromatic molecules. *J. Am. Chem. Soc.*, 103:6586–6592, 1981.

[19] W. L. Meerts, W. M. Van Herpen, and A. Dymanus. The structure of uorene ($C_{13}H_{10}$) and the uorene-argon van der Waals complex from a high resolution near UV spectrum. *Can. J. Phys.*, 62:1293–1299, 1984.

[20] H. Koch, B. Fernandez, and O. Christiansen. The benzene-argon complex: A ground and excited state ab initio study. *J. Chem. Phys.*, 108:2784–2790, 1998.

[21] H. Koch, B. Fernandez, and J. Makarewicz. Ground state benzene-argon intermolecular potential energy surface. *J. Chem. Phys.*, 111:198–204, 1999.

[22] G. Berden, W. L. Meerts, and E. Jalviste. Rotationally resolved ultraviolet spectroscopy of indole, indazole, and benzimidazole: Inertial axis reorientation in the $S_1(^1L_b) \leftarrow S_0$ transitions. *J. Chem. Phys.*, 103:9596, 1995.

[23] M. D. Brookes and A. R. W. McKellar. Infrared spectra of the Kr-CO and Xe-CO van der Waals complexes. *Mol. Phys.*, 97:127–137, 1999.

[24] E. J. Cambell, L. W. Buxton, and A. C. Legon. [83]Kr nuclear quadrupole coupling, microwave spectrum, and structure of KrHCN. *J. Chem. Phys.*, 78:3483–3493, 1983.

THREE

Rotational isomers of hydroxy deuterated o- and m-cresols studied by ultraviolet high resolution experiments [1]

Abstract

The laser induced fluorescence spectra of several torsional transitions of the $S_1 \leftarrow S_0$ electronic transition were recorded for the hydroxy deuterated o- and m-cresols. Both *cis* and *trans* rotamers were observed in a high resolution molecular beam experiment. The spectra were analyzed using a genetic algorithm assisted automatic assignment. The Hamiltonian used included rotational, torsional and rotation-torsion components. Both, high resolution rotationally resolved spectra and low resolution torsional frequencies, were combined to obtain the rotational constants, the direction of the methyl group axis, and the V_3 and V_6 barriers to internal rotation of the methyl top in the ground (S_0) and excited (S_1) states. The lifetime of the S_1 state is also reported. Quantum interference effects due to the interaction of the internal and overall rotation allowed for determination of the absolute sign of the angle between transition moment and the a principal axis.

3.1 Introduction

A large number of spectroscopic studies have been performed on substituted phenols. Of particular interest are substitutions in *ortho*- and *meta*-positions, because of the existence of *cis – trans* isomerism. Another important issue is the internal rotation

of symmetric top groups attached to the benzene ring, like -CH$_3$. These two features meet in the *o*- and *m*-cresol molecules.

The *cis* and *trans* orientations of the hydroxy group were already predicted for some phenol derivatives in the thirties of the last century [1]. Similarly, in that decade the barrier to internal rotation of the methyl group was measured for the first time (for ethane) by Kemp and Pitzer [2]. Since then, phenol and toluene derivatives, among many other molecules, were shown to exhibit one or both of these characteristics.

The low resolution spectra of the *o*- and *m*-cresols were examined by many groups [3–7]. Both, *cis* and *trans* rotamers were identified and torsional parameters like the barrier to internal rotation (V_{3i}, $i = 1, 2$) and the reduced rotational constant (F) of the methyl top were obtained for the ground (S_0) and excited electronic (S_1) states. Microwave spectra of *o*-cresols and their hydroxy deuterated isotopomers were recorded by Welzel *et al.* [8]. From these spectra accurate rotational and torsional parameters for the undeuterated and hydroxy deuterated *o*-cresols in the ground electronic state were determined.

The low resolution spectra revealed a drastic change of the barriers for the internal rotation upon electronic excitation from S_0 to S_1. This is consistent with the barriers derived for the other substituted toluenes, like fluorotoluenes [9, 10], toluidines [11] and tolunitriles [12]. For example, in *trans o*-cresol the internal rotation is strongly hindered ($V_3^{''} = 355$ cm^{-1}) in the ground state [4]. However, it decreases in the S_1 state by a factor of about four. On the other hand, the methyl rotor in *trans m*-cresol is almost free in S_0 ($V_3^{''} = 11$ cm^{-1}), but it is strongly hindered in S_1 ($V_3^{'} = 213$ cm^{-1}) [3]. These changes could not simply be explained by steric effects. Several groups treated the problem theoretically [13–15]. Recently, Nakai and Kawai [16, 17] proposed the $\pi^* - \sigma^*$ hyperconjugation (HC) mechanism for *ortho* and *meta* substituted touluenes, which explains the aforementioned barrier changes upon the electronic excitation. Originally hyperconjugation was postulated to be the reason for conformational preferences in propene by Hehre *et al.* [13].

Rotationally resolved UV laser induced fluorescence (LIF) spectra provide accurate rotational constants for the ground and excited states of the examined molecules [18, 19], from which structural information can be deduced. Other important parameters like magnitude and direction of the transition moment (TM, to within its sign) and lifetime of the S_1 state can be determined [20]. Perturbations in the rotational spectra caused by internal rotation effects allow for more parameters to be derived [21]. Especially when combined with higher torsional transition frequencies they provide an accurate determination of the direction of the methyl top axis, the internal rotation constant, the barrier heights in the both electronic states and even the absolute direction of TM. The latter is obtained from quantum interference effects [21, 22]. In this paper we present frequency and intensity analysis of the high resolution, rotationally resolved LIF spectra of different torsional members of the $S_1 \leftarrow S_0$ transition in hydroxy deuterated *o*- and *m*-cresols.
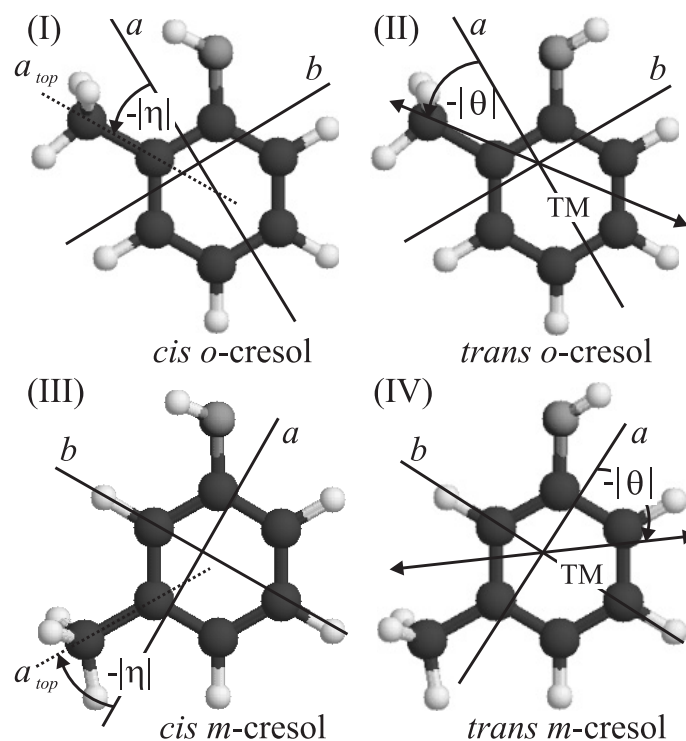
Figure 3.1: Structures of *trans* and *cis* rotamers of hydroxy deuterated *o*- and *m*-cresols. The principal axes are denoted by a, b, c, with c perpendicular to the benzene frame. Both angles, η and θ, are taken to be positive in the sense of rotation direction from a to b axis.

The experimental spectra were analyzed with the help of Genetic Algorithm (GA) based automatic fitting procedures. These GA-fits are superior to classical assignments for very dense spectra and they allowed a fast and easy assignment for the split spectra observed in this work.

3.2 Theory

3.2.1 Model

All cresols studied are assumed to consist of the rigid planar frame (phenol) with a methyl group attached to it. The axis of the internal rotation of this methyl top

a_{top} is in the plane of the benzene ring and makes an angle η with the a principal axis (see Fig. 3.1). Since the electronic excitation takes place in the planar benzene chromophore we also assume the transition moment in the ab plane and with an angle θ with the a principal axis (Fig. 3.1). The implemented model utilizes the principal axes of the molecule as a reference coordinate system (PAM method). The derived rotational constants do not include contributions from internal rotation and are directly related to the geometry of the molecule. Only the main features of the theory are presented below and more details can be found in [21, 23, 24].

The Hamiltonian, which describes the rotation-torsion problem consists of three parts: the rotational part H_r, the torsional part H_t and the coupling term between overall and internal rotation H_{rt}

$$H = H_r + H_t + H_{rt}, \tag{3.1}$$

where

$$\begin{aligned}
H_r &= AJ_a^2 + BJ_b^2 + CJ_c^2 + F(\vec{\rho} \cdot \vec{J})^2, \\
H_t &= FJ_\alpha^2 + \frac{1}{2} \sum_{i=1,2} V_{3i}(1 - \cos 3i\alpha), \\
H_{rt} &= -2F\vec{\rho} \cdot \vec{J}J_\alpha.
\end{aligned} \tag{3.2}$$

where A, B, C are the rotational constants, J_g ($g = a, b, c$) are the projections of the total angular momentum $\vec{J}$ on the principal axes of inertia of the molecule and vector $\vec{\rho}$ has the following components

$$\rho_g = \frac{\cos \eta_g I_\alpha}{I_g}. \tag{3.3}$$

In the last equation I_α is the moment of inertia of the internal rotor and I_g are the principal moments of inertia of the whole molecule. For the cresol molecules $\eta_c = 0$, $\eta_a = \eta$, hence $\eta_b = 90 - \eta$. The reduced rotational constant for internal rotation F is defined as

$$F = \frac{\hbar^2}{2rI_\alpha} = \frac{F_\alpha}{1 - I_\alpha \sum_g \cos^2 \eta_g / I_g}. \tag{3.4}$$

J_α is the angular momentum of the internal rotor defined by $J_\alpha = -i\hbar \frac{\partial}{\partial \alpha}$ where α is the torsional angle and V_3 and V_6 are the three- and six-fold barrier heights of the periodic torsional potential.

A perturbation approach [18, 21, 23, 24] is used to derive the energy for (3.1). At first, the torsional Hamiltonian H_t is solved and the coupling between the internal and overall rotation H_{rt} is treated as the perturbation on the rotational Hamiltonian H_r.

As a result one can construct an effective rotational Hamiltonian for every torsional state (labelled with $\nu\sigma$)

$$H_{\nu\sigma} = AJ_a^2 + BJ_b^2 + CJ_c^2 + F\sum_{n=1}^{\infty} W_{\nu\sigma}^{(n)}(\rho_a J_a + \rho_b J_b)^n, \qquad (3.5)$$

where $W_{\nu\sigma}^{(n)}$ are the n-th order perturbation coefficients for the $\nu\sigma$ state. As shown in Ref. [23] these coefficients can be expressed as matrix elements of the internal rotation angular momentum operator J_α in the torsion-rotation basis. Here, ν labels the torsional level in the high barrier limit and σ takes the values $-1, 0, +1$. States with $\sigma = 0$ are nondegenerate of a symmetry and with $\sigma = \pm 1$ are two-fold degenerate of e symmetry. In the following we will label the levels with A and E.

In the calculations the Hamiltonian (3.5) is restricted to fourth order. In that case matrix elements (see Appendix B of Ref. [24]) connect rotational basis functions up to $\Delta K = 4$. A matrix of size $(2J+1) \times (2J+1)$ has to be diagonalized for every J for the νa and νe torsional states. The resulting eigenvalues are ordered with increasing energies and labelled with K_a and K_c as in a normal asymmetric rotor (for details see [25]).

3.2.2   Internal rotor effects

The transition frequencies follow the selection rules $\Delta J = 0, \pm 1$. Since the transition moment does not depend on the internal rotor angle additionally $\Delta\sigma = 0$ holds. We therefore expect for the $S_1 \leftarrow S_0$ origin two, more or less overlapping subbands, each with its own rotational structure. These subbands ($0a_1 \leftarrow 0a_1$ and $0e \leftarrow 0e$, A and E subbands, respectively) are separated by $\Delta\nu_0^{EA} = \Delta E'_{EA} - \Delta E''_{EA}$, where ΔE_{EA} are $E - A$ energy differences in the excited and ground states, respectively. If $\Delta\nu_0^{EA}$ is small both spectra partially overlap like in the o-cresols. A large value causes a complete separation of the subspectra as in the m-cresols. Furthermore, a decrease of the barrier upon electronic excitation results in a blue-shift of the E subband with respect to the A subband as observed in the o-cresols. For the m-cresols we observe a red-shift of the E subband and hence an increase of the torsional barrier upon electronic excitation.

The A- and E-subband pair have a different rotational structure. For the A states the odd perturbation coefficients vanish [23, 24] and it follows that this A subband has an asymmetric rigid rotor-like structure with effective rotational constants

$$\begin{aligned}
A_A &= A + FW_A^{(2)}\rho_a^2, \\
B_A &= B + FW_A^{(2)}\rho_b^2, \\
C_A &= C + FW_A^{(2)}\rho_c^2.
\end{aligned} \qquad (3.6)$$

However, for the E states all the perturbation coefficients are nonzero giving rise to linear terms in K_a. This causes mixing of the rigid rotor wavefunctions, which induces transitions forbidden for a normal asymmetric rigid rotor [21].

For a transition moment in the ab plane (Fig. 3.1) the line strengths are given by

$$
\begin{aligned}
A_{R''R'} &\propto |\mu_a\langle R'|\Phi_{Za}|R''\rangle|^2 + |\mu_b\langle R'|\Phi_{Zb}|R''\rangle|^2 + \\
&+2\mu_a\mu_b\langle R'|\Phi_{Za}|R''\rangle\langle R'|\Phi_{Zb}|R''\rangle,
\end{aligned} \tag{3.7}
$$

here the Z axis is the space-fixed axis determined by the laser polarization direction, $|R\rangle \equiv |J, K_a, K_c\rangle$, $\mu_a = \mu\cos\theta$, $\mu_b = \mu\sin\theta$, and μ is the absolute value of the TM. Φ_{Zg} are the direction cosines between the laboratory Z axis and the molecular g axis. Eq. (3.7) differs from the usual rigid rotor expression by an extra third term, the so-called interference term. As first pointed out by Plusquellic *et al.* [22] and later by Remmers *et al.* [21] the interference term can be used to determine the absolute sign of the θ angle. This is because $\mu_a\mu_b = 1/2\mu^2\sin\theta\cos\theta$ and therefore changes sign with θ. The interference term is non-zero only for the E transitions. The final intensities are obtained by multiplying the line strengths with the temperature dependance. We used the two-temperature model defined in Ref. [26].

3.2.3   Computational approach

All the observed rotational spectra were fitted using GA based program. In general, the GA is a global optimizer, which uses concepts copied from the natural reproduction and selection processes. For a description of the GA the reader is referred to the original literature [27–29]. A more detailed description of the GA application to the fitting of high resolution spectra can be found in Ref. [30, 31]. Here, we only present the most important aspects of the GA fitting philosophy.

In the GA program each parameter from the model described in Sec. (3.2.1) is represented by a gene. A vector of parameters (genes) that describe one spectrum is called a chromosome and a set of typically 300 chromosomes forms a population. Initially, all the parameters in the population are set randomly between limits imposed by a user. These limits depend on the degree of complication of the rotational spectra and can be as large as $\pm 10\%$ of the centrally chosen value. In practice, hardly any prior knowledge on the values of the parameters is required.

In the next step all the chromosomes from the population are evaluated by a fitness function F_{fg} (or cost function C_{fg}). This function is very critical for the GA to be successful. A more elaborate discussion on the choice of the cost function can be found elsewhere [30, 31]. The function used here is defined by Hageman *et al.* [30] and can in the mathematical shorthand form be expressed as [31]

$$
F_{fg} = \frac{(\boldsymbol{f}, \boldsymbol{g})}{\|\boldsymbol{f}\|\,\|\boldsymbol{g}\|}, \tag{3.8}
$$

where $\boldsymbol{f}$ and $\boldsymbol{g}$ represent the experimental and calculated spectra, respectively. The inner product $(\boldsymbol{f}, \boldsymbol{g})$ is defined with the metric $\boldsymbol{W}$

$$(\boldsymbol{f}, \boldsymbol{g}) = \boldsymbol{f}^T \boldsymbol{W} \boldsymbol{g} \tag{3.9}$$

and the norm of $\boldsymbol{f}$ defined as $\|\boldsymbol{f}\| = \sqrt{(\boldsymbol{f}, \boldsymbol{f})}$ (a similar definition holds for $\boldsymbol{g}$). $\boldsymbol{W}$ has the matrix elements $W_{ij} = w(|j - i|) = w(r)$. For $w(r)$ we used a triangle function [30] with a user controlled width of the base Δw

$$w(r) = \begin{cases} 1 - |r| / \left(\frac{1}{2}\Delta w\right) & \text{for } |r| \leqslant \frac{1}{2}\Delta w \\ 0 & \text{otherwise.} \end{cases} \tag{3.10}$$

After evaluation of the each chromosome from the population, the best solutions are kept for the next GA generation. This elitism prevents them from being lost and also chooses the best parents to be combined in the following crossover process. We use a two-point crossover, after which we apply a small number of mutations into just "born" chromosomes. Next the GA cycle (generation) repeats. For the cresol spectra we mostly set the maximum number of generations to 500.

The fitting approach to the experimental data was as follows. At first, we fit the A-subband of the $S_1 \leftarrow S_0$ origin to an effective asymmetric rigid rotor. Although this did not result in proper values for the rotational constants, it gave an indication which lines in the complicated rotational spectra belong to the A-subband. From the preliminary $0a_1 \leftarrow 0a_1$ subband fit the leftover E lines could be easily identified and the origin of the $0e \leftarrow 0e$ transition could be estimated. Hence this yielded an estimate of the torsional splitting $\Delta\nu_0^{EA}$. Combining these results and the knowledge of some torsional parameters from the literature a simultaneous GA fit of the $0a_1 \leftarrow 0a_1$ and $0e \leftarrow 0e$ subbands was quickly successful.

Line positions obtained from the GA fits were subsequently manually compared with the observed spectra and corrected if needed. Spectra of the higher torsional states ($1e \leftarrow 0e$ and $2a_1 \leftarrow 0a_1$ transitions) were also fit with the GA. Then, all the available data were fit by a separate least-squares based program [20]. Obtained parameters were utilized to improve the torsional origins and to refit all the data. After two or three such a steps a very good to perfect fit could be obtained with parameters that did not change any more within their uncertainties.

After the parameters that determine the line positions were found, we performed a simultaneous GA intensity fit of the $0a_1 \leftarrow 0a_1$ and $0e \leftarrow 0e$ subbands. All the parameters that did not affect the intensity were fixed. The lineshapes were fit using a Voigt profile with a fixed Gaussian contribution of 25 MHz (see Sec. (3.3)). Since the GA performs an intensity fit of the complete spectrum much better information on θ and the linewidth $\Delta_{Lorentz} \equiv \Delta_L$ is obtained than from an intensity fit to some selected individual lines. All errors presented in the paper are calculated from the combined available high and low resolution data.
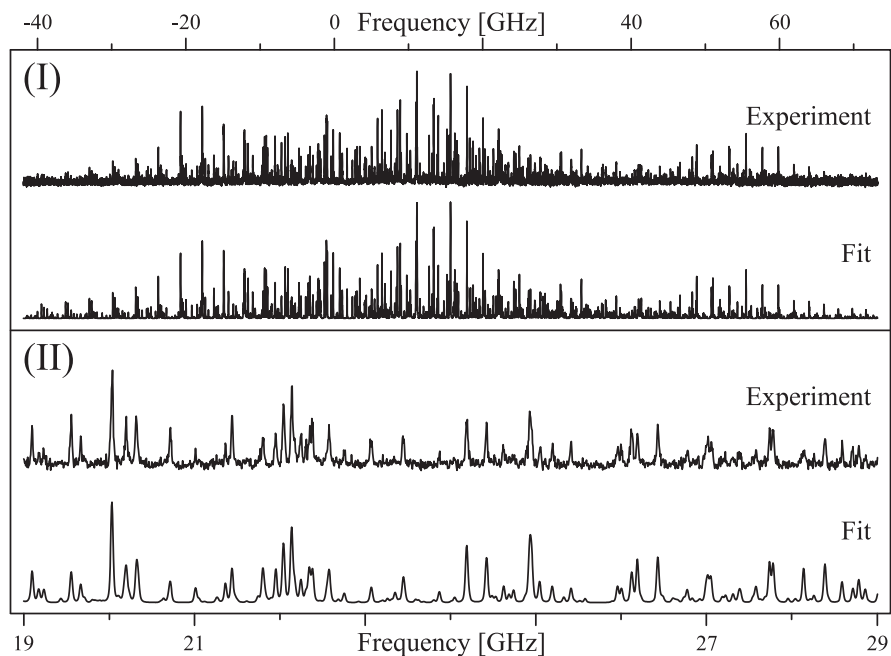
Figure 3.2: Experimental and fitted spectra of hydroxy deuterated *trans o*-cresol. (I) Full spectra. The zero in the frequency scale corresponds to the $0a_1 \leftarrow 0a_1$ origin at $36\,201.093(10)$ cm^{-1}. The $0e \leftarrow 0e$ origin is located at $40.020(7)$ GHz. (II) a 10 GHz zoom-in to the part of the spectrum where both: $0e \leftarrow 0e$ and $0a_1 \leftarrow 0a_1$ spectra overlap.

We would like to note here that although the 'classical' assignment of quantum numbers to the experimental lines is still possible for the studied molecules it would be a very difficult, tedious and long process. If one considers one pair of spectra (A and E subbands) for one deuterated cresol, the 'classical' assignment of such a complicated spectra may easily take a month. Furthermore, assignment of the spectrum helps only for the fit of the higher torsional states of the same cresol molecule, but not for the other molecules. It is clear that only assignment of the rotationally resolved spectra of *cis* and *trans*, *o*- and *m*-cresols might have taken few months to half a year. In contrast the complete GA analysis of all the spectra presented in this publication took about one week. This is quite a gain of time, which can be spent on the actual analysis of the data, formulating hypothesis and making theoretical predictions.

Table 3.1: Deuterated (-OD) *trans* *o*-cresol molecular constants obtained from the combined fit of the rotationally resolved $0a_1 \leftarrow 0a_1$ and $0e \leftarrow 0e$ torsional transitions and origins of the torsional $1e \leftarrow 0e$ and $2a_1 \leftarrow 0a_1$ transitions.

	S_0		S_1	
A''	3 168.41479 [a]	ΔA	$-146.45(27)$	MHz
B''	2 173.76335 [a]	ΔB	$-5.69(23)$	MHz
C''	1 299.79054 [a]	ΔC	$-26.321(84)$	MHz
F_α	5.241053 [b]	ΔF_α	$-0.11491(62)$	cm^{-1}
V_3	371.047 [a]		83.415(14)	cm^{-1}
V_6	0 [c]		$-3.294(51)$	cm^{-1}
$\nu_0^{0a_1 \leftarrow 0a_1}$		36 201.093(10)		cm^{-1}
$\Delta\nu_0^{EA}$		40 019.7(68)		MHz
ΔE_{EA}	436.4(68)		40 456.1(68)	MHz
η	$-30.23(29)$	$\Delta\eta$	0 [c]	deg
θ		$-37.00(29)$		deg
τ		10.6(7)		ns

[a] Constants taken from microwave experiments [8] and fixed in the fit.
[b] Value for toluene [33].
[c] Fixed in the fit.

3.2.4 Ab initio calculations

The structure of *o*- and *m*-cresol in the electronic ground state has been optimized at the HF, MP2/6-31G(d,p) levels and at the CIS/6-31G(d,p) level for the electronically excited S_1-state with the Gaussian 98 program package (Revision11) [32]. The SCF convergence criterion used throughout the calculations was an energy change below 10^{-8} Hartree, while the convergence criterion for the gradient optimization of the molecular geometry was $\partial E/\partial r < 1.5 \cdot 10^{-5}$ Hartree/Bohr and $\partial E/\partial \varphi < 1.5 \cdot 10^{-5}$ Hartree/degrees, respectively.
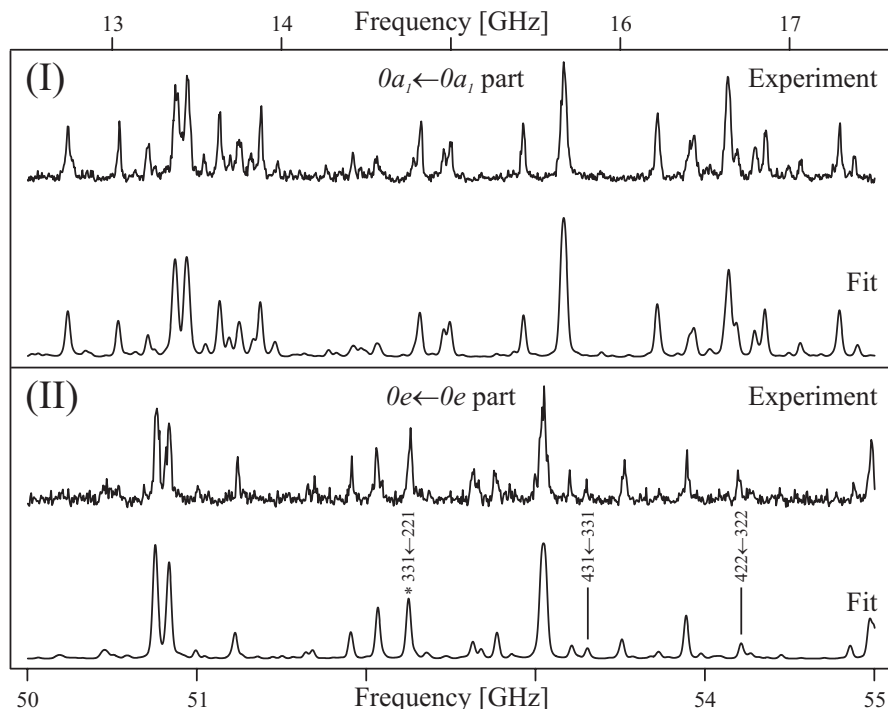
Figure 3.3: Effects of the -CH$_3$ group internal rotation. Part of the R-branch of (I) the $0a_1 \leftarrow 0a_1$ and (II) the $0e \leftarrow 0e$ subbands of hydroxy deuterated *cis o*-cresol spectra. The anomalous lines (see text) are marked with their quantum numbers $(J''K_a''K_c'' \leftarrow J'K_a'K_c')$. Line with asterisk is not a single line. The frequency scale is relative to the $0a_1 \leftarrow 0a_1$ subband origin.

3.3   Experimental setup

The experimental setup for the rotationally resolved LIF is described elsewhere [34]. In short, the apparatus consists of a single frequency ring dye laser (Coherent 899-21), pumped with 6 W of the 514 nm line of an argon-ion laser. Rhodamine 110 is used in the dye laser as a lasing medium. The fundamental light from the dye laser is coupled into an external delta cavity (Spectra Physics) for second harmonic generation (SHG). The UV radiation at ~ 277 nm (for *m*-cresols) and at ~ 275 nm (for *o*-cresols) is generated in this cavity by an angle tuned, Brewster cut BBO crystal. The cavity length is locked to the dye laser frequency by a frequency modulation technique [35, 36].

Table 3.2: Deuterated (-OD) *cis o*-cresol molecular constants obtained from the fit of the rotationally resolved $0a_1 \leftarrow 0a_1$ and $0e \leftarrow 0e$ torsional transitions.

	S_0		S_1	
A''	3 232.91617 [a]	ΔA	$-104.61(22)$	MHz
B''	2 148.84054 [a]	ΔB	$-28.40(17)$	MHz
C''	1 301.65739 [a]	ΔC	$-26.710(62)$	MHz
F_α	5.241053 [b]	ΔF_α	0 [c]	cm^{-1}
V_3	669.10 [a]		88.8776(38)	cm^{-1}
$\nu_0^{0a_1 \leftarrow 0a_1}$		36 407.593(10)		cm^{-1}
$\Delta\nu_0^{EA}$		37 579.7(26)		MHz
ΔE_{EA}	15.4(26)		37 595.1(26)	MHz
η	$-31.76(12)$	$\Delta\eta$	0 [c]	deg
θ		$-45.65(12)$		deg
τ		14.9(14)		ns

[a] Constants taken from microwave experiments [8] and fixed in the fit.
[b] Value for toluene [33].
[c] Fixed in the fit.

The undeuterated cresols used in the experiment are commercially available substances. In order to substitute a hydrogen atom from cresols' -OH group with a deuterium atom, they are mixed with D_2O in the source container. To increase the vapour pressure of cresols, the source is heated to 110° C. Subsequently, the molecular beam is formed by expanding a mixture from the source, seeded in 600 mbar of argon, through a 100 μm hole into the vacuum. The vacuum system is comprised of three differentially pumped vacuum chambers that are linearly connected by two skimmers (1 mm and 2 mm). The skimmers collimate the molecular beam and hence reduce the Doppler contribution to the measured linewidth. The UV laser crosses the molecular beam 360 mm downstream from the nozzle at right angles. The molecular fluorescence is collected perpendicular to the plane defined by the laser and molecular beam by an imaging optics that consists of a concave mirror and two plano-convex lenses. The Doppler contribution to the experimental linewidth in this set-up is 25 MHz of full width at half-maximum (FWHM). The total fluorescence is detected by a photomultiplier tube, whose output is digitized by a photon-counter and send to a PC for data acquisition and processing. The relative frequency is determined with a quasi-
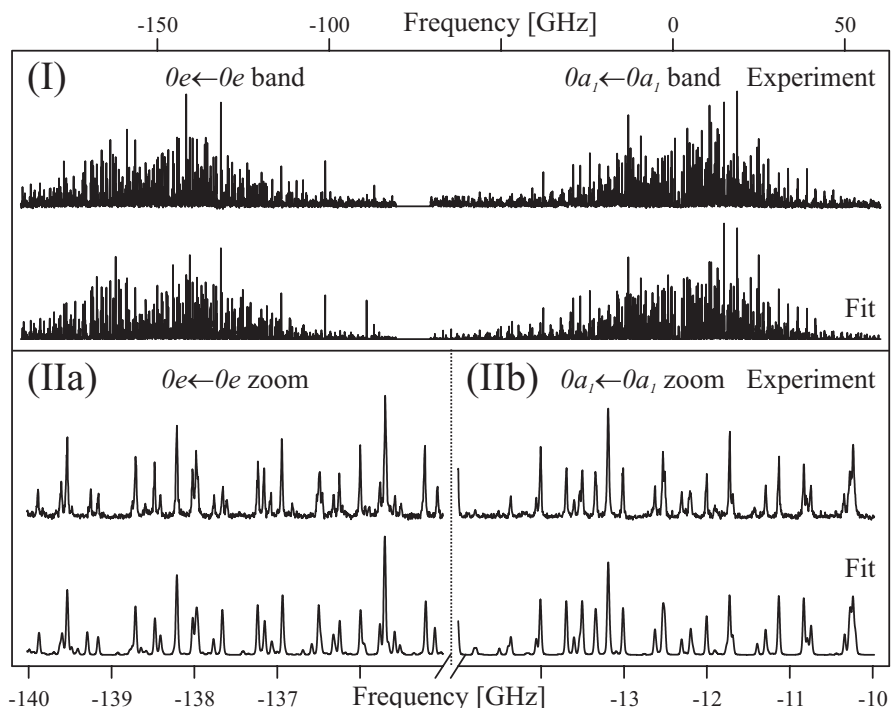
Figure 3.4: Experimental and fitted spectra of hydroxy deuterated *trans m*-cresol. (I) Full spectra with indicated $0e \leftarrow 0e$ and $0a_1 \leftarrow 0a_1$ subbands. The zero in the frequency scale corresponds to the $0a_1 \leftarrow 0a_1$ origin at 36 095.829(10) cm^{-1}. The $0e \leftarrow 0e$ origin is located at $-155.325(300)$ GHz. (II) a 5 GHz zoom-in of (a) the $0e \leftarrow 0e$ and (b) $0a_1 \leftarrow 0a_1$ spectra.

confocal Fabry-Perot interferometer with a free spectral range of 149.9434(56) MHz. For the absolute frequency calibration an iodine spectrum is recorded and compared with the available data [37].

3.4   Results

Four rotationally resolved torsional bands of the hydroxy deuterated   *trans o*-cresol have been measured, *i.e.* $0a_1 \leftarrow 0a_1$, $0e \leftarrow 0e$, $1e \leftarrow 0e$ and $2a_1 \leftarrow 0a_1$. This allowed to determine not only the barriers to internal rotation, but also the torsional constant F in both electronic states. The ground state rotational constants and V_3'' were kept fix at the values of a microwave study [8], $\Delta\eta$ was fixed to zero and F_α'' was fixed to

Table 3.3: Deuterated (-OD) *trans m*-cresol molecular constants obtained from the combined fit of the rotationally resolved $0a_1 \leftarrow 0a_1$ and $0e \leftarrow 0e$ torsional transitions and origins of the torsional $1e \leftarrow 0e$ and $2a_1 \leftarrow 0a_1$ transitions.

	S_0		S_1	
A''	3 653.36(56)	ΔA	$-114.66(30)$	MHz
B''	1 738.36(33)	ΔB	$-18.79(16)$	MHz
C''	1 186.90(20)	ΔC	$-20.570(73)$	MHz
F_α	5.286(12)	ΔF_α	$-0.130(32)$	cm^{-1}
V_3	3.188(180)		204.29(46)	cm^{-1}
V_6	0 $^{a)}$		$-28.42(30)$	cm^{-1}
$\nu_0^{0a_1 \leftarrow 0a_1}$		36 095.829(10)		cm^{-1}
ΔE_{EA}	161 089(300)		5 763(300)	MHz
$\Delta \widetilde{E}_{EA}$		11(300)		MHz
η	$-29.700(79)$	$\Delta \eta$	0 $^{a)}$	deg
θ		$-50.95(10)$		deg
τ		26.7(45)		ns

$^{a)}$ Fixed in the fit.

the value found for toluene [33]. Fig. 3.2 shows the rovibronic spectrum of the split origin of *trans o*-cresol-d_1. The results of the fit to the rovibronic spectrum of the split origin and to the frequencies of the $1e \leftarrow 0e$ and $2a_1 \leftarrow 0a_1$ are presented in Table 3.1.

For the hydroxy deuterated *cis o*-cresol we detected only the $0a_1 \leftarrow 0a_1$ and $0e \leftarrow 0e$ torsional transitions. Like in undeuterated *cis o*-cresol this is due to the weak fluorescence signal from the higher torsional bands of the S_1 state [4]. Because of the limited number of torsional data we had to fix V_6 at zero in the both electronic states, F''_α to a "typical" value for the -CH$_3$ rotor as found for toluene [33] and $\Delta F_\alpha = 0$ [1]. Furthermore, the ground state rotational constants and V''_3 were taken from a microwave study [8] and $\Delta \eta$ was fixed to zero. The final parameters from the simultaneous fit of the both subbands are given in Table 3.2 and a sample of the quality of this fit can be seen in Fig. 3.3. This figure illustrates the appearance of rovibronic transitions that are forbidden in an unperturbed rigid rotor spectrum from

---

[1] ΔP is defined as $P' - P''$, where P represents a particular parameter.
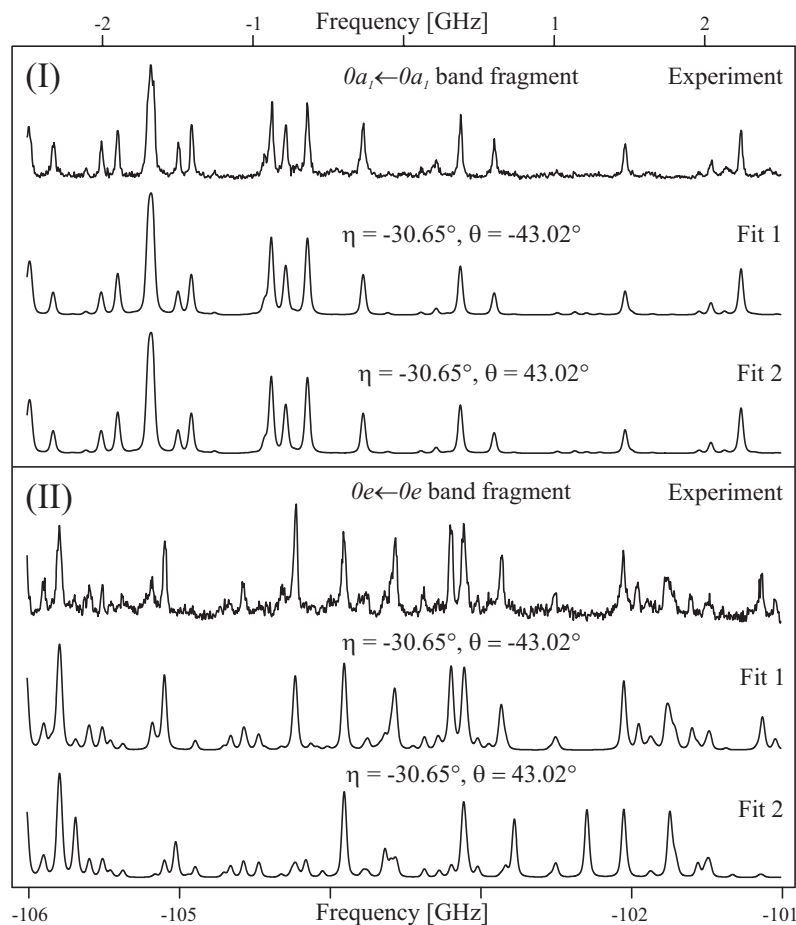
Figure 3.5: Example of the θ angle sign effect on hydroxy deuterated *cis m*-cresol spectra. As predicted from theory the sign of θ has no effect on the $0a_1 \leftarrow 0a_1$ subband intensities (I). In the $0e \leftarrow 0e$ part of the spectrum (II) only "Fit 1" predicts proper line intensities. The frequency scale is given relative to the $0a_1 \leftarrow 0a_1$ subband origin.

linear terms in K_a as described in section 3.2.2.

For the hydroxy deuterated *cis* and *trans m*-cresols we acquired similar torsional spectra as for the hydroxy deuterated *trans o*-cresol. However, the separation between $0a_1 \leftarrow 0a_1$ and $0e \leftarrow 0e$ origins in this case is very large (see Fig. 3.4), resulting in no overlap of the rotational structure of both bands. We pasted together these spectra

Table 3.4: Deuterated (-OD) *cis* *m*-cresol molecular constants obtained from the combined fit of the rotationally resolved $0a_1 \leftarrow 0a_1$ and $0e \leftarrow 0e$ torsional transitions and origins of the torsional $1e \leftarrow 0e$ and $2a_1 \leftarrow 0a_1$ transitions.

	S_0		S_1	
A''	3 573.14(44)	ΔA	$-126.26(20)$	MHz
B''	1 761.84(24)	ΔB	$-9.97(12)$	MHz
C''	1 189.10(16)	ΔC	$-18.583(69)$	MHz
F_α	5.287(12)	ΔF_α	$-0.156(24)$	cm^{-1}
V_3	21.341(52)		221.82(32)	cm^{-1}
V_6	0 $^{a)}$		$-29.77(24)$	cm^{-1}
$\nu_0^{0a_1\leftarrow 0a_1}$		35 980.896(10)		cm^{-1}
ΔE_{EA}	138 123(300)		4 325(300)	MHz
$\Delta \widetilde{E}_{EA}$		$-22(300)$		MHz
η	$-30.647(45)$	$\Delta\eta$	0 $^{a)}$	deg
θ		$-43.02(45)$		deg
τ		9.8(6)		ns

$^{a)}$ Fixed in the fit.

using iodine lines as a reference. This introduced an estimated error of 300 MHz in $\Delta\nu_0^{EA}$. In order to allow for the large error in $\Delta\nu_0^{EA}$ in the simultaneous fits of the $0a_1 \leftarrow 0a_1$ and $0e \leftarrow 0e$ bands we added an additional parameter $\Delta\widetilde{E}_{EA}$ with $\Delta\nu_0^{EA} = \Delta E'_{EA} - \Delta E''_{EA} + \Delta\widetilde{E}_{EA}$. This parameter helped in particular in the beginning of the fit procedure to relax constraints to the V_3 values, which are responsible for the A and E bands splitting and at the same time for the effects in the E band caused by the linear terms in the effective rotational Hamiltonian (Eq. 3.5). The final values of $\Delta\widetilde{E}_{EA}$ are on the order of few tens of MHz, which indicates that the estimated errors due to pasting two nonoverlapping spectra are at their upper limit. The final molecular constants for the hydroxy deuterated *trans* *m*-cresol are presented in Table 3.3 and a fit obtained with these parameters is compared with the experimental spectrum in Fig. 3.4.

The parameters for the hydroxy deuterated *cis* *m*-cresol are given in Table 3.4 and a sample of the fit is shown in Fig. 3.5. This figure compares the intensities of A- and E-lines for different relative signs of η and θ. Quantum interference effects are only

Table 3.5: Measured torsional frequencies of hydroxy deuterated *cis* and *trans*, *o*- and *m*-cresols used in the combined low and high resolution fits. All the frequencies are relative to the origins of the $0a_1 \leftarrow 0a_1$ transitions.

transition	*trans ortho*	*cis meta*	*trans meta*	
$0e \leftarrow 0e$	40.0183(68)	$-133.820(300)$	$-155.326(300)$	GHz
$1e \leftarrow 0e$	43.693(10)	72.242(10)	67.858(10)	cm^{-1}
$2a_1 \leftarrow 0a_1$	73.357(10)	142.698(10)	134.686(10)	cm^{-1}

observed for the E-lines. As Fig. 3.5 shows, the fit with $\eta = -30.65°$, $\theta = -43.02°$ and $\eta = -30.65°$, $\theta = 43.02°$ for the A-lines is identical, while it differs considerably for the E-lines. Obviously, only the combination $\eta = -30.65°$ and $\theta = -43.02°$ gives the correct results. All torsional data for the hydroxy deuterated *o*- and *m*-cresols are summarized in Table 3.5.

For all the aforementioned rotationally resolved spectra the GA intensity fit using the two-temperature model yielded typically values for the rotational temperatures $T_1 \sim 1.7$ K, $T_2 \sim 4$ K and for the weighting factor $w \sim 0.1$.

3.5   Discussion

The methyl top barrier to internal rotation is very sensitive to the steric and electronic surrounding of the top. A more symmetric electron density around the carbon to which -CH_3 group is attached generally leads to lower barriers to internal rotation. Barriers to internal rotation for the undeuterated and hydroxy deuterated cresols obtained experimentally and theoretically by other groups [3, 4, 8, 17] are compared in Table 3.6. Not surprisingly, the current values are similar to those from earlier experiments on the undeuterated cresols. Notable is the trend of a reduction of the barrier for hydroxy deuterated *o*-cresols and an increase of the barrier for *m*-cresols with electronic excitation.

The $S_1 \leftarrow S_0$ electronic transition in *m*- and *o*-cresol corresponds to a $\pi^* \leftarrow \pi$ transition. The CIS calculations show, that the first excited singlet state of *cis/trans* *m*- and *o*-cresol is comprised mainly of two configurations: the first arises from a LUMO(χ_3) $\leftarrow$ HOMO(χ_2) excitation, the second arises from a LUMO+1(χ_4) $\leftarrow$

Table 3.6: Comparison of the rotational barriers for the undeuterated and hydroxy deuterated (marked with [a]) *cis* and *trans*, *o*- and *m*-cresols. All values are given in cm^{-1}.

Ref.	*cis ortho*		*trans ortho*	
	V_3''	V_6''	V_3''	V_6''
exp. [4]	600	-30	355	-7
exp. [8]	661.4(38)		369.95(11)	
exp. [8][a]	669.10(50)		371.047(40)	
theor. [17]	629		366	
exp. *this work*[a]	669.10(50)		371.047(40)	
	V_3'	V_6'	V_3'	V_6'
exp. [4]	90	-5	83	-7
exp. [7]	90.2(3)	$-22.1(7)$		
theor. [17]	126		123	
exp. *this work*[a]	88.8776(38)		83.415(14)	
	cis meta		*trans meta*	
	V_3''	V_6''	V_3''	V_6''
exp. [3]	26	-9	11	-8
theor. [17]	37		12	
exp. *this work*[a]	21.341(52)		3.188(180)	
	V_3'	V_6'	V_3'	V_6'
exp. [3]	211	-39	213	-22
theor. [17]	268		241	
exp. *this work*[a]	221.82(32)	$-29.77(24)$	204.29(46)	$-28.42(30)$

HOMO-1(χ_1) excitation. Both configurations contribute significantly to the S$_1$-state:

$$\Psi_e(S_1, cis, ortho) = 0.60328(\chi_2\chi_3) - 0.35717(\chi_1\chi_4)$$
$$\Psi_e(S_1, trans, ortho) = 0.61198(\chi_2\chi_3) - 0.33890(\chi_1\chi_4)$$
$$\Psi_e(S_1, cis, meta) = 0.61041(\chi_2\chi_3) - 0.34334(\chi_1\chi_4)$$
$$\Psi_e(S_1, trans, meta) = 0.60675(\chi_2\chi_3) - 0.35275(\chi_1\chi_4)$$

all with minor contributions from other configurations. Thus, a discussion of the changes of torsional barriers upon electronic excitation has to include at least the
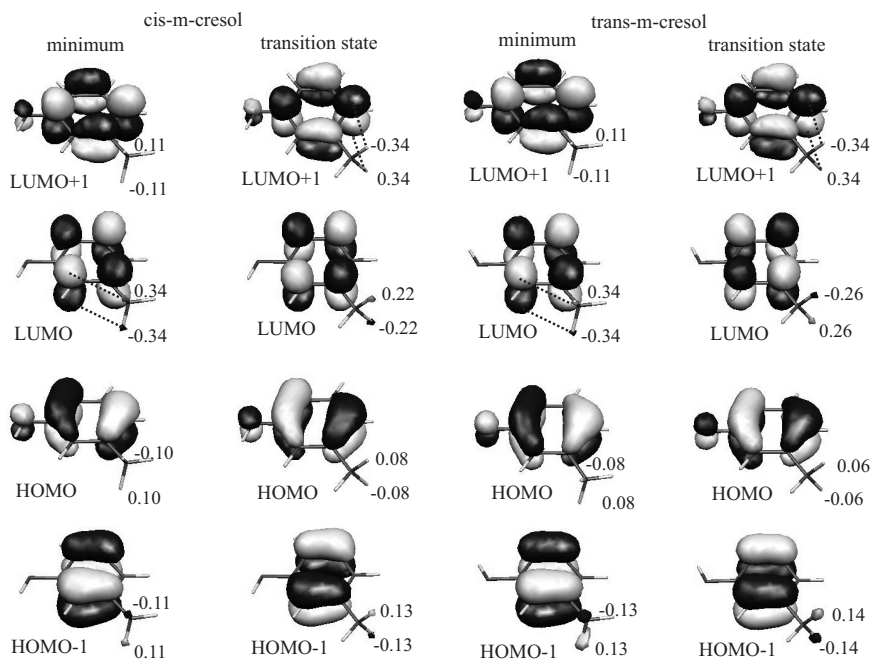
Figure 3.6: Molecular orbitals of *cis* and *trans* *m*-cresol for the minimum conformation ($\alpha = 0°$) and top of the barrier ($\alpha = 60°$). The $\pi^* - \sigma^*$ hyperconjugation is denoted by dotted lines.

above molecular orbitals. We will start with a discussion of the barriers in *m*-cresol, since sterical reasons for the barrier are negligable here. Moreover, the *meta* positions do not communicate electronically with each other in contrast to the *ortho* and *para* positions. Fig. 3.6 shows HOMO-1, HOMO, LUMO, and LUMO+1 of *cis* and *trans* *m*-cresol for torsional angles of 0° (minimum of the potential) and 60° (maximum of the potential). The MO coefficients at the out-of-plane hydrogen atoms of the methyl group have been given numerically in the figure, for sake of clarity. The MO coefficients in the HOMO-1 and HOMO virtually do not change, as has been pointed out by Nakai and Kawai [16, 17]. Large changes can be seen in the LUMO and LUMO+1. For *cis* and *trans* *m*-cresol the coefficients at the out-of-plane hydrogen atoms in the LUMO decrease upon rotation of the methyl group from the minimum conformation to the transitions state. The $\pi^* - \sigma^*$ hyperconjugation, which is responsible for this effect is denoted by the dotted lines in Fig. 3.6. It can be described as a delocalization of the aromatic π^* electrons to the s-type hydrogen atom orbitals of the methyl
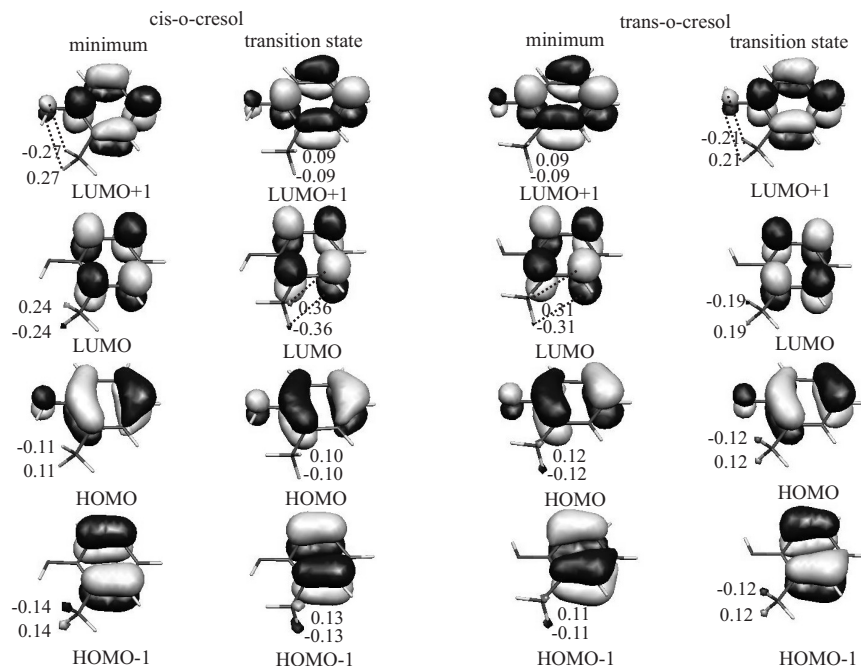
Figure 3.7: Molecular orbitals of *cis* and *trans* o-cresol for the minimum conformation and top of the barrier. The $\pi^* - \sigma^*$ hyperconjugation is denoted by dotted lines.

group. Thus, hyperconjugation stabilizes the equilibrium conformation at 0°, leading to a barrier increase upon electronic excitation, as observed in the experiment. The situation gets more complicated when including the LUMO+1 in the consideration. Here, the transition state conformation at 60° is stabilized, what in priciple should lead to a decrease of the barrier upon electronic excitation. The fact that both effects don't cancel out must be traced back to the different weights, that both configurations contribute to the S_1-state. The above coefficients for the linear combination of configurations show, that the LUMO contributes about three times as much as the LUMO+1. Furthermore, the coefficients show, that both configurations together contribute only to about 50% of the excited state wave function.

The methyl torsional barrier of o-cresol, and especially that of *cis* o-cresol is much more influenced by steric interactions and/or intermolecular hydrogen bonds between the methyl and the hydroxy group than in *m*-cresol. While in *m*-cresol the minimum configuration is the same for the *cis* and *trans* conformers, in *cis* o-cresol the minimum configuration changes between *cis* and *trans*. The in-plane hydrogen atom of the

methyl group pointing towards the OH group describes the transition state for *cis o*-cresol and the minimum for *trans o*-cresol (cf. Fig. 3.7). This has been confirmed by normal mode analysis, which shows a negative frequency for the methyl rotation of the transition state structure of *trans o*-cresol in Fig. 3.7 and only positive frequencies for the minimum structure. The torsion represents the motion which mediates the transition over the top of the potential. The shift of the potential minimum by 60 ° might be explained by the possibility of an additional binding interaction between the in-plane hydrogen of the methyl group and the hydroxy group. For *cis o*-cresol the s-type MO coefficients of the methyl hydrogens in the LUMO increase upon rotation of the methyl group from the minimum to the transition state. This indicates a decrease of the barrier upon electronic excitation as observed in the experiment. On the other hand, the MO coefficients for the LUMO of *trans o*-cresol decrease, implying a barrier increase upon electronic excitation, what can be traced back to the shift of the minimum by 60°.

Tables 3.7 and 3.8 show the calculated ground state rotational constants of *cis* and *trans o*- and *m*-cresol, optimized at the MP2/6-31G(d,p) level of theory. The excited state rotational constants have been calculated with CIS/6-31G(d,p) and the change of the rotational constants upon electronic excitation as the difference of the CIS/6-31G(d,p) and the HF/6-31G(d,p) calculations. The calculated MP2 rotational constants are in very good agreement with the experimental ground state constants. The maximum deviations are 2%. Although the absolute rotational constants of the CIS calculations are in quite bad agreement with the excited state rotational constants, the difference between a HF calculation for the ground state and the CIS calculation for the excited state yields nearly perfect changes of the rotational constants upon electronic excitation. This is due to a cancellation of errors which arises from the neglect of dispersive interactions in both electronic states, but has a great predictive power for the estimation of the changes of rotational constants upon electronic excitation as has been shown to be valid for quite some different molecular systems [38, 39].

Using the program *pKrFit* [40] we determined the structure of *cis* and *trans o*- and *m*-cresol in the S_0 and S_1-states from the rotational constants, given in Tables 3.1 – 3.4. Due to the very limited number of inertial parameters, we performed a fit limited to the r_0-structure, which neglects the vibrational contributions from the different isotopomers and which is based on the assumption:

$$I_0^g = I_{rigid}^g(r_0) \tag{3.11}$$

where the I_0^g are the (experimentally determined) zero-point averaged moments of inertia with respect to the inertial axes g. The functions $I_{rigid}^g(r_0)$ are calculated from the structural parameters r_0 using rigid-molecule formulas. Thus, no vibrational corrections are introduced in the determination of the structure. Table 3.9 gives the results of the structure fits. As only three rotational constants are available we

Table 3.7: Rotational constants of cis and trans o-cresol from a MP2/6-31G(d,p) calculation for the electronic ground state. The difference of a CIS/6-31G(d,p) and a HF/6-31G(d,p) calculation are compared to the experimentally determined changes of the rotational constants upon excitation. All values are in MHz.

	MP2//6-31G(d,p)	CIS//6-31G(d,p)	CIS-HF//6-31G(d,p)	exp.
		cis-o-cresol		
A''	3 242.2			3 232.91
B''	2 202.6			2 148.84
C''	1 322.4			1 301.66
A'		3 193.1		3 128.31
B'		2 203.7		2 120.44
C'		1 314.5		1 274.94
ΔA			-88.6	-104.61
ΔB			-26.6	-28.40
ΔC			-24.3	-26.71
		trans-o-cresol		
A''	3 293.0			3 168.41
B''	2 190.5			2 173.76
C''	1 326.1			1 299.79
A'		3 168.1		3 021.97
B'		2 223.7		2 168.07
C'		1 317.1		1 273.47
ΔA			-147.7	-146.45
ΔB			-0.2	-5.69
ΔC			-24.8	-26.32

calculated the structure using a very simplified model for the molecules. In order to compare the structural changes upon electronic excitation, this model was chosen the same for all four isomers. All ring CH bonds are set to 108.5 pm for the electronic ground state and to 107.2 pm for the electronically excited state as in phenol. The methyl CH bonds are kept fix at 108.9 pm for both electronic states. The CC bond length of the ring-methyl group bond is kept at 150.6 pm. All dihedral angles are fixed at a planar conformation for both electronic states. The CC bonds between the hydroxy and methyl substituent are set equal and are fit (CC_b). All other ring CC

Table 3.8: Rotational constants of cis and trans *m*-cresol from a MP2/6-31G(d,p) calculation for the electronic ground state. The difference of a CIS/6-31G(d,p) and a HF/6-31G(d,p) calculation are compared to the experimentally determined changes of the rotational constants upon excitation. All values are in MHz.

	MP2//6-31G(d,p)	CIS//6-31G(d,p)	CIS-HF//6-31G(d,p)	exp.
		cis-*m*-cresol		
A''	3 670.3			3 573.14
B''	1 789.5			1 761.84
C''	1 212.0			1 189.10
A'		3 613.5		3 446.88
B'		1 801.4		1 751.87
C'		1 211.0		1 170.52
ΔA			-110.8	-126.26
ΔB			-13.7	-9.97
ΔC			-18.5	-18.58
		trans-*m*-cresol		
A''	3 652.9			3 653.36
B''	1 797.0			1 738.36
C''	1 213.6			1 186.90
A'		3 599.9		3 538.70
B'		1 806.3		1 719.57
C'		1 211.7		1 166.33
ΔA			-111.7	-114.66
ΔB			-11.2	-18.79
ΔC			-17.6	-20.57

bonds are set equal and are fit (CC_a). Additionally, the CO bond is fit. Of course the results of Table 3.9 represent only one possible set of changes, that is valid in the given model.

The structural changes of *cis* and *trans o*- and *m*-cresol upon electronic excitation can be summarized by a shortening of the CO bond length and an overall increase of the ring CC bonds. These findings support the results of the *ab initio* calculations. Comparing the results of the CIS and the HF calculations, one finds a reduction of the CO bond length of 2 pm, independent of the conformer and an increase of the

Table 3.9: Structural changes of *cis* and *trans o-* and *m*-cresol upon electronic excitation from a model structure, described in the text. All values are in pm.

	S_0	S_1	Δ	S_0	S_1	Δ
	cis-*o*-cresol			trans-*o*-cresol		
CC_a	142.6	144.2	+1.6	143.3	143.6	+0.3
CC_b	139.7	144.2	+4.5	137.6	145.1	+7.5
CO	135.6	134.7	-0.9	135.4	134.8	-0.6
	cis-*m*-cresol			trans-*m*-cresol		
CC_a	139.8	143.6	+3.8	143.2	146.6	+3.4
CC_b	140.3	141.4	+1.1	138.2	140.0	+1.8
CO	135.5	134.1	-1.4	135.1	133.0	-2.1

ring bond lengths between 1 and 4 pm.

As can be seen from our results, the torsional constant F_α slightly decreases upon electronic excitation ($\Delta F = -2.5\%$). This is consistent with a small weakening of the σ CH bonds in the methyl top and also supports the $\pi^* - \sigma^*$ HC mechanism [17]. The direction of the methyl top axis in all studied cresols almost bisects the CCC internal angle in the benzene ring (see Fig. 3.1).

Due to the quantum interference effects we were able to determine not only the magnitude, but also the absolute direction of the TM (see Sec. (3.2.2)). In all deuterated cresols θ has the same sign (direction) as η (see Fig. 3.1). The transitions in the hydroxy deuterated *cis* cresols are of almost equal the *a* and *b* types, while in *trans o*-cresol the *a* type lines are stronger ($|\theta| = 37.00°$) and in *trans m*-cresol the *b* type character is more pronounced ($|\theta| = 50.95°$). Fig. 3.8 shows the experimentally determined transition dipole moments for *cis* and *trans ortho*- and *meta*-cresol. The broken arrows indicate the direction of the TM as obtained from the CIS/6-31G(d,p) calculations. In all four cases very close agreement between experiment and theory is obtained. If we compare the orientations of the TM in the cresols with those of the parent molecules toluene and phenol (each in its own inertial system) we find, that the transition dipole moments of all four cresols are oriented close to that of phenol and almost perpendicular to that of toluene. This is quite different from the situation in *m*-aminophenol, studied by Reese *et al.* [41]. There, both substituents, the amino and the hydroxy group, contribute nearly equally to the resulting TM. This was explained by a mixing of the zero-order states ^1L_a and ^1L_b through the unsymmetric substitution. The different behavior of the cresols can be explained by the absence of π-type molecular orbitals at the methyl group. Thus the "toluene" part of the
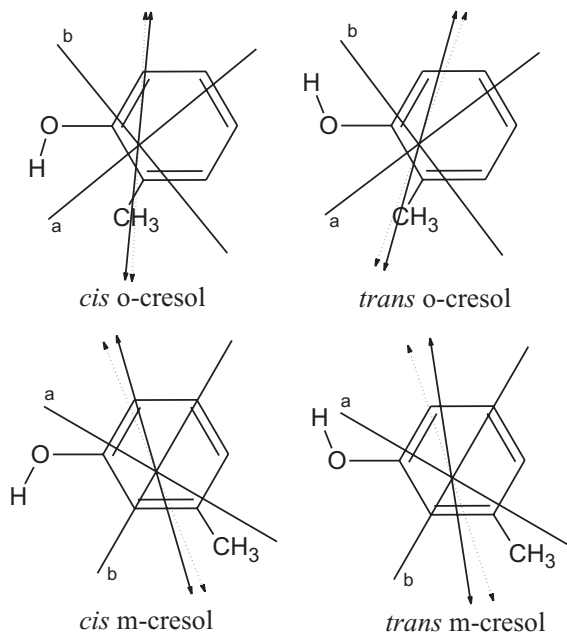
Figure 3.8: Experimental (solid arrows) and calculated (broken arrows) transition dipole moment orientations in *ortho-* and *meta*-cresol. For details of the calculations see text.

molecule has no strong influence on the TM orientation.

The fluorescence lifetime of the hydroxy deuterated cresols is similar to the S_1 state lifetime in hydroxy deuterated phenol ($\tau = 13.3(16)$ ns, Ref. [40]), except for the unusually long lifetime in hydroxy deuterated *trans m*-cresol ($\tau = 26.7(45)$ ns). The first suggests that like in phenol the rapid internal conversion to the -OH stretching vibration is blocked by a deuteration of the hydroxy group. The second is unexpected and it is somewhat similar to the long lifetime encountered in deuterated *cis m*-D, -OD phenol ($\tau = 38.8(70)$ ns, Ref. [40]).

3.6   Summary

We measured and analyzed the rotationally resolved torsional members of the $S_1 \leftarrow S_0$ electronic transition in hydroxy deuterated *o* and *m*-cresols. The spectra could be simulated by treating the internal rotation of the methyl top as a perturbation to the overall rotation of the molecules. For the analysis of the spectra we used the

automated assignments based on genetic algorithms [30, 31], which facilitated the fitting of the complex spectra. The obtained barriers to internal rotation are similar to the ones reported for the undeuterated cresols and the changes in F_α and rotational constants upon electronic excitation seem to indirectly support the hyperconjugation $\pi^* - \sigma^*$ mechanism [17], which is held responsible for the large barrier changes upon the electronic excitation. The derived rotational constants in the both electronic states can be utilized for future validation of the geometry calculations of these molecules.

Other important parameters like the absolute direction of TM and the lifetimes of the hydroxy deuterated o- and m-cresols were determined. In all molecules the angle of the transition dipole moment with the inertial a-axis (θ) has the same sign (direction) as the angle of the methyl torsional axis with the inertial a-axis (η). This implies, that the hydroxy group is the determinating factor for the orientation of the TM, while the influence of the methyl group is small.

The lifetime of these hydroxy deuterated cresols is similar to the lifetime previously reported for hydroxy deuterated phenol [40], with the exception of the hydroxy deuterated *trans* m-cresol, which has a factor two longer lifetime. Therefore explanations of the different lifetimes, which are based on conical intersections along a single (-OH) coordinate [42] have to be refined to account for the observations described in this study.

References

[1] L. Pauling. Note on the interpretation of the infra-red absorption of organic compounds containing hydroxyl and amino groups. *J. Am. Chem. Soc.*, 58:94–98, 1936.

[2] J.D. Kemp and K.S. Pitzer. Hindered rotation of the methyl groups in ethane. *J. Chem. Phys.*, 4:749, 1936.

[3] H. Mizuno, K. Okuyama, T. Ebata, and M. Ito. Rotational isomers of m-cresol and internal rotation of the CH_3 group in S_0, S_1, and the ion. *J. Phys. Chem.*, 91:5589–5593, 1987.

[4] T. Aota, T. Ebata, and M. Ito. Rotational isomers and internal rotation of the CH_3 group in S_0, S_1, and ion of o-cresol. *J. Phys. Chem.*, 93:3519–3522, 1989.

[5] M. Schmitt. *Laserspektroskopie wasserstoffbrückengebundener Cluster im Überschalldüsenstrahl.* PhD thesis, Ruprecht-Karls-Universität, Heidelberg, 1992.

[6] E. Fujimaki, A. Fujii, T. Ebata, and N. Mikami. Autoionization-detected infrared spectroscopy of intramolecular hydrogen bonds in aromatic cations. II.

unconventional intramolecular hydrogen bonds. *J. Chem. Phys.*, 112:137–148, 2000.

[7] K. Suzuki, Y. Emura, Sh. Ishiuchi, and M. Fujii. Internal methyl group rotation in *o*-cresol studied by pulsed field ionization-zeke photoelectron spectroscopy. *J. Electron Spectrosc. Relat. Phenom.*, 108:13–20, 2000.

[8] A. Welzel, A. Hellweg, I. Merke, and W. Stahl. Structural and torsional properties of o-cresol and o-cresol-OD as obtained from microwave spectroscopy and *ab initio* calculations. *J. Mol. Spec.*, 215:58–65, 2002.

[9] K. Okuyama, N. Mikami, and M. Ito. Internal-rotation of the methyl-group in the electronically excited-state – *o*-fluorotoluene, *m*-fluorotoluene, and *p*-fluorotoluene. *J. Phys. Chem.*, 89:5617–5625, 1985.

[10] Z.-Q. Zhao, C.S. Parmenter, D.B. Moss, A.J. Bradley, E.W. Knight, and K.G. Owens. *p*-fluorotoluene. I. methyl CH_3 and CD_3 internal rotation in the S_1 and S_0 states. *J. Chem. Phys.*, 96:6362–6377, 1992.

[11] K. Okuyama, N. Mikami, and M. Ito. Internal-rotation of the methyl-group in the electronically excited-state – *o*-toluidine and *m*-toluidine. *Laser Chem.*, 7:197–212, 1987.

[12] M. Fujii, M. Yamauchi, K. Takazawa, and M. Ito. Electronic-spectra of *o*-tolunitrile, *m*-tolunitrile and *p*-tolunitrile – substituent effect on internal-rotation of the methyl-group. *Spectrochim. Acta, Part A*, 50:1421–1433, 1994.

[13] Warren J. Hehre, John A. Pople, and Alain J. P. Devaquet. Torsional potentials of methyl rotors attached to polar linkages. *J. Am. Chem. Soc.*, 98:664–668, 1976.

[14] K. Lu, F. Weinhold, and J. Weisshaar. Understanding barriers to internal rotation in substituted toluenes and their cations. *J. Chem. Phys.*, 102:6787–6805, 1995.

[15] Y. Sonoda and S. Iwata. Theoretical studies of the internal rotation of the methyl group in *o*-, *m*-, *p*-fluorotoluenes and their cations. *Chem. Phys. Lett.*, 243:176–182, 1995.

[16] H. Nakai and M. Kawai. Nature of the change in the rotational barrier of the methyl group due to $S_0 \rightarrow S_1$ excitation. *Chem. Phys. Lett.*, 307:272–276, 1999.

[17] H. Nakai and M. Kawai. $\pi^* - \sigma^*$ hyperconjugation mechanism on the rotational barrier of the methyl group (I): Substituted toluenes in the ground, excited and aionic states. *J. Chem. Phys.*, 113:2168–2174, 2000.

[18] X. Q. Tan, W. A. Majewski, D. F. Plusquellic, and D. W. Pratt. Methyl group torsional dynamics from rotationally resolved electronic spectra. 1- and 2-methylnaphthalene. *J. Chem. Phys.*, 94:7721–7733, 1991.

[19] G. Berden, W. L. Meerts, M. Schmitt, and K. Kleinermanns. High resolution UV spectroscopy of phenol and the hydrogen bonded phenol-water cluster. *J Chem. Phys.*, 104:972–982, 1996.

[20] M. Schmitt, Ch. Ratzer, Ch. Jacoby, and W.L. Meerts. Structure and barrier to internal rotation of 4-methylstyrene in the S_0- and S_1-state. *J. Mol. Spectr.*, 2005.

[21] K. Remmers, E. Jalviste, I. Mistrik, G. Berden, and W. L. Meerts. Internal rotation effects in the rotationally resolved $S_1(^1L_b) \leftarrow S_0$ origin bands of 3-methylindole and 5-methylindole. *J. Chem. Phys.*, 108:8436–8445, 1998.

[22] D. F. Plusquellic and D. W. Pratt. Exploiting quantum interference effects for the determination of the absolute orientation of an electronic transition moment vector in an isolated molecule. *J. Chem. Phys.*, 97:8970–8976, 1992.

[23] E.W. Gordy and R. L. Cook. *Microwave Molecular Spectra*. John Wiley & Sons, New York, 3rd edition, 1984.

[24] D. R. Herschbach. Calculation of energy levels for internal torsion and over-all rotation. III. *J. Chem. Phys.*, 31:91–108, 1959.

[25] J. T. Hougen, I. Kleiner, and M. Godefroid. Selection rules and intensity calculations for a C_s asymmetric top molecule containing a methyl group internal rotor. *J. Mol. Spec.*, 163:559–586, 1994.

[26] Y. R. Wu and D. H. Levy. Determination of the geometry of deuterated tryptamine by rotationally resolved electronic spectroscopy. *J. Chem. Phys.*, 91:5278–5284, 1989.

[27] J. H. Holland. *Adaption in Natural and Artificial Systems*. MI: The University of Michigan Press, Ann-Arbor, 1975.

[28] D. E. Goldberg. *Genetic Algorithms in search, optimisation and machine learning*. Addison-Wesley, Reading Massachusetts, 1989.

[29] I. Rechenberg. *Evolutionsstrategie - Optimierung technischer Systeme nach Prinzipien der biologischen Evolution*. Frommann-Holzboog, Stuttgart, 1973.

[30] J. A. Hageman, R. Wehrens, R. de Gelder, W. Leo Meerts, and L. M. C. Buydens. Direct determination of molecular constants from rovibronic spectra with genetic algorithms. *J. Chem. Phys.*, 113:7955–7962, 2000.

[31] W. Leo Meerts, M. Schmitt, and G. Groenenboom. New applications of the genetic algorithm for the interpretation of high resolution spectra. *Can. J. Chem.*, 82:804–819, 2004.

[32] M. J. Frisch, G. W. Trucks, H. B. Schlegel, G. E. Scuseria, M. A. Robb, J. R. Cheeseman, V. G. Zakrzewski, J. A. Montgomery, Jr., R. E. Stratmann, J. C. Burant, S. Dapprich, J. M. Millam, A. D. Daniels, K. N. Kudin, M. C. Strain, O. Farkas, J. Tomasi, V. Barone, M. Cossi, R. Cammi, B. Mennucci, C. Pomelli, C. Adamo, S. Clifford, J. Ochterski, G. A. Petersson, P. Y. Ayala, Q. Cui, K. Morokuma, P. Salvador, J. J. Dannenberg, D. K. Malick, A. D. Rabuck, K. Raghavachari, J. B. Foresman, J. Cioslowski, J. V. Ortiz, A. G. Baboul, B. B. Stefanov, G. Liu, A. Liashenko, P. Piskorz, I. Komaromi, R. Gomperts, R. L. Martin, D. J. Fox, T. Keith, M. A. Al-Laham, C. Y. Peng, A. Nanayakkara, M. Challacombe, P. M. W. Gill, B. Johnson, W. Chen, M. W. Wong, J.L. Andres, C. Gonzalez, M. Head-Gordon, E. S. Replogle, and J. A. Pople. Gaussian 98, revision a.11. Gaussian, Inc., Pittsburgh, PA, 2001.

[33] W.A. Kreiner, H.D. Rudolph, and B.T. Tan. Microwave spectra of several molecular isotopes of toluene. *J. Mol. Spectr.*, 48:86–99, 1973.

[34] M. Schmitt, J. Küpper, D. Spangenberg, and A. Westphal. Determination of the structures and barriers to hindered internal rotation of the phenol-methanol cluster in the S_0 and S_1 state. *Chem. Phys.*, 254:349–361, 2000.

[35] R.V. Pound. Electronic stabilization of microwave ocillators. *Rev. Sci. Instrum.*, 17:490–505, 1946.

[36] R.W.P. Drewer and J.L. Hall and F.V. Kowalski and J. Hough and G.M. Ford and A.J. Munley and H. Ward. Laser phase and frequency stabilization using an optical resonator. *Appl. Phys. B*, 31:97–105, 1983.

[37] S. Gerstenkorn and P. Luc. *Atlas du Spectre d'Absorption de la Molécule d'Iode.* CNRS, Paris.

[38] M. Schmitt, Ch. Ratzer, K. Kleinermanns, and W. Leo Meerts. Determination of the structure of 7-azaindole in the electronic ground and excited state using high resolution ultraviolet spectroscopy and an automated assignment based on a genetic algorithm. *Mol. Phys.*, 102:1605–1614, 2004.

[39] M. Schmitt, Ch. Ratzer, and W.L. Meerts. The structure of the phenol-nitrogen cluster: a joint experimental and *ab initio* study. *J. Chem. Phys.*, 120:2752–2758, 2004.

[40] Ch. Ratzer, J. Küpper, D. Spangenberg, and M. Schmitt. The structure of phenol in the S_1-state determined by high resolution UV-spectroscopy. *Chem. Phys.*, 283:153–169, 2002.

[41] Jennifer A. Reese, Tri V. Nguyen, Timothy M. Korter, and David W. Pratt. Charge redistribution on electronic excitation. Dipole moments of *cis*- and *trans*-3-aminophenol in their S_0 and S_1 electronic states. *J. Am. Chem. Soc.*, 126:11387–11392, 2004.

[42] A. L. Sobolewski and W. Domcke. Photoinduced electron and proton transfer in phenol and its clusters with water and ammonia. *J. Phys. Chem.A*, 105:9275–9283, 2001.

The structure of 4-methylphenol and its water cluster revealed by rotationally resolved UV-spectroscopy using a genetic algorithm approach [1]

Abstract

The structure of 4-methylphenol (p-cresol) and its binary water cluster has been elucidated by rotationally resolved laser induced fluorescence spectroscopy. The electronic origins of the monomer and the cluster are split into four subbands by the internal rotation of the methyl group and of the hydroxy group in case of the monomer and the water moiety in case of the cluster. From the rotational constants of the monomer the structure in the S_1-state could be determined to be distorted quinoidally. The structure of the p-cresol-water cluster is determined to be trans-linear, with a O–O hydrogen bond length of 290 pm in the electronic ground state and of 285 pm in the electronically excited state. The S_1-state life time of p-cresol, p-cresol-d_1 and the binary water cluster have been determined to be 1.6 ns, 9.7 ns, and 3.8 ns, respectively.

4.1   Introduction

In this study we present the determination of the geometry of p-cresol and its binary water cluster in the ground state and the electronically excited S_1 state by means of rotationally resolved electronic spectroscopy. The determination of excited state structures of aromatic molecules gives insight into the changes of the electronic

properties of the chromophore. In a series of investigations, we determined the structural changes of some *para* disubstituted aromatic molecules like *p*-fluorophenol [1], *p*-cyanophenol [2] and *p*-methylstyrene [3]. In all these cases a quinoidal distortion along the *a*-axis of the molecule is found, whereas for singly substituted benzenes a symmetric distortion (benzenoid) of the aromatic ring is found [4]. Changes of the electronic properties are also reflected in the change of torsional barriers of symmetric (e.g. CH_3) or asymmetric tops (e.g. OH) which are directly attached to the benzene ring. In recent publications it was shown, how the different electronic properties of the fluorine and the cyano group influence the barrier to hydroxy torsion in both electronic states of *p*-fluorophenol and *p*-cyanophenol [1, 2].

4-methylphenol possesses two feasible large amplitude motions, the methyl rotation with a mixed V_3/V_6 potential, and the twofold hydroxy rotation. The molecular symmetry group, which describes both motions is G_{12}. In the *p*-cresol water cluster, the OH torsion is quenched; instead an additional splitting due to the torsional motion of the water moiety with respect to the water symmetry axis is observed. This barrier is expected from the similar phenol-water system to be quite low. Thus, we have the case of two low barrier torsional motions, which will split the origin into four subbands, an $A^{(3)} - E$ pair due to the threefold motion and an $A^{(2)} - B$ pair due to the twofold rotation. We use the superscripts (2) and (3) to distinguish the different A sublevels from the two and threefold internal rotation from the A rotational constant. Since the rotational constants of this cluster are quite small, the overlapping of four subspectra leads to a very congested overall spectrum, in which it is difficult, if not impossible to identify single rovibronic lines. However, the assignment of well resolved lines to specific quantum numbers of the transitions is an indispensable prerequisite for an assigned fit of the molecular parameters. We have shown recently that in these cases of many overlapping lines the use of a genetic algorithm approach for automated assignment of the spectra simplifies the interpretation and in many cases only makes it possible [5].

4-methylphenol has found considerable interest as chromophore and simple molecular model of the aromatic amino acid tyrosine [6]. Proton transfer, electron transfer and hydrogen transfer are important processes in clusters of tyrosine. E.g. in the water oxidizing complex of photosystem II, tyrosine is oxidized and reduced by hydrogen atom transfer involving tyrosine, water, and histidine in the active center [7].

The electronic ground state of *p*-cresol has been investigated by infrared [8, 9] and Raman spectroscopy [6, 10], by stimulated emission dip spectroscopy [11] and by dispersed fluorescence spectroscopy [12]. Recently Lin *et al.* presented a mass-analyzed threshold ionization spectrum of the *p*-cresol cation [13]. The nature of conformational preferences in *p*-cresol has been studied theoretically by Richardon *et al.* [14]. They determined the most stable conformation of *p*-cresol on MP2 level of theory to be eclipsed with respect to the methyl group orientation, and the OH group on the same side of the aromatic ring as the eclipsed methyl hydrogen (*syn*),
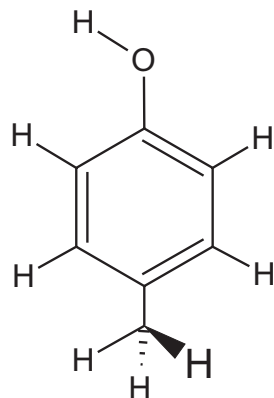
Figure 4.1: Most stable conformation of *p*-cresol.

cf. Fig. 4.1.

Several *p*-cresol-water clusters up to 4 water molecules have been studied using dispersed fluorescence and R2PI spectroscopy in the region of the intermolecular vibrations [15, 16]. From the vibrational analysis it is deduced that the binary cluster is hydrogen bound via a trans-linear H-bond as in the similar phenol-water system [17].

4.2   Experimental setup

The experimental setup for high resolution LIF is described in detail elsewhere [18]. Briefly, the molecular beam machine consists of three differentially pumped vacuum chambers that are linearly connected by two skimmers with orifice diameters of 1 mm (first chamber) and 2 mm (second chamber) for reduction of the Doppler width to 25 MHz. The expansion chamber is evacuated by a 8000 l/s oil diffusion pump (Leybold DI 8000), which is backed by a 250 m^3/h roots blower pump (Saskia RPS 250) and a 65 m^3/h rotary pump (Leybold D65B). The second chamber serves as buffer chamber and is pumped by a 400 l /s turbo-molecular pump (Leybold Turbovac 361), backed by a 40 m^3/h rotary pump (Leybold D40B), maintaining a chamber pressure below $1 \cdot 10^{-5}$ mbar. The third chamber is pumped by a 145 l/s turbo-molecular pump (Leybold Turbovac 151) through a liquid nitrogen trap and backed by a 16 m^3/h rotary pump (Leybold D16B) resulting in a vacuum better than $1 \cdot 10^{-6}$ mbar. The molecular beam is crossed at right angles with the laser beam 360 mm downstream from the nozzle.

The laser system consists of a ring dye laser (Coherent 899-21), which is pumped

with 6 W of the 514 nm line of an Ar^+-ion laser (Coherent Innova 100). This light is coupled into an external folded ring cavity (Spectra Physics) for second harmonic generation (SHG). Typical UV powers are 10 - 40 mW. The laser induced fluorescence is collected perpendicular to the plane defined by laser and molecular beam by an imaging optics setup consisting of a concave mirror and two plano-convex lenses. Data acquisition is performed and synchronized by means of a homebuilt real time Linux program [19].

4.3 Theory of the internal rotation

The coupling between the internal rotation of the methyl group and the overall rotation of the molecule and the coupling of the OH and the water torsion with the overall rotation are treated in the formalism of the principal axis method (PAM) [20, 21]. This is exact in the first (symmetric top) case, but only an approximation for the twofold (asymmetric) top. Nevertheless as the hydrogen atom of the OH group and in the water moiety is light, and the inertial axes remain virtually unchanged during rotation of the top, the application of the PAM leads to reliable results. The Hamiltonian for the rotation-torsion interaction can be written as:

$$H = H_R + H_T + H_{RT} \tag{4.1}$$

with the rigid rotational Hamiltonian given by:

$$H_R = AJ_a^2 + BJ_b^2 + CJ_c^2. \tag{4.2}$$

The torsional Hamiltonian for the mixed V_3/V_6 potential (methyl torsion) is given by:

$$H_T = Fp^2 + \frac{1}{2}\sum_{n=1}^{2} V_{3n}(1 - \cos 3n\alpha), \tag{4.3}$$

and for a twofold V_2 potential (OH and water torsion) by:

$$H_T = Fp^2 + \frac{1}{2}\sum_{n=1}^{2} V_{2n}(1 - \cos 2n\alpha). \tag{4.4}$$

F is the torsional constant and defined by:

$$F = \frac{h}{8\pi^2 r I_\alpha} \tag{4.5}$$

with

$$r = 1 - \sum_{g=a,b,c} \frac{\lambda_g^2 I_\alpha}{I_g} \tag{4.6}$$

here λ_g $(g=a,b,c)$ are the direction cosines between the inertial axes and the axis of internal rotation. I_α is the moment of inertia of the internal rotor with respect to its symmetry axis and the I_g are the principal moments of inertia of the entire molecule. In what follows, the treatment for the $n = 2$ and $n = 3$ potentials is identical.

The coupling of internal and overall rotation is described by H_{RT} [20, 22]:

$$
\begin{aligned}
H_{RT} = {} & FW_{v\sigma}^{(1)}(\rho_a J_a + \rho_b J_b + \rho_c J_c) \\
& + FW_{v\sigma}^{(2)}(\rho_a J_a + \rho_b J_b + \rho_c J_c)^2
\end{aligned}
\tag{4.7}
$$

where the first order perturbation coefficients $W_{v\sigma}^{(1)}$ are zero for the nondegenerate $A^{(2)}$-,$A^{(3)}$ and B-levels. $W_{v\sigma}^{(2)}$ is nonzero for all levels.

The coefficients ρ_g with $g = a, b, c$ are defined as:

$$
\begin{aligned}
\rho_a &= I_\alpha/I_a \cos\eta \\
\rho_b &= I_\alpha/I_b \sin\eta
\end{aligned}
\tag{4.8}
$$

with η as the angle between the projection vector of the n-fold rotor axis on the ab-plane and the a-axis.

The n-th order perturbation coefficients $W_{v\sigma}^{(n)}$ in Eq. (4.7) are defined by [20]:

$$
W_{v\sigma}^{(0)} = \frac{E_{v\sigma}}{F}
\tag{4.9}
$$

$$
W_{v\sigma}^{(1)} = -2\left\langle v,\sigma\right| p \left| v,\sigma\right\rangle
\tag{4.10}
$$

$$
W_{v\sigma}^{(2)} = 1 + 4F\sum_{v'}\frac{\left|\left\langle v,\sigma\right| p \left| v',\sigma\right\rangle\right|^2}{E_{v\sigma} - E_{v'\sigma}}
\tag{4.11}
$$

where $|v,\sigma\rangle$ are eigenfunctions of Eq.'s (4.3) and (4.4), and $E_{v\sigma}$ are the respective eigenvalues with v as the torsional state index.

4.4   The genetic algorithms

The experimental spectra were assigned automatically using a genetic algorithm based fit described in detail in Ref. [5] and [23]. We used the GA library PGAPack version 1.0, which can run on parallel processors [24]. The calculations were performed on eight processors of a SUN UltraSPARC 333 MHz and on a 2.6 GHz PC with two processors under Linux. The genetic algorithm uses concepts copied from natural reproduction and selection processes. For a detailed description of the GA the reader is referred to the original literature on evolutionary or genetic algorithms. [25–27] In the present work a population of 300 was used and the calculation was completely converged after 500 generations. The other parameters which control the genetic algorithm convergency are similar as in Ref. [5].

The cost function used to describe the quality of the fit was defined as $C_{fg} = 100(1 - F_{fg})$ with the fitness function F_{fg}:

$$F_{fg} = \frac{(\boldsymbol{f}, \boldsymbol{g})}{\|\boldsymbol{f}\| \, \|\boldsymbol{g}\|}. \tag{4.12}$$

$\boldsymbol{f}$ and $\boldsymbol{g}$ represent the experimental and calculated spectra, respectively and the inner product $(\boldsymbol{f}, \boldsymbol{g})$ is defined with the metric $\boldsymbol{W}$ which has the matrix elements $W_{ij} = w(|j - i|) = w(r)$ as:

$$(\boldsymbol{f}, \boldsymbol{g}) = \boldsymbol{f}^T \boldsymbol{W} \boldsymbol{g}, \tag{4.13}$$

and the norm of $\boldsymbol{f}$ as $\|\boldsymbol{f}\| = \sqrt{(\boldsymbol{f}, \boldsymbol{f})}$ and similar for $\boldsymbol{g}$. For $w(r)$ we used a triangle function[23] with a width of the base of Δw:

$$w(r) = \begin{cases} 1 - |r| / \left(\frac{1}{2}\Delta w\right) & \text{for } |r| \leqslant \frac{1}{2}\Delta w \\ 0 & \text{otherwise.} \end{cases} \tag{4.14}$$

Since the GA performs an intensity fit of the complete spectrum, much better information on the transition dipole moment (TDM) orientation and line width parameters is gathered than from an intensity fit to a few individual lines. Thus, the GA results in improved values for the in plane angle θ of the TDM and also of the Lorentzian width of the individual rovibronic lines. Therefore excited state life times can be determined with a much higher accuracy than in line shape fits of individual rovibronic lines.

4.5   Results and Discussion

4.5.1   4-methylphenol

Fig. 4.2 shows the rotationally resolved LIF spectrum of the electronic origin of p-cresol. The spectrum is split into two components, $A^{(3)}$ and E by the internal rotation of the methyl group ($E_{v,0} - E_{v,\pm 1}$). Their respective origins, which are 8218 MHz apart, are marked by arrows.

In two recent publications [3, 28] we showed how a combined fit to high resolution rovibronic data and low resolution torsional transitions can be used to improve the determination of the barriers and torsional constants in both electronic states. A, B, C, V_3, V_6, F, and η were fit for each electronic state to the rotationally resolved origin and to the torsional transitions from Ref. [29]. These torsional transitions are obtained from the zero order perturbation coefficient, cf. Eq. (4.9). The rovibronic spectrum was fit using the genetic algorithm (GA) approach, described in Ref. [5]. The parameters that determine the intensity and line-form are the rotational temperatures, the Lorentzian and Gaussian linewidths and the projections of the transition dipole moment to the inertial axes. They can be fit most favorably using the GA algorithm.

Figure 4.2: (a) Experimental and fitted rovibronic spectrum of the electronic origin of 4-methylphenol. (b) 10 GHz zoom in of the (a) spectrum. (c) Inset showing three pairs of rovibronic transitions split by the two-fold hydroxy group rotation in cresol. For the sake of clarity only the strongest transitions are shown and the splitting is marked with the horizontal lines. The solid line represents experiment and the dashed line the fit. All frequencies are given relative to the electronic origin at 35331.257(10) cm^{-1}.

The Lorentzian contribution to the linewidth of the Voigt profile with a fixed Doppler width of 25 MHz is determined to be 100$\pm$10 MHz, equivalent to a S_1-state lifetime of 1.6$\pm$0.2 ns. The results of the fits are compiled in Tables 4.1 and 4.2.

Closer inspection of the spectrum shows that each of the rovibronic transitions is further split into two close lying subbands (cf. Fig. 4.2c) due to the hindered -OH torsion. As a twofold torsion leads only to nondegenerate $A^{(2)}$-($\sigma = 0$) and B-($\sigma = 1$) levels, the first order perturbation coefficients from Eq. (4.10) are zero. The second order perturbation coefficients which are nonzero (Eq. 4.11) are quadratic in the angular momentum and can therefore be incorporated in the rotational constants.

Table 4.1: Molecular parameters of 4-methylphenol and 4-methyl[7D]phenol from the GA fit. The ground state rotational constants of 4-methylphenol have been kept fixed at the microwave values from Ref.[30].

4-methylphenol		S_0	S_1
A	(MHz)	5494.570	5154.6(12)
B	(MHz)	1456.963	1470.51(67)
C	(MHz)	1160.200	1153.62(41)
V_3	(MHz)	18.00(25)	7.99(34)
V_6	(MHz)	-13.8(45)	-24.7(43)
F	(cm^{-1})	5.224(98)	5.108(98)
ν_0	(cm^{-1})	35331.257(10)	
$\nu_0(E) - \nu_0(A^{(3)}) =$	(MHz)	8218(16)	
$\nu_0(A^{(2)}) - \nu_0(B) =$	(MHz)	90(13)	
4-methyl[7D]phenol			
A	(MHz)	5442.16(94)	5110.04(94)
B	(MHz)	1417.59(37)	1431.03(37)
C	(MHz)	1133.45(27)	1127.46(27)
V_3	(MHz)	18.00(25)	7.99(34)
V_6	(MHz)	-13.8(45)	-24.7(43)
F	(cm^{-1})	5.170(7)	5.066(7)
ν_0	(cm^{-1})	35326.729(10)	
$\nu_0(E) - \nu_0(A^{(3)}) =$	(MHz)	8656.2(50)	

Since the OH torsional barrier is very high, the perturbations are small and both subbands can be fit with the same set of effective rotational constants and a origin shift between the $A^{(2)}$- and B-bands of 90 MHz.

Determination of barriers and torsional constants in both electronic states demands more information from other spectroscopic techniques. In the microwave spectrum a splitting of the b-type transitions of 175 MHz has been observed [30]. The selection rule for b-type transitions is $\Delta\sigma = \pm 1$, so that the splitting between the sub-torsional levels amounts to 87.5 MHz. The frequency of the pure torsional transition has been determined by IR spectroscopy to be 294 cm^{-1} [9]. The first overtone of the torsional vibration in the electronically excited state is determined to be 1199

Table 4.2: Torsional transitions of 4-methylphenol. The electronic transitions are labeled by the m quantum number and the symmetry of the sub-torsional level σ: $m\sigma(S_1) \leftarrow m\sigma(S_0)$ for absorption bands and $m\sigma(S_1) \rightarrow m\sigma(S_0)$ for emission bands.

p-cresol	exp.	fit.	diff.	
$1e \leftarrow 1e$	8218(16)	8214	-4	MHz
$2e \leftarrow 1e$	15.1(5)	15.4	+0.3	cm^{-1}
$3a_1 \leftarrow 0a_1$	51.7(5)	52.7	+1.0	cm^{-1}
$4e \leftarrow 1e$	77(2)	77.9	+0.9	cm^{-1}
$5e \leftarrow 1e$	125(2)	123.6	-1.4	cm^{-1}
$1e \rightarrow 2e$	18.5(10)	17.7	-0.8	cm^{-1}
$0a_1 \rightarrow 3a_1$	52.5(10)	51.9	-0.6	cm^{-1}
$1e \rightarrow 4e$	80.0(20)	80.1	+0.1	cm^{-1}

cm^{-1}. Using these transitions and fixing the torsional constant F at 690 GHz (the value in phenol), we are able to fit the ground state torsional V_2-barrier to 1130 cm^{-1} and the excited state barrier to 4395 cm^{-1}. Both values are slightly lower than the corresponding values in phenol (1215 and 4710 cm^{-1}, respectively) [17].

4.5.2 4-methyl[7-D]phenol

Fig. 4.3 shows the rotationally resolved LIF spectrum of the electronic origin of 4-methyl[7-D]phenol. Due to the heavier OD group, the twofold torsion is quenched in this system and the molecular symmetry group for the description of the molecule is G_6. Consequently, the origin band consists only of split pair of $A^{(3)}$- and E-bands with a frequency spacing of 8656 MHz.

Table 4.1 gives the molecular parameters that have been determined using the GA program. The lifetime for 4-methyl[7-D]phenol is determined to be 9.7±0.6 ns from a Lorentzian contribution to the total linewidth of 16.4±1 MHz. The $A^{(3)}E$ sub-torsional splitting is very similar to the splitting in 4-methylphenol, also indicating similar potential barriers. As no torsional bands of 4-methyl[7-D]phenol have been measured not enough data are available to fit the barriers to methyl rotation in this molecule. Nevertheless, since the effect of hydroxy deuteration on the methyl barrier is supposed to be small, we set barriers and torsional constants equal to those of

Figure 4.3: Rovibronic spectrum of the electronic origin of 4-methyl[7D]phenol. Frequencies are given relative to the electronic origin at $35326.729(10)$ cm^{-1}.

4-methylphenol.

4.5.3 4-methylphenol(H$_2$O)$_1$

Fig. 4.4 presents the rotationally resolved electronic spectrum of the origin of the p-cresol-water cluster at 34972.873 cm^{-1}. The origin is split into an $A^{(3)}$ and an E subband due to the methyl torsion with a subtorsional splitting of 5459 MHz and into an $A^{(2)}$ and B subband due to the water torsion with a subtorsional splitting of 29428 MHz.

As in the case of phenol, the sub-torsional structure due to the twofold water torsion can be fit using a rigid rotor model with different rotational constants for both components. Similar to the phenol-water case, the B and C rotational constants of the ($\sigma = 0$) and ($\sigma = 1$) components are equal within their uncertainties. The A constants of the sub-torsional components differ by about 11 MHz indicating, that

Figure 4.4: Rovibronic spectrum of the electronic origin of 4-methylphenol-water. Frequencies are given relative to the electronic origin at $34972.873(10)$ cm^{-1}.

the torsional axis of the water torsion is more or less parallel to the main inertial a-axis of the cluster. This structure can be described as a trans-linear hydrogen bond configuration, with the water moiety acting as proton acceptor, like in phenol-water. A spin statistics of 1:3 for the ratio of ($\sigma = 0$) to ($\sigma = 1$) further supports a structure with the water moiety symmetric with respect to the aromatic plane.

This analysis clearly shows the convenience of the GA analysis of such a complex spectrum. Although by eye no periodicity can be observed at first glance, the GA is capable of easily finding the two splittings from the methyl torsion (5459 MHz) and the water torsion (29428 MHz). Of course, the application of the GA based automated technique still requires the choice of the 'correct' Hamiltonian for the problem under consideration. An easy way of finding spectral splittings (and thus obtaining information about the required Hamiltonian) is to perform an autocorrelation of the spectrum. This method has been shown by Neusser's group to be helpful in the analysis of the phenol-water cluster spectrum [31] and later by Remmers *et al.* in the

Table 4.3: Molecular parameters of 4-methylphenol-water

	S_0		S_1	
	$\sigma = 0$	$\sigma = 1$	$\sigma = 0$	$\sigma = 1$
A (MHz)	3663.48(244)	3652.19(53)	3590.87(244)	3576.37(53)
B (MHz)	765.60(59)	765.98(31)	774.78(59)	774.35(31)
C (MHz)	637.00(48)	637.71(31)	640.76(48)	641.61(31)
V_3 (cm^{-1})	18.00(25)		7.99(34)	
V_6 (cm^{-1})	-13.8(45)		-24.7(43)	
F (cm^{-1})	5.41(7)		5.21(7)	
ν_0 (cm^{-1})			34971.891(10)	34972.873(10)
$\nu_0(A^{(2)}) - \nu_0(B)$ (MHz)		29428(7)		
$\nu_0(A^{(3)}) - \nu_0(E)$ (MHz)		5459(6)		

analysis of the tunneling spectrum of the benzoic acid dimer [32]. Nevertheless, if one component of the complete spectrum amount to more than 50 % of the total intensity, the GA is capable of fitting this part of the spectrum, although it might be concealed in the dense spectrum of the other component(s) and would therefore be in accessible to a classical analysis using line position assigned fits. From the difference of the partly fitted spectrum to the experimental one the missing components can easily be recognized and subsequently fit.

In order to compute the geometrical rotational constants from the torsionally perturbed constants of Table 4.3, we have to estimate the V_2 potential energy barrier and the torsional constant F for the water torsion in both electronic states. However, only three pieces of information are available for the determination of these four parameters: The $(\sigma = 0)/(\sigma = 1)$ sub-torsional splitting of 29428 MHz, the difference of the A rotational constants for $(\sigma = 0)$ and $(\sigma = 1)$ in the electronic ground state and in the electronically excited state. Fixing F'' of the ground state to the value determined for phenol-water (14.813 cm^{-1}) [28] (the ground state acidities of phenol and cresol are similar, therefore one would expect similar torsional constants for the water moiety) a ground state barrier V_2'' of 182.6 cm^{-1}, an excited state barrier V_2' of 125.3 cm^{-1} and a torsional constant F' in the excited state of 14.9 cm^{-1} are calculated. These values are very close to the torsional barriers of phenol-water.

Table 4.4: Structural r_0-parameters of p-cresol. For atomic numbering see Fig. 4.1.

	S_0	S_1	
$B_1(C_1C_2)$	139.9(1)	142.2(10)	(pm)
$B_2(C_2C_3)$	140.5(3)	138.1(10)	(pm)
$B_3(C_3C_4)$	138.9(1)	144.3(4)	(pm)
$B_4(CO)$	138.3(6)	134.5(11)	(pm)
$B_5(CC_{methyl})$	151.3(6)	150.3(2)	(pm)

4.5.4 Determination of the structures

The program *pKrFit* [4] was used to determine the structure of 4-methylphenol in the S_0 and S_1-states from the rotational constants of the two isotopomers described above. Due to the limited number of isotopomers in this study, we performed a fit to the r_0-structure, which completely neglects the vibrational contributions from the different isotopomers. A simple model for the geometry has been adopted, that is given in Fig. 4.1. All aromatic CH bonds are set to the same value (107.7 pm for the ground state and 107.4 pm for the excited state), the CH bonds of the methyl group are fixed at 109.0 pm. The OH bond lengths from the structural fits of phenol have been taken as constants (96 pm in the S_0 and 99 pm in the S_1-state). Opposing CC bonds are set equal.

Table 4.4 gives the results for the fits of the S_0 and the S_1 structure. The aromatic ring expands upon electronic excitation quinoidally, as has been found for other *para* disubstituted aromatic compounds. The CO and the CC_{methyl} bond lengths decrease, what is in agreement with a quinoidal distortion of the ring system. The relative shortening of these bands cannot be determined accurately, as both bonds nearly coincide with the main inertial a-axis. Because the deuteration is at a position close to this axis, both bond lengths are strongly correlated. The results present therefore only one possible combination of bond length decreases.

From the above determined S_0 and S_1-structures of the cresol moiety, we fitted the structure of the p-cresol-water to the geometric rotational constants. All geometry parameters in p-cresol have been kept fixed at the monomer values, the geometry of the water moiety has also been kept fixed. We imposed the symmetry constraint on the fit: The H-atoms of the water moiety are symmetric with respect to the aromatic plane. Table 4.5 shows the results.

The O–O hydrogen bond length decreases by 5.0 pm upon electronic excitation, imaging the increased acidity of p-cresol upon electronic excitation, while the OOC

Table 4.5: Structural r_0-parameters of p-cresol-water. The atomic numbering refers to Fig. 4.1, the subscript w refers to atoms of the water moiety. The dihedral angle is defined between the H_1-atom of the water moiety, the O-atom of water, the O_7-atom of cresol and the C_1-atom of cresol. The second dihedral angle is determined by the symmetry constraint.

	S_0	S_1	
$r(O_w O_7)$	290.0(2)	285.0(2)	(pm)
$a(O_w O_7 C_1)$	114.4(12)	113.9(20)	(deg)
$a(H_{w1} O_w O_7 C_1)$	120(47)	116(16)	(deg)
$a(H_{w2} O_w O_7 C_1)$	-120(47)	-116(16)	(deg)

Table 4.6: OH-torsional barriers of phenol, p-fluorophenol, p-cyanophenol and p-methylphenol (p-cresol). All values in cm^{-1}.

	$V_2(S_0)$	$V_2(S_1)$	References
p-fluorophenol	1006	1819	[1]
p-methylphenol	1130	4395	[this work]
phenol	1215	4710	[17]
p-cyanophenol	1420	>5000	[2]

angle and the HOOC dihedral, describing the orientation of the water moiety nearly stay constant. Two different views of the ground state structure are shown in Fig. 4.5.

4.6   Conclusions

The value for the torsional barrier due to the internal rotation of the hydroxy group in p-cresol was found to be 1130 cm^{-1} in the ground state, and 4395 cm^{-1} in the excited state. These values can be compared to the V_2 barriers of other p-disubstituted phenols and of phenol itself, given in Table 4.6.

Relative to phenol, *para* substitution with fluorine (+mesomeric effect) and methyl (+inductive effect) leads to a decrease of the torsional barrier in both electronic states,
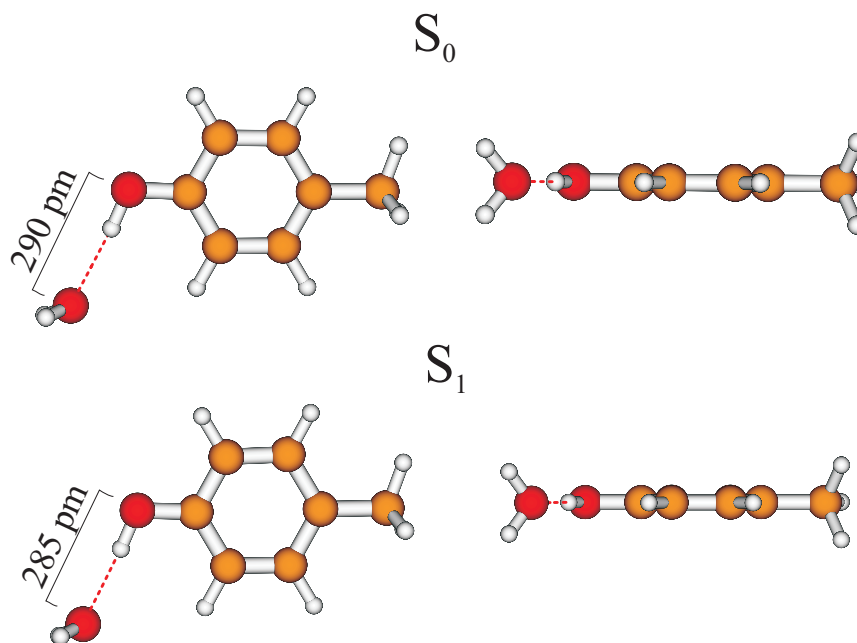
Figure 4.5: Top and side views of the ground and excited state structures of p-cresol-water. For all other geometry parameters see Table 4.5.

while the cyano group (-mesomeric effect) increases the barrier. Electron accepting groups (as cyano) stabilize a partial quinoidal structure of the p-substituted phenol with some double bond character of the CO bond, while electron donating groups destabilize it. The lifetime of 4-methyl[7-D]phenol determined from the Lorentz contribution to the Voigt profile (9.7 ns) is substantially longer than the respective 4-methylphenol life time of 1.6 ns. A similar increase of the S_1 state life time was found for phenol and [7D]phenol and was explained by a smaller probability for tunneling of the OD species through the barrier which separates the $^1\pi\sigma^*$ from the $^1\pi\pi^*$ surface [33].

The V_3 and V_6 barriers of the methyl group torsion are low , as is typical for molecules with G_{12} symmetry. Barriers determined from 4-methylphenol and 4-methyl[7-D]phenol are equal within the uncertainty, showing that the two torsional motions are mainly decoupled.

From the rotational constants of both isotopomers, the structural change upon electronic excitation could be determined. As it is typical for *para* disubstituted aromatics, the ring expands quinoidally upon excitation, while the two bonds in *para*

position decrease. The decrease of the CO bond length mirrors the shift of electron density from the oxygen atom to the aromatic ring, which takes place and is the reason for the increased acidity of phenols upon electronic excitation.

The rotationally resolved electronic spectrum of the origin of the water cluster is split into an $A^{(3)}E$ pair due to the methyl group rotation and into an $A^{(2)}B$ pair due to the torsional motion of the water moiety. The S_1 lifetime of the p-cresol-water cluster determined from the Lorentz contribution to the Voigt profile is 42 ± 5 MHz, equivalent to a S_1-state lifetime of 3.8 ± 0.5 ns, which is much shorter than the life time of the similar phenol-water cluster (15 ns). The large increase of the lifetime by going from phenol to the phenol-water cluster was attributed by Sobolewski and Domcke to a removal of the conical intersection of the $^1\pi\sigma^*$ surface with the ground state. Furthermore, the $^1\pi\sigma^*$ surface shifts to higher energies, and develops a minimum at the hydrogen transfered geometry of the cluster [33]. The longer lifetimes of deuterated phenol and the phenol-water cluster compared to phenol have therefore different explanations (smaller tunneling rate vs. removal of a conical intersection). For the explanation of the life times, it was also discussed, that a rapid internal conversion takes place with the OH stretching vibration as accepting mode [34, 35]. Both deuteration and complexation with water lower the stretching frequency of the OH vibration, reducing its ability to act as accepting mode. In this picture the lifetime of the p-cresol-water cluster should be equally increased as the one of deuterated p-cresol. However, we found a much shorter lifetime for the cresol-water cluster than for the deuterated cresol, strongly favoring the lifetime model of Sobolewski and Domcke [33].

The structure of the p-cresol-water cluster could be determined to be trans-linearly hydrogen bound, with cresol as proton donor like in the similar phenol-water cluster. The O–O hydrogen bond length could be determined to be 290 pm in the ground state and to 285 pm in the electronically excited state. This decrease in hydrogen bond length is a consequence of the increased acidity of p-cresol in the S_1-state, which leads to a stronger hydrogen bond. Again, the decrease of the hydrogen bond length of 5 pm is very similar to the corresponding value in phenol-water (4 pm).

References

[1] Ch. Ratzer, M. Nispel, and M. Schmitt. Structure of p-fluorophenol and barrier to internal -OH torsion in the S_1-state. *Phys. Chem. Chem. Phys.*, 5:812–819, 2002.

[2] J. Küpper, M. Schmitt, and K. Kleinermanns. The rotationally resolved electronic spectrum of p-cyanophenol. *Phys. Chem. Chem. Phys.*, 4:4634–4639, 2002.

[3] M. Schmitt, Ch. Ratzer, Ch. Jacoby, and W. L. Meerts. Structure and barrier

to internal rotation of 4-methylstyrene in the S_0- and S_1-state. *J. Mol. Struct.*, 742:123–130, 2005.

[4] Ch. Ratzer, J. Küpper, D. Spangenberg, and M. Schmitt. The structure of phenol in the S_1-state determined by high resolution UV-spectroscopy. *Chem. Phys.*, 283:153–169, 2002.

[5] W. Leo Meerts, M. Schmitt, and G. Groenenboom. New applications of the genetic algorithm for the interpretation of high resolution spectra. *Can. J. Chem.*, 82:804–819, 2004.

[6] Z. Arp, D. Autrey, J. Laane, S. A. Overman, and G. J. Thomas. Tyrosine raman signatures of the filamentous virus ff are diagnostic of non-hydrogen-bonded phenoxyls: Demonstration by raman and infrared spectroscopy of p-cresol vapor. *Biochemistry*, 40:2522–2529, 2001.

[7] M. R. A. Blomberg and P. E. M. Siegbahn. A quantum chemical study of tyrosyl reduction and O–O bond formation in photosystem II. *Mol. Phys.*, 101:323–333, 2001.

[8] G. Varsanyi. *Assignments for Vibrational Spectra of 700 Benzene Derivatives.* Wiley, New York, 1974.

[9] R. J. Jacobsen. *Spectrochim. Acta*, 21:433–441, 1965.

[10] J. Laane, K. Haller, S. Sakurai, K. Morris, D. Autrey, Z. Arp, W. Y. Chiang, and A. Combs. Raman spectroscopy of vapors at elevated temperatures. *J. Mol. Struct.*, 650:57–68, 2003.

[11] T. Ebata and M. Ito. Ground-state IVR of jet-cooled p-alkylphenols and p-alkylanilines studied by stimulated emission ion dip and stimulated Raman-UV optical double-resonance spectroscopies. *J. Phys. Chem.*, 96:3224–3231, 1992.

[12] K. Song and J. M. Hayes. Supersonic jet spectra of p-alkylphenols. *J. Mol. Spec.*, 134:82–97, 1989.

[13] J. L. Lin, C. Li, and W. B. Tzeng. Mass-analyzed threshold ionization spectroscopy of p-methylphenol and p-ethylphenol cations and the alkyl substitution effect. *J. Chem. Phys.*, 120:10513–10519, 2004.

[14] P. R. Richardson, M. A. Chapman, D. C. Wilson, S. P.Bates, and A. C. Jones. The nature of conformational preference in a number of p-alkyl phenols and p-alkyl benzenes. *J. Chem. Phys.*, 4:4910–4915, 2002.

[15] M. Pohl, M. Schmitt, K. Wolf, and K. Kleinermanns. Microscopic shifts of size assigned p-cresol$(H_2O)_n$-cluster spectra. *J. Chem. Phys.*, 94:1717, 1991.

[16] M. Pohl, M. Schmitt, and K. Kleinermanns. Vibrational spectroscopy of size-assigned p-cresol/H_2O-clusters in the S_0 and S_1 state. *Chem. Phys. Letters*, 177:252, 1991.

[17] Giel Berden, W. Leo Meerts, M. Schmitt, and Karl Kleinermanns. High resolution UV spectroscopy of phenol and the hydrogen bonded phenol-water cluster. *J. Chem. Phys.*, 104:972–982, 1996.

[18] M. Schmitt, J. Küpper, D. Spangenberg, and A. Westphal. Determination of the structures and barriers to hindered internal rotation of the phenol-methanol cluster in the S_0 and S_1 state. *Chem. Phys.*, 254:349–361, 2000.

[19] J. Küpper. *Rotationsauflösende Laserspektroskopie - Beziehung zwischen Struktur und interner Dynamik von Molekülen.* PhD thesis, Heinrich-Heine-Universität, Math. Nat. Fakultät, Düsseldorf, 2000.

[20] W. Gordy and R. L. Cook. *Microwave Molecular Spectra.* Wiley, New York, 3 edition, 1984.

[21] C. C. Lin and J. D. Swalen. Internal rotation and microwave spectroscopy. *Rev. Mod. Phys.*, 31:841–891, 1959.

[22] D. R. Herschbach. Calculation of energy levels for internal torsion and over-all rotation. III. *J. Chem. Phys.*, 31:91–108, 1959.

[23] J. A. Hageman, R. Wehrens, R. de Gelder, W. Leo Meerts, and L. M. C. Buydens. Direct determination of molecular constants from rovibronic spectra with genetic algorithms. *J. Chem. Phys.*, 113:7955–7962, 2000.

[24] D. Levine. PGAPack V1.0, PgaPack can be obtained via anonymous ftp from: ftp://ftp.mcs.anl.gov/pub/pgapack/pgapack.tar.z.

[25] J. H. Holland. *Adaption in Natural and Artificial Systems.* MI: The University of Michigan Press, Ann-Arbor, 1975.

[26] D. E. Goldberg. *Genetic Algorithms in search, optimisation and machine learning.* Addison-Wesley, Reading Massachusetts, 1989.

[27] I. Rechenberg. *Evolutionsstrategie - Optimierung technischer Systeme nach Prinzipien der biologischen Evolution.* Frommann-Holzboog, Stuttgart, 1973.

[28] Ch. Jacoby and M. Schmitt. Torsional barriers in aromatic molecular clusters as probe of the electronic properties of the chromophore. *Chem. Phys. Chem.*, 5:1686–1694, 2004.

[29] M. Schmitt. *Laserspektroskopie wasserstoffbrückengebundener Cluster im Überschalldüsenstrahl*. PhD thesis, Ruprecht-Karl-Universität, Heidelberg, 1992.

[30] Armin Hellweg. *Mikrowellenspektroskopische Untersuchungen zur intramolekularen Dynamik von p-Toluidin, p-Kresol und p-Thiokresol*. Gnter Mainz, 2003.

[31] R. M. Helm, H. P. Vogel, and H. J. Neusser. Rotational analysis and tunnel splittings of the intermolecular vibrations of the phenol-water complex by high resolution UV spectroscopy. *J. Chem. Phys.*, 108:4496–4504, 1998.

[32] K. Remmers, W. Leo Meerts, and I. Ozier. Proton tunneling in the benzoic acid dimer studied by high reolution UV spectroscopy. *J. Chem. Phys.*, 112:10890–10894, 2000.

[33] A. L. Sobolewski and W. Domcke. Photoinduced electron and proton transfer in phenol and its clusters with water and ammonia. *J. Phys. Chem.A*, 105:9275–9283, 2001.

[34] A. Sur and Ph. M. Johnson. Radiationless transitions in gas phase phenol and the effects of hydrogen bonding. *J. Chem. Phys.*, 84:1206, 1986.

[35] R. J. Lipert and S. D. Colson. Deuterium isotope effects on S_1 radiationless decay in phenol and on intermolecular vibrations in the phenol-water complex. *J. Phys. Chem.*, 93:135, 1989.

Structure determination of resorcinol rotamers by high resolution UV spectroscopy [1]

Abstract

The rotationally resolved $S_1 \leftarrow S_0$ electronic origins of several deuterated resorcinol rotamers cooled in a molecular beam were recorded. An automated assignment of the observed spectra was performed using a genetic algorithm approach with an asymmetric rotor Hamiltonian. The structures of resorcinol A and resorcinol B were derived from the rotational constants of twenty deuterated species for both electronic states. The lifetimes of different resorcinol isotopomers in the S_1 state are also reported. Like in phenol these lifetimes mainly depend on the position of deuteration. A nearly perfect additivity of the zero-point energies after successive deuterations in resorcinol rotamers was discovered and subsequently used in the full assignment of the previously reported low resolution spectra of deuterated resorcinol A [1].

5.1 Introduction

The three dihydroxybenzenes catechol (1,2-dihydroxybenzene), resorcinol (1,3-dihydroxybenzene), and hydroquinone (1,4-dihydroxybenzene) are building blocks of many biologically important groups of molecules, like flavanones, flavones, flavonols, and anthocyanins. As such their structure is essential in understanding the chemistry and dynamics of these biomolecules. Another interesting topic is that hydroquinone possesses two isomers, which are distinguished by the relative orientation of their two
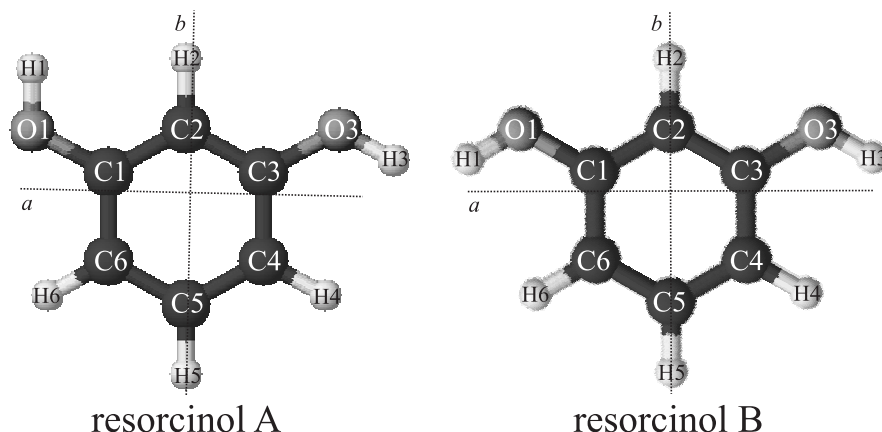
Figure 5.1: Rotamers of resorcinol studied in the paper. Numbering of the atoms is used in the text to refer to the different deuterated species. Inertial axes a and b are also shown, the c is perpendicular to the ab plane.

-OH groups (*cis – trans* isomerism). For resorcinol and catechol even three such rotamers are expected, although for catechol one of these three will have a strong steric hindrance. It is therefore not a surprise that dihydroxybenzenes have been a topic of many scientific publications.

Low resolution spectra (for example laser induced fluorescence – LIF, resonance enhanced multiphoton ionization – REMPI or dispersed fluorescence – DF) help to understand the vibrational activity in different electronic states of the molecules. REMPI spectra of dihydroxybenzenes up to about 300 cm^{-1} were recorded by Dunn *et al.* [2] and different rotamers were tentatively assigned. However, as shown by Gerhards *et al.* [3] earlier assignments of resorcinol rotamers were incorrect. Using spectral hole burning Gerhards *et al.* observed two series of transitions arising from two different rotamers of resorcinol and attributed the band at 35944 cm^{-1} to the $S_1 \leftarrow S_0$ origin of structure A and the band at 36196 cm^{-1} to the $S_1 \leftarrow S_0$ origin of structure B (see Fig. 5.1). Later, low resolution studies on resorcinol, its cations and deuterated isotopomers combined experimental and theoretical approaches [1, 4, 5] yielded a better understanding of the structure and vibrations in the S_0, S_1 and D_0 electronic states.

Microwave (MW) spectroscopy of *cis* hydroquinone [6] allowed for determination of the -COH groups structure in its electronic ground state. MW spectra of resorcinol [7] yielded the rotational constants of the ground state of all three possible rotamers. Unfortunately, no isotopic substitutions were done and consequently no structural parameters were derived. On the other hand rotational constants pre-

dicted from theoretical structures of resorcinol [1, 3] do not compare very well with the microwave data [7]. This indicates that higher level calculations are needed.

Since MW spectroscopy gives only rotational constants of the electronic ground state, high resolution laser induced fluorescence spectroscopy has to be applied to obtain information about the electronically excited states. The structure of the S_1 state of phenol was derived from high resolution LIF data of several isotopomers [8]. The *trans* and *cis* rotamers of hydroquinone were identified in the high resolution $S_1 \leftarrow S_0$ fluorescence excitation experiments by Humphrey and Pratt [9]. They determined the structural change of hydroquinone upon electronic excitation and deduced a quinoidal structure in the electronic S_1 state.

In the present work we determine the *pseudo r_s*-structures [10] of the A and B rotamers of resorcinol in their S_0 and S_1 electronic states (see Fig. 5.1). A total of 24 $S_1 \leftarrow S_0$ electronic origins of deuterated species of resorcinol A and B were measured using rotationally resolved LIF. We fit the obtained spectra with a genetic algorithms (GA) automated assignment [11, 12] to an asymmetric rotor Hamiltonian. The GA prove to be very useful in analysis of the multitude of spectra acquired in this experiment. All spectra can be described within experimental accuracy as *a*-type spectra. Similarly to phenol [8], the S_1 lifetimes of the deuterated molecules depend mainly on the position of deuteration. We also show extreme additivity of the zero-point energies after successive deuterations in resorcinol rotamers. Finally, we use this fact to correct the assignment of the low resolution spectra of deuterated resorcinol A [1].

5.2   Experiment

5.2.1   Apparatus

The experimental setup for the rotationally resolved LIF is described elsewhere [13]. In short, the vacuum system consists of three differentially pumped vacuum chambers that are linearly connected by two skimmers (1 mm and 2 mm). The skimmers collimate the molecular beam and hence reduce the Doppler contribution to the measured linewidth to 25 MHz of full width at half-maximum (FWHM).

The laser part consists of single frequency ring dye laser (Coherent 899-21), pumped with 7 W of the 514 nm line of an argon-ion laser. Rhodamine 110 is used in the dye laser as a lasing medium. The fundamental light from the dye laser is coupled into an external delta cavity (Spectra Physics) for second harmonic generation (SHG). The UV radiation at $\sim$ 278 nm is generated in this cavity by an angle tuned, brewster cut BBO crystal. The cavity length is locked to the dye laser frequency by a frequency modulation technique [14, 15]. Typically $\sim$ 20 mW of UV radiation is available for the experiment.

The UV laser crosses the molecular beam 360 mm downstream from the nozzle
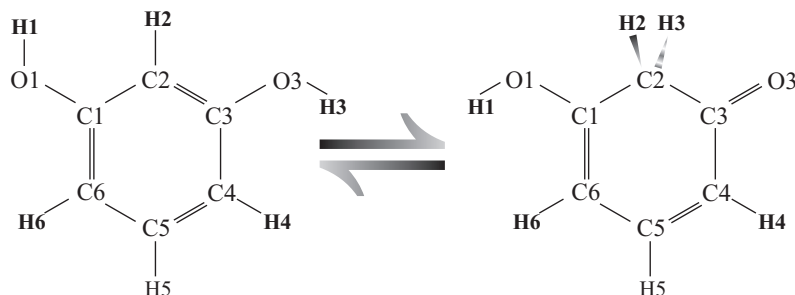
Figure 5.2: Keto-enol tautomerism in resorcinol A rotamer. Due to this mechanism the hydrogen atoms shown in bold are easily deuterated.

under right angles. The molecular fluorescence is collected perpendicular to the plane defined by the laser and molecular beam by an imaging optics. The total fluorescence is detected by a photomultiplier tube, whose output is digitized by a photon-counter and send to a PC for data acquisition and processing. The relative frequency is determined with a quasi-confocal Fabry-Perot interferometer with a free spectral range of 149.9434(56) MHz. For the absolute frequency calibration an iodine spectrum is recorded and compared with the tabulated data [16].

Commercially available undeuterated resorcinol is used without further purification. To substitute different hydrogen atoms from resorcinol with deuterium atoms, it is mixed with a surplus of D_2O in the source container. Firstly, the hydroxy groups are deuterated. Subsequently, all hydrogen atoms except H5 can be exchanged by deuterium atoms due to a keto-enol tautomerism (see Fig. 5.2). To increase the vapour pressure of resorcinol, the source is heated to 180 °C. Subsequently, the molecular beam is formed by expanding a mixture from the source, seeded in 600 mbar of argon, through a 100 μm hole into the vacuum system.

5.2.2   Spectra of deuterated species

First we tried to obtain the rotationally resolved LIF spectra of the $S_1 \leftarrow S_0$ origins of the undeuterated resorcinol A and B. Although we searched for the spectra within ± 10 cm^{-1} from the origins given by Ref. [3] we failed to detect any signal. This must be due to a very short lifetime of the S_1 electronic state of resorcinol, which is apparently much shorter then the one of phenol [8] and hydroquinone [9].

We therefore based our experiments on the deuterated species using the assignment of the mass resolved R2PI spectra of deuterated resorcinol A reported in Ref. [1]. Since we expected short lifetimes (*i.e.* possibly weak or undetectable spectra) for all hydroxy undeuterated resorcinol isotopomers we focused on the bands originating
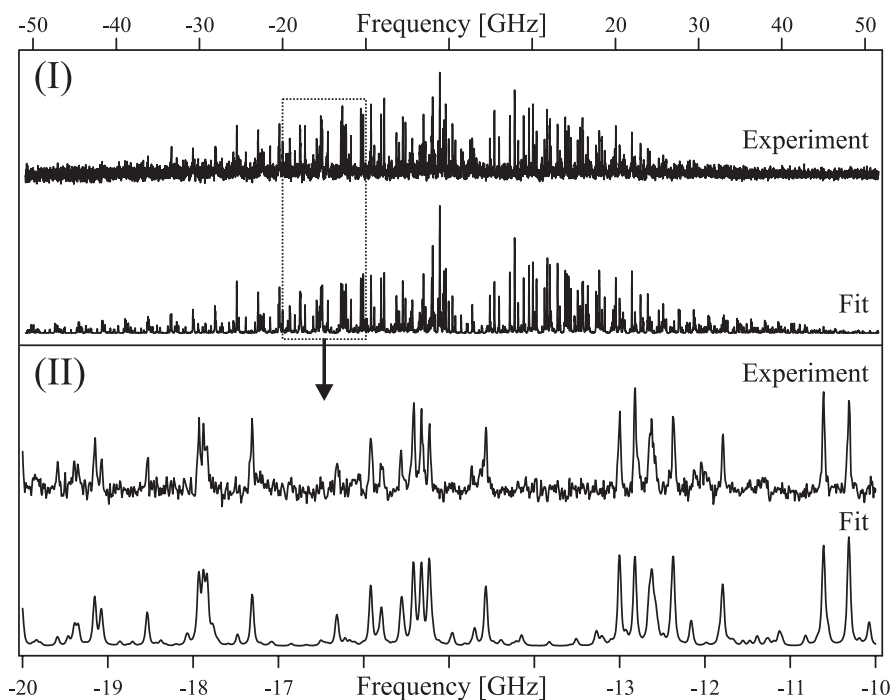
Figure 5.3: Experimental and fitted spectra of (1,3,4,6) and (1,4,6) deuterated re-sorcinol A. (I) Full spectra. (II) 10 GHz zoom in. The zero in the frequency scale corresponds to the origin of (1,3,4,6) transition, ν_0 of (1,4,6) species is shifted from the other band by +3661(7) MHz.

from isotopomers with at least one hydroxy group deuterated. The results will be presented in the following section.

The numbering of the atoms used further in the text is presented in Fig. 5.1. For designation of different deuterated species we put the numbers of hydrogens replaced by deuterium in brackets, if necessary separated by commas. For example, (1,3) means resorcinol isotopomer with deuterium atoms in positions H1 and H3.

5.3   Results and discussion

5.3.1   Analysis of the spectra

All spectra were analyzed with a rigid asymmetric rotor Hamiltonian [17] with a two-temperature model [18]. For the fitting of spectra we used an automatic assignment GA program, developed in our group [11, 12]. This GA based approach confirmed its usefulness in the assignment of many (24), frequently overlapping spectra present in our study.

In general, the spectra of resorcinol A were found to be weaker than the ones of B. At first sight this is surprising, because the low resolution LIF spectra from Ref. [5] show a slightly weaker signal for rotamer B than for A. *Ab initio* calculations [3, 19] also confirm a lower stability of rotamer B. However, it has been found from our analysis that in general the isotopomers of resorcinol A have shorter lifetimes and thus might indeed have weaker rotationally resolved spectra, due to lifetime broadening. This will be discussed in Section 5.3.6.

Within the experimental accuracy all the bands analyzed in this work were found to be pure *a*-type transitions. The -OH torsional splittings remained unresolved for all hydroxy undeuterated resorcinol isotopomers. A sample of the spectra and the GA fit of the $+65.60$ cm^{-1} band of resorcinol A is presented in Fig. 5.3. The spectrum of three overlapping bands at around $+75$ cm^{-1} originating from the three different isotopomers of rotamer B is compared with the GA fit in Fig. 5.4. GA fits of the other spectra of resorcinol A and B are of similar quality. In the two-temperature model [18] implemented in the GA fits typical values for the rotational temperatures were following $T_1 \sim 1.8$ K, $T_2 \approx 3 - 8$ K and for the weighting factor $w \approx 0.04 - 0.1$.

5.3.2   Spin statistics

Rotamer A of resorcinol belongs to the molecular symmetry (MS) group isomorphic with point group C_s. Consequently, we do not expect any influence of the nuclear spin statistics on the rotational spectra of any of its isotopomers. This is in agreement with the experimental finding.

On the other hand rotamer B can be characterized by the MS group C_{2v}. Therefore the ratio of the line intensities for $K_a + K_c = odd$ to the $K_a + K_c = even$ should be 6:10. This is characteristic for the molecules with C_{2v} symmetry with two pairs of equivalent hydrogens, where C_2 axis coincides with the b inertial axis. However, for most isotopomers of this resorcinol rotamer, the C_{2v} symmetry is lost and hence the spin statistics does not influence the rotational spectra any more. The only isotopomers, which will still possess the C_{2v} symmetry are the ones symmetrically substituted with respect to the inertial b axis, namely (1,3), (4,6), (1,2,3), (2,4,6), (1,3,4,6) and (1,2,3,4,6) (position 5 cannot be deuterated in our experiment). The first four species contain a pair of equivalent hydrogens, as well as a pair of equivalent
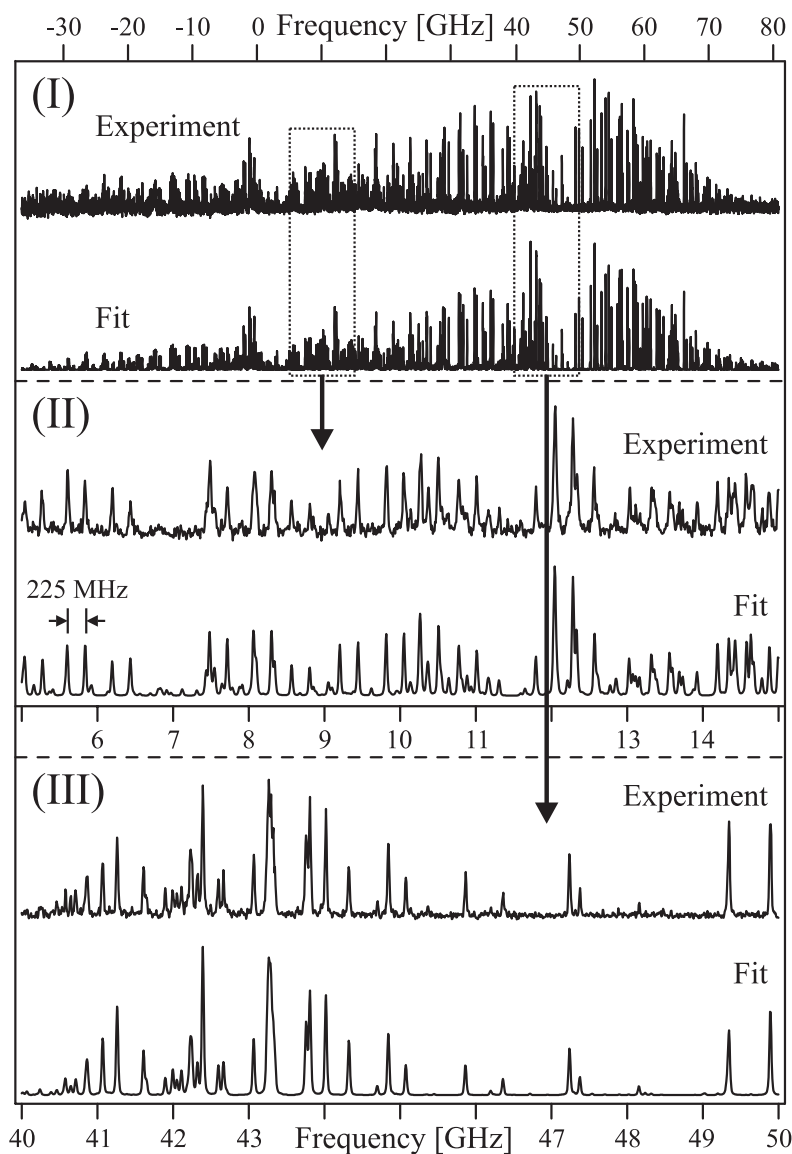
Figure 5.4: Experimental and fitted spectra of (1,2,4),(1,2,6) and (1,2,3,4) deuterated resorcinol B. (I) Full spectra. The zero in the frequency scale corresponds to the origin of the (1,2,4) isotopomer. (II) 10 GHz zoom in of the part belonging to the (1,2,4) and (1,2,6) isotopomers. A small splitting of 225 MHz between these two bands is also shown. (III) 10 GHz zoom in of the origin vicinity of the (1,2,3,4) species.

deuterium atoms. In this case the line intensities for $K_a + K_c = odd$ to $K_a + K_c = even$ is 7:5. For the (1,3,4,6) and (1,2,3,4,6) sotopomers two pairs of equivalent deuterium atoms give an intensity ratio $K_a + K_c = odd$ to $K_a + K_c = even$ equal 4:5.

5.3.3 Molecular constants

The rotational constants of resorcinol A and B, together with the other parameters obtained from the GA fits of the 20 experimental spectra are given in Tables 5.1 and 5.2, respectively. Parameters presented in these tables were averaged over typically five different GA fits of the same spectrum started from different initial parameter values. Due to the weak spectra of bands (2,3,4), (2,4), (2,3,6) and (2,6) of resorcinol A, ten runs of GA fits were averaged in these cases. Simulated spectra with averaged parameters as well as the ones from the single fits always gave a perfect or very good match with the observed spectra both in intensity and positions of the transitions.

Averaging also gives an estimate of the errors of the fitted parameters using standard deviations of the averages. Subsequently, we derived a final uncertainty (containing correlations between the parameters) utilizing a least-square program [20] with the line positions calculated from the averaged GA results. In these calculations we manually included only lines with the large enough intensity, $i.e$ the lines which would be used in the 'classical' assignment. The upper limit for the errors of the absolute origin ν_0 and $\Delta\nu_0$ was estimated from the absolute frequency calibration to the iodine lines [16]. It amounts 0.010 cm^{-1}.

All analyzed bands were attributed to isotopomers based on the structure fit to the inertial parameters and their shifts from undeuterated species. Details are discussed in the following sections. We also note here that the spectra of the (1) and (1,3) isotopomers of resorcinol A, and the (4) and (4,6) isotopomers of resorcinol B were too weak for reliable GA fits. However, after successful structure fits these spectra could be reproduced with rotational constants derived from the calculated structural parameters.

5.3.4 Structure fit

Models

From the experiment we obtained the rotational constants B_g^0, which are related to the vibrationally averaged moments of inertia of the molecule I_g^0 via

$$I_g^0 = \hbar/4\pi B_g^0, \tag{5.1}$$

with g designating principal axes of inertia of the molecule a, b, c. However if possible, one prefers to determine the equilibrium structure of the molecule, which is directly related to the minimum of the potential energy of the electronic state. These latter structures are marked with the superscript e.

Table 5.1: Molecular constants of deuterated resorcinol A. $\Delta\nu_0 = \nu_0 - 35944\ \mathrm{cm}^{-1}$. For spectra where pasting of overlapping scans was possible the $\Delta\nu_0^{prev}$ represents the shift from previous column (isotopomer) origin.

Substitution	(1,3,6)	(1,6)	(1,3,4)	(1,4)
A''/MHz	3591.1(49)	3605(12)	3594.2(66)	3608.8(90)
B''/MHz	1711.08(40)	1770.8(11)	1709.56(51)	1765.96(61)
C''/MHz	1159.01(27)	1185.47(70)	1158.75(42)	1185.06(49)
ν_0/cm^{-1}	35978.745(10)	35978.836(10)	35980.395(10)	35980.513(10)
$\Delta\nu_0/\mathrm{cm}^{-1}$	34.745(10)	34.836(10)	36.395(10)	36.513(10)
$\Delta\nu_0^{prev}/\mathrm{MHz}$		2741.5(64)	46717.6(42)	3550.2(51)
A'/MHz	3463.9(49)	3478(12)	3467.8(66)	3481.4(90)
B'/MHz	1702.62(40)	1761.2(11)	1701.00(51)	1756.50(61)
C'/MHz	1142.25(27)	1167.83(70)	1142.03(42)	1167.52(49)
τ/ns	6.8(15)	3.6(4)	5.5(9)	4.0(6)
Substitution	(1,3,4,6)	(1,4,6)	(2,3,6)	(2,6)
A''/MHz	3520.9(61)	3524.5(80)	3573.8(84)	3574(11)
B''/MHz	1683.00(50)	1739.41(76)	1739.61(73)	1800.4(10)
C''/MHz	1139.14(33)	1164.98(45)	1170.19(50)	1197.63(68)
ν_0/cm^{-1}	36009.596(10)	36009.718(10)	36024.826(10)	36024.910(10)
$\Delta\nu_0/\mathrm{cm}^{-1}$	65.596(10)	65.718(10)	80.826(10)	80.910(10)
$\Delta\nu_0^{prev}/\mathrm{MHz}$		3660.7(53)		2531.0(81)
A'/MHz	3400.3(61)	3402.8(80)	3441.4(84)	3441(11)
B'/MHz	1674.28(50)	1730.03(76)	1730.75(73)	1791.0(10)
C'/MHz	1122.94(33)	1147.90(45)	1152.41(50)	1178.75(68)
τ/ns	7.1(16)	2.3(3)	3.0(3)	2.7(2)
Substitution	(2,3,4)	(2,4)		
A''/MHz	3569(10)	3566(16)		
B''/MHz	1741.93(85)	1800.2(14)		
C''/MHz	1170.29(57)	1197.51(94)		
ν_0/cm^{-1}	36026.557(10)	36026.670(10)		
$\Delta\nu_0/\mathrm{cm}^{-1}$	82.557(10)	82.670(10)		
$\Delta\nu_0^{prev}/\mathrm{MHz}$	49374.7(74)	3379.9(93)		
A'/MHz	3438(10)	3433(16)		
B'/MHz	1733.06(85)	1790.7(14)		
C'/MHz	1152.52(57)	1178.76(94)		
τ/ns	3.8(4)	2.5(3)		

Table 5.2: Molecular constants of deuterated resorcinol B. $\Delta\nu_0 = \nu_0 - 36196 \text{ cm}^{-1}$. For spectra where pasting of overlapping scans was possible the $\Delta\nu_0^{prev}$ represents the shift from previous column (isotopomer) origin.

Substitution	(1,4)	(1,6)	(1,3,4)	(1,2)
A''/MHz	3670(12)	3678(11)	3672.3(57)	3632.4(75)
B''/MHz	1742.50(83)	1744.94(84)	1687.59(42)	1773.01(63)
C''/MHz	1183.30(61)	1183.77(55)	1156.53(30)	1192.14(43)
ν_0/cm^{-1}	36227.801(10)	36227.809(10)	36229.237(10)	36237.829(10)
$\Delta\nu_0$/cm^{-1}	31.801(10)	31.809(10)	33.237(10)	41.829(10)
$\Delta\nu_0^{prev}$/MHz		242.8(65)	42832.9(47)	
A'/MHz	3543(12)	3551(11)	3546.7(57)	3501.7(75)
B'/MHz	1726.93(83)	1728.89(84)	1672.62(42)	1756.86(63)
C'/MHz	1163.30(61)	1163.76(55)	1137.42(30)	1171.23(43)
τ/ns	4.7(9)	4.6(10)	13.2(22)	5.1(8)
Substitution	(1,2,3)	(1,4,6)	(1,3,4,6)	(1,2,4)
A''/MHz	3630.9(58)	3605.9(59)	3597.1(46)	3571.8(57)
B''/MHz	1714.87(47)	1716.49(47)	1661.59(34)	1743.01(47)
C''/MHz	1164.84(30)	1163.20(32)	1137.32(25)	1171.14(32)
ν_0/cm^{-1}	36239.322(10)	36260.428(10)	36261.845(10)	36270.382(10)
$\Delta\nu_0$/cm^{-1}	43.322(10)	64.428(10)	65.845(10)	74.382(10)
$\Delta\nu_0^{prev}$/MHz	44752.8(44)		42476.4(38)	
A'/MHz	3500.9(58)	3485.3(59)	3477.3(46)	3446.6(57)
B'/MHz	1699.73(47)	1700.54(47)	1646.60(34)	1727.00(47)
C'/MHz	1144.87(30)	1143.72(32)	1118.73(25)	1150.75(32)
τ/ns	11.2(16)	5.6(10)	9.4(17)	6.5(13)
Substitution	(1,2,6)	(1,2,3,4)		
A''/MHz	3570.4(54)	3559.2(44)		
B''/MHz	1745.37(46)	1687.43(32)		
C''/MHz	1171.34(32)	1145.25(24)		
ν_0/cm^{-1}	36270.389(10)	36271.864(10)		
$\Delta\nu_0$/cm^{-1}	74.389(10)	75.864(10)		
$\Delta\nu_0^{prev}$/MHz	224.6(42)	44209.3(36)		
A'/MHz	3445.8(54)	3435.1(44)		
B'/MHz	1728.90(46)	1672.30(32)		
C'/MHz	1151.09(32)	1125.82(24)		
τ/ns	6.6(14)	15.1(29)		

There are a few methods to correct the experimental moments of inertia for the vibrational effects. As crudest approximation, one can neglect these effects and force the relation $I_g^0 = I_g^e(r_0)$. The result is called r_0-structure. However, these structures give typically overestimated bond lengths [21] and depend strongly on the choice of isotopomers [22]. In the r_s-structures [22, 23] the following relation is used to take into account average vibrational effects along every principal axes:

$$I_g^0 = I_g^e(r_s) + \frac{1}{2}\epsilon_{0g}. \qquad (5.2)$$

Unfortunately, the substitution method generally does not allow to use multisub-stituted isotopomers in the fit of the structure (with the exception of some highly symmetric multisubstitutions), but it gives better estimates of the hypothetical equilibrium structure and is largely independent of the studied isotopic substitutions.

The third way to include the vibrational corrections is the *pseudo Kraitchman* approach [10]. Here, Eq. 5.2 is utilized in a global, nonlinear fit of all the isotopomers (also multisubstituted) in order to obtain the *pseudo r_s*-structure. We used this model in our structure fits, because it allows to include the vibrational effects on the structure with only three additional parameters (the three ϵ_{0g}), while simultaneously multisubstitutions can be considered. The fitting program utilized has been described in detail in Ref. [8]. More models for the determination of structures from rotational constants have been discussed [24–27], but they are not used here, since they require additional parameters to be fit.

Structural constrains

Since we studied only a limited number of isotopically substituted resorcinols, we had to impose constraints on the geometry of the molecules in the structure fit. Both rotamers of resorcinol in the ground and excited states are treated as planar molecules. This is certainly a good assumption for the ground states, for which MW on resorcinol [7] predict very small inertial defects $\Delta I(A) = -0.083$ and $\Delta I(B) = -0.081$. We do not report the inertial defects for the electronically excited states of the resorcinol rotamers, because of the large uncertainty in A. However, in phenol [8] as well as in hydroquinone [9], the S_1 state was found to be planar and there should be no reason for resorcinol to behave differently.

In the case of resorcinol B the following restrictions are justified by the symmetry: distance C_1–C_2 is set equal to C_2–C_3, C_1–C_6 equals C_3–C_4 and similarly C_4–C_5 equals C_5–C_6. Both -COH groups are equivalent and the inner angles of the benzene ring are set equal in the following pairs: C_6–C_1–C_2 with C_2–C_3–C_4 and C_1–C_6–C_5 with C_3–C_4–C_5. Additionally, we fix the outer C–C–H angles such that C–H bonds bisect the inner C–C–C angles. Finally, all C–H bonds are treated to be identical and the sum of all the inner angles in the benzene ring is fixed to 720 degrees.

In principle, resorcinol A does not have the C_{2v} symmetry of resorcinol B. However, in our structure fits we found that the aforementioned constraints are also valid for resorcinol A. For example, if the distance C_1–C_2 is uncoupled from C_2–C_3, identical values within their uncertainties were found. The same holds for the other C–C pairs mentioned in the previous paragraph as well as for the inner C–C–C angles. For resorcinol A we also fix the two, in principle different -COH groups to the same geometry. This is justified by the fact that the hydroxy groups are in *meta* positions and therefore their electronic and steric interactions are small. The other constraints imposed on the resorcinol B geometry were also applied in the final fit of resorcinol A structure.

Fit

We started the structure fits with resorcinol A, since we expected some help with the assignment of different isotopomers from the low resolution R2PI spectra [1]. As starting parameters we used the bond lengths and -COH group geometry from phenol [8] and additionally fixed the inner benzene ring angles and outer C–C–H angles to 120 degrees. In this way the initial guess of the rotational constants of all possible deuterated isotopomers of resorcinol A was made. These preliminary rotational constants agreed reasonably well with the MW constants [7] obtained for the undeuterated resorcinol. Furthermore, from the guess we could unambiguously assign most of the isotopomers and include them in the fit. The remaining bands were assigned from the improved structural parameters. Only in the case of pairs (2,3,4) with (2,3,6) and (2,4) with (2,6) the differences in the rotational constants were too small for definitive assignment. These bands were tentatively distinguished using their shifts from undeuterated species. For details see Section 5.3.5.

Fitting of some of the parameters from our model made the fit numerically unstable. This was most likely caused by the large uncertainties in the rotational constants, in particular A, but might also be caused by the low number of measured isotopically substituted species. Therefore, in the next step we tried to fix different combinations of geometrical parameters to the values found in phenol [8]. However for consistency reasons, after the successful resorcinol B structure fit we repeated the structure fit of rotamer A with parameters fixed to values found for resorcinol B. The final structural parameters for resorcinol A are presented in Table 5.3.

In contrast to rotamer A, the fit of resorcinol B geometry was straightforward. With the parameters from the species A fit a very good estimate of the rotational constants of all the rotamer B isotopomers was obtained. All the resorcinol B bands shown in Table 5.2 were unambiguously identified. The results of structure fits for both electronic states are presented in Table 5.3.

The structure fits for both resorcinol rotamers in S_0 and S_1 electronic states reproduce the rotational constants of all isotopomers very well. The uncertainties of parameters from Table 5.3 include parameter correlations. It is important to notice

Table 5.3: *Pseudo-r_s* structural parameters of resorcinol A and B in the S_0 and S_1 electronic states. All bond lengths are given in Å and the angles in degrees.

Parameter	A		B	
	S_0	S_1	S_0	S_1
C_2–C_3	1.388(28)	1.450(18)	1.3944(27)	1.438(18)
C_3–C_4	1.388(32)	1.418(21)	1.3963(44)	1.425(28)
C_4–C_5	1.408(29)	1.469(16)	1.4071(77)	1.449(23)
C–H	1.091(27)	$1.074^{a)}$	1.0856(57)	1.074(18)
C–O	1.371(64)	1.307(37)	1.3569(56)	1.3286(92)
O–H	0.959(48)	0.975(34)	0.9547(85)	0.947(57)
C_1–C_2–C_3	$119.68^{a)}$	$116.1^{a)}$	119.68(52)	116.1(14)
C_2–C_3–C_4	$120.68^{a)}$	$122.61^{a)}$	120.68(29)	122.61(69)
C_3–C_4–C_5	$119.41^{a)}$	$120.46^{a)}$	119.41(36)	120.46(73)
C_4–C_5–C_6	$120.14^{a)}$	$117.8^{a)}$	120.14(54)	117.8(13)
C_3–C_2–H_2	$120.16^{a)}$	$121.97^{a)}$	120.16(26)	121.97(71)
C_5–C_4–H_4	$120.29^{a)}$	$119.77^{a)}$	120.29(18)	119.77(37)
C_6–C_5–H_5	$119.93^{a)}$	$121.11^{a)}$	119.93(27)	121.11(64)
C_4–C_3–O_3	119.6(20)	118.7(18)	122.18(54)	121.0(16)
C–O–H	$108.55^{a)}$	$110.0^{a)}$	108.55(21)	110.0(30)
ϵ_A	0.0548(21)	0.180(83)	0.05370(94)	0.220(61)
ϵ_B	0.0552(19)	0.180(83)	0.05396(94)	0.217(61)
ϵ_C	−0.0557(10)	−0.180(83)	−0.05393(94)	−0.217(61)

[a] Fixed in the final fit to the value found for resorcinol B.

that the fitting program is a local optimizer. To exclude convergence to local solutions the fits were repeated with different starting parameters.

Ground and excited electronic state structures

From Table 5.3 it is evident that within the given uncertainties both resorcinol rotamers are structurally very similar. This also holds for the excited electronic states. The aromatic ring of resorcinol expands upon electronic excitation rather equally in all directions (benzenoidal), though there seems to be a trend for elongating the whole

molecule more along the b inertial axis than a-axis.

The most significant differences between resorcinol and phenol [8] are observed for the C–C bond lengths of the benzene frame. For resorcinol the longest bond seems to be the C_4–C_5 bond which is far from the hydroxy groups and the shortest, the bond between the two hydroxy groups C_2–C_3. In contrast, in phenol the largest one is the C_{-OH}–C_{ortho} distance (1.4187(139) Å), closest to the -OH group and the smallest distance (1.3912(34) Å) is the 'middle' one (C_{ortho}–C_{meta}). This can be explained by some collective electronic influence of the hydroxy groups on the benzene skeleton in the *ortho* and *para* positions.

Resorcinol is a slightly stronger acid than phenol [28] ($pK_a^{(resorcinol)} = 9.45$ *vs.* $pK_a^{(phenol)} = 9.96$) in the S_0 electronic state. This seems to be confirmed by the -COH group structures for both molecules. Although the C–O bonds are equal, the O–H bond of the resorcinol tends to be longer than the corresponding one in phenol [8]. Upon electronic excitation we clearly see the shortening of the C–O bonds and a possible elongation of the O–H bonds. This suggests a similar increase of acidity upon the electronic excitation in resorcinol, compared to phenol.

Finally, we can compare the ϵ_g parameters, which represent the averaged effect of vibrations along the g inertial axis. From Table 5.3 it is clear that on average both rotamers experience similar vibrational motions in the ground electronic state. This is not surprising in the light of dispersed fluorescence experiments of Imhof *et al.* [5] on resorcinol A and B, which reported very similar vibrational frequencies for both rotamers. Upon electronic excitation a significant increase of the vibrational activity (ϵ_g) is noticed. This is caused by a shallowing of the potential energy surface for most of the normal modes in the S_1 state and consequently a decrease of the corresponding vibrational frequencies. Again this is in agreement with the reported vibrational frequencies for both resorcinols in the S_1 state [5].

5.3.5   The zero-point energies

Additivity and assignment of electronic shifts

In the Born-Oppenheimer approximation all isotopomers of the same resorcinol rotamer share the same potential energy surface. Within this approximation the differences between shifts of the band origins from the undeuterated origin $\Delta\nu_0$ can be identified with the differences in the zero-point energies between ground and excited states $\Delta ZPE = ZPE' - ZPE''$ for different isotopomers. Moreover, one can easily calculate the ΔZPE's corresponding to subsequent substitutions of all the atoms in the molecule. In our case only H atoms are substituted. The results for resorcinol A and B are presented in Table 5.4.

We start with the discussion of resorcinol B, in which the assignment of isotopomers was more straightforward. It is clear from Table 5.4 that for resorcinol B the ΔZPE's after successive deuterations are extremely additive (to within below

Table 5.4: Differences in the ΔZPE for the observed isotopomers of resorcinol A and B (ΔZPE $\equiv \Delta\nu_0$). Each column named with '+($\dots$)' contains ΔZPE after additional substitution of the isotopomer given in the first column. All numbers are in cm^{-1}.

A	$\Delta\nu_0$	+(3)	+(4)	+(6)	+(3,4)	+(3,6)	+(4,6)	
(1,3) [a]	5.54		30.86	29.21			60.06	
(1) [a]	5.63	−0.09	30.89	29.21	30.77	29.12	60.09	
(1,3,6)	34.74		30.85					
(1,6)	34.84	−0.09	30.88		30.76			
(1,3,4)	36.39			29.20				
(1,4)	36.51	−0.12		29.21		29.08		
(1,3,4,6)	65.60							
(1,4,6)	65.72	−0.12						
(2,3,6)	80.83							
(2,6)	80.91	−0.08						
(2,3,4)	82.56							
(2,4)	82.67	−0.11						

B	$\Delta\nu_0$	+(2)	+(3)	+(4)	+(6)	+(1,3)	+(2,3)	+(3,4)	+(3,6)
(4) [a]	30.39				32.64	2.84			
(1,4)	31.80	42.58	1.44		32.63		44.06		
(1,6)	31.81	42.58		32.62				34.04	34.04
(1,3,4)	33.24	42.63			32.61				
(1,2)	41.83		1.49	32.55	32.56			34.03	
(1,2,3)	43.32			32.54					
(4,6) [a]	63.03					2.81			
(1,4,6)	64.43		1.42						
(1,3,4,6)	65.84								
(1,2,4)	74.38		1.48						
(1,2,6)	74.39								
(1,2,3,4)	75.86								

[a] Origins found for isotopomers with too weak spectra for reliable GA fits. Later fitted with rotational constants predicted from the structure fits.

0.1 cm^{-1}). This additivity of ΔZPE's is not completely surprising, since it was already observed for example for phenol [8]. It clearly points to a very local character of CH and OH stretching and COH bending vibrations in resorcinol B.

For resorcinol A we consider first the upper eight rows of Table 5.4. These data represent the ΔZPE's of isotopomers unambiguously assigned by the structure fits. With high confidence it can be assumed that the substitutions in positions (1), (2) and (3) will also be additive. This assumption is based on the observations that both in resorcinol B and in phenol the ΔZPE's add up very well. Furthermore, the substitutions at positions (4) and (6) (next to any of the two hydroxy groups) in resorcinol A seems to be perfectly additive as well.

From these facts it can be concluded that of the four possible assignments of the isotopomers (2,3,6), (2,3,4),(2,6), and (2,4) only the one presented in Table 5.4 gives additive shifts for substitutions in positions (2) and (3). For the other three possibilities, the ΔZPE after deuteration of either H_2 or H_3 differ within each column by ~ 3.47 cm^{-1}. We do not observe such a large deviations even in phenol. Moreover, in phenol [8] the ΔZPE clearly gets smaller in deuterated isotopomers from -CH groups with increasing distance from the hydroxy group. This agrees perfectly with a smaller origin shift for the $+(6)$ column (*trans* position with respect to -OH group) compared to the $+(4)$ column (*cis* position with respect to -OH group).

Prediction of $S_1 \leftarrow S_0$ spectrum for deuterated resorcinol rotamers.

Based on the additivity of the origin shifts with subsequent deuterations and the average shifts from Table 5.4 we can predict the full $S_1 \leftarrow S_0$ spectrum of deuterated resorcinol A and B. The results are presented in Table 5.5, where they are also compared with the results of the low resolution experiment from Ref. [1]. Clearly for the rotamer A, derived origin shifts $\Delta\nu_0^{pred.}$ are in perfect agreement with the observed ones $\Delta\nu_0^{measured}$. Furthermore, after taking into account FWHM ~ 3 cm^{-1} of the low resolution study, estimated on the basis of Fig. 5 from Ref. [1], we conclude a very good agreement between frequencies. However, in view of our study some of the bands from Ref. [1] had to be reassigned.

For resorcinol B the electronic origin of the undeuterated species that was not observerd in the present investigation, can be determined using the nearly perfect additivity of the ZPE shifts. The values given in Table 5.4 were used for determination of $\nu_0^{undeuterated}$. The resulting average value of $36193.78(4)$ cm^{-1} gives a perfect agreement (to within below 0.1 cm^{-1}) of the predicted and measured origin shifts of all isotopomers. This origin of the undeuterated resorcinol B, is certainly within the experimental error of the low resolution experiments, which reported previously the origin at 36196 cm^{-1} [1].

Table 5.5: Comparison of predicted electronic shifts from undeuterated origin for all resorcinol A isotopomers, deuterated in positions $1 - 6$ (excluding 5), with experimentally observed values $\Delta\nu_0^{measured}$. All numbers are given in cm^{-1}.

	Substitution	$\Delta\nu_0^{pred.}$	$\Delta\nu_0^{measured}$
d1	(3)	−0.10	
	(1)	5.64	5.63
	(6)	29.21	
	(4)	30.87	
	(2)	51.76	
d2	(1,3)	5.53	5.54
	(3,6)	29.10	
	(3,4)	30.77	
	(1,6)	34.84	34.84
	(1,4)	36.50	36.51
	(2,3)	51.65	
	(1,2)	57.39	
	(4,6)	60.07	
	(2,6)	80.96	80.91
	(2,4)	82.62	82.67
d3	(1,3,6)	34.74	34.74
	(1,3,4)	36.40	36.39
	(1,2,3)	57.29	
	(3,4,6)	59.97	
	(1,4,6)	65.71	
	(2,3,6)	80.86	80.83
	(2,3,4)	82.52	82.56
	(1,2,6)	86.60	
	(1,2,4)	88.26	
	(2,4,6)	111.83	
d4	(1,3,4,6)	65.61	65.60
	(1,2,3,6)	86.49	
	(1,2,3,4)	88.16	
	(2,3,4,6)	111.73	
	(1,2,4,6)	117.47	
d5	(1,2,3,4,6)	117.36	

5.3.6 S_1 electronic state lifetimes

For both resorcinol rotamers the trend of increasing the excited state lifetimes with subsequent deuterations of the hydroxy groups is similar (cf. Tables 5.1 and 5.2). For the rotamer A, the lifetime of isotopomers with 1 and 3 positions substituted ranges from 5.5 to 7.1 ns, for either 1 or 3 substituted from 3.0 to 4.0 and for deuterated isotopomers with neither 1 nor 3 substitution from 2.5 to 2.7 ns. One exception from this rule is the (1,4,6) isotopomer, with the short lifetime of 2.3 ns which is shorter than that of the hydroxy-undeuterated species.

For rotamer B no hydroxy-undeuterated species could be observed. An increase of the S_1 lifetime for the resorcinol B isotopomers is found with respect to the respective isotopomers of resorcinol A. Substitution of both hydroxy hydrogen atoms leads to lifetimes between 9.4 ns and 15.1 ns, while single hydroxy deuteration results in lifetimes between 4.6 to 6.6 ns.

5.4   Summary

In summary, for the interpretation of all 24 studied spectra we utilized the GA automated assignment [11, 12] with an asymmetric rotor Hamiltonian. The GA again proved its usefulness in the analysis of the many spectra acquired in this experiment. All spectra could be described within experimental accuracy as a-type spectra and the -OH torsional splittings remained unresolved for all resorcinol isotopomers.

We determined the *pseudo r_s*-structures of resorcinol's A and B rotamers in the S_0 and S_1 electronic states. Within obtained uncertainties and assumed model, both rotamers could be described with very similar geometrical parameters for both electronic states. The aromatic ring of resorcinol expands symmetrically, although there exists a trend for a slightly larger elongation of the whole molecule along the b inertial axis.

The extreme additivity of the zero-point energies after successive deuterations of the resorcinol rotamers was proven and subsequently used in the full assignment of the previously reported low resolution spectra of deuterated resorcinol A [1]. The analogous spectrum is also predicted for the resorcinol B rotamer. For that rotamer the additivity led to a correction of the undeuterated $S_1 \leftarrow S_0$ origin to 36193.78(4) cm^{-1}. The additivity of the ZPE shifts is a clear indication of the local oscillator behaviour of the CH and OH vibrations in these molecules.

References

[1] M. Gerhards, C. Unterberg, and S. Schumm. Structure and vibrations of dihydroxybenzene cations and ionization potentials of dihydroxybenzenes studied by

mass analyzed threshold ionization and infrared photoinduced rydberg ionization spectroscopy as well as *ab initio* theory. *J. Chem. Phys.*, 111:7966–7975, 1999.

[2] T. M. Dunn, R. Tembreull, and D. M. Lubman. Free-jet spectra and structure of *o*-, *m*- and *p*-dihydroxybenzenes. *Chem. Phys. Lett.*, 121:453–457, 1985.

[3] M. Gerhards, W. Perl, and K. Kleinermanns. Rotamers and vibrations of resorcinol obtained by spectral hole burning. *Chem. Phys. Lett.*, 240:506–512, 1995.

[4] M. Gerhards, M. Schiwek, C. Unterberg, and K. Kleinermanns. OH stretching vibrations in aromatic cations: IR/PIRI spectroscopy. *Chem. Phys. Lett.*, 297:515–522, 1998.

[5] P. Imhof, R. Brause, and K. Kleinermanns. Determination of ground state vibrational frequencies of jet-cooled resorcinol by means of dispersed fluorescence spectroscopy and *ab initio* calculations. *J. Mol. Spectr.*, 211:65–70, 1985.

[6] W. Caminati, S. Melandri, and L. B. Favero. Microwave spectroscopy of hydroquinone: The rotational spectrum of the *cis* conformer. *J. Chem. Phys.*, 100:8569–8572, 1994.

[7] S. Melandri, G. Maccaferri, W. Caminati, and P. G. Favero. Conformational equilibrium in resorcinol by means of the free-jet absorption millimeter wave spectrum. *Chem. Phys. Lett.*, 256:513–517, 1996.

[8] Ch. Ratzer, J. Küpper, D. Spangenberg, and M. Schmitt. The structure of phenol in the S_1-state determined by high resolution UV-spectroscopy. *Chem. Phys.*, 283:153–169, 2002.

[9] S. J. Humphrey and D. W. Pratt. High resolution $S_1 \leftarrow S_0$ fluorescence excitation spectra of hydroquinone. distinguishing the *cis* and *trans* rotamers by their nuclear spin statistical weights. *J. Chem. Phys.*, 99:5078–5086, 1993.

[10] H. D. Rudolph. Contribution to the systematics of r_0-derived molecular structure determinations. *Struct. Chem.*, 2:581–588, 1991.

[11] J. A. Hageman, R. Wehrens, R. de Gelder, W. Leo Meerts, and L. M. C. Buydens. Direct determination of molecular constants from rovibronic spectra with genetic algorithms. *J. Chem. Phys.*, 113:7955–7962, 2000.

[12] W. Leo Meerts, M. Schmitt, and G. Groenenboom. New applications of the genetic algorithm for the interpretation of high resolution spectra. *Can. J. Chem.*, 82:804–819, 2004.

[13] M. Schmitt, J. Küpper, D. Spangenberg, and A. Westphal. Determination of the structures and barriers to hindered internal rotation of the phenol-methanol cluster in the S_0 and S_1 state. *Chem. Phys.*, 254:349–361, 2000.

[14] R.V. Pound. Electronic stabilization of microwave ocillators. *Rev. Sci. Instrum.*, 17:490–505, 1946.

[15] R.W.P. Drewer and J.L. Hall and F.V. Kowalski and J. Hough and G.M. Ford and A.J. Munley and H. Ward. Laser phase and frequency stabilization using an optical resonator. *Appl. Phys. B*, 31:97–105, 1983.

[16] S. Gerstenkorn and P. Luc. *Atlas du Spectre d'Absorption de la Molécule d'Iode*. CNRS, Paris.

[17] H. C. Allen and P. C. Cross. *Molecular Vib-Rotors*. Wiley, New York, 1963.

[18] Y. R. Wu and D. H. Levy. Determination of the geometry of deuterated tryptamine by rotationally resolved electronic spectroscopy. *J. Chem. Phys.*, 91:5278–5284, 1989.

[19] A. Pieretti, F. Ramondo, L. Bencivenni, and M. Spoliti. Complexes of dihydroxybenzenes with carbon monoxide by DFT calculations and FT-IR matrix spectroscopy. *J. Mol. Str.*, 560:315–326, 2001.

[20] M. Schmitt, Ch. Ratzer, Ch. Jacoby, and W.L. Meerts. Structure and barrier to internal rotation of 4-methylstyrene in the S_0- and S_1-state. *J. Mol. Spectr.*, 2005.

[21] E.W. Gordy and R. L. Cook. *Microwave Molecular Spectra*. John Wiley & Sons, New York, 3rd edition, 1984.

[22] C.C. Costain. Determination of molecular structures from ground state rotational constants. *J. Comp. Phys.*, 29:864, 1958.

[23] J. Kraitchman. Determination of molecular structure from microwave spectroscopic data. *Am. J. Phys.*, 21:17, 1953.

[24] James K. G. Watson. The estimation of equilibrium molecular structures from zero-point rotational structures. *J. Mol. Spectr.*, 48:479–502, 1973.

[25] J. G. Smith and James K. G. Watson. A test of the r_m method of structure determination. *J. Mol. Spectr.*, 69:47–52, 1978.

[26] James K. G. Watson, Artur Roytburg, and Wolfgang Ulrich. Least-squares mass-dependence molecular structures. *J. Mol. Spectr.*, 196:102–119, 1999.

[27] James K. G. Watson. Mass derivatives of molecular parameters and distortions in the $r_m^{(2)}$ structures. *J. Mol. Spectr.*, 207:16–24, 2001.

[28] T. Mitsunaga, A. H. Conner, and Ch. G. Hill Jr. Predicting the hydroxymethylation rate of phenols with formaldehyde by molecular orbital calculation. *J. Wood Sci.*, 48:153–158, 2002.

Twisted intramolecular charge transfer (TICT) states. Rotationally resolved fluorescence excitation spectra of 4,4′-dimethylaminobenzonitrile (DMABN) in a molecular beam [1]

Abstract

We report the observation at high resolution of seven vibronic bands that appear within ~ 200 cm^{-1} of the electronic origin in the $S_1 \leftarrow S_0$ fluorescence excitation spectrum of 4,4′-dimethylaminobenzonitrile (DMABN) in a molecular beam. Surprisingly, each band is found to be split into two or more components by a (coordinated) methyl group tunnelling motion, which significantly complicates the analysis. Despite this fact, high quality (Observed Minus Calculated ≤ 30 MHz) fits of each of the bands have been obtained, from which the rotational constants, inertial defects, torsion-rotation interaction constants, methyl group torsional barriers, and transition moment orientations of DMABN in both electronic states have been determined. The data show that DMABN is a slightly pyramidalized ($\sim 1°$), but otherwise (heavy-atom) planar molecule in its ground S_0 state, and that its electronically excited S_1 state has both, a more pyramidalized ($\sim 3°$) and twisted ($\sim 25°$) DMA group. Large reductions in the methyl group torsional barriers also show that the $S_1 \leftarrow S_0$ electronic transition is accompanied by significant charge transfer from the nitrogen atom to the π^* orbitals of the aromatic ring. Thereby established for the first time is the participation of all three vibrational coordinates in the dynamics leading to the 'anomalous' emissive behaviour of DMABN in the condensed phase.

6.1   Introduction

Literally hundreds (if not thousands) of publications have appeared in the past 50 years concerning the properties of 4,4′-dimethylaminobenzonitrile (DMABN) and related molecules in their ground and electronically excited states. Mainly, this is because of its 'anomalous' emission spectrum in the condensed phase. In addition to the normal fluorescence that is always present, DMABN exhibits an additional, red-shifted emission in polar solvents that was first attributed by Lippert *et al.* [1–3] to an intramolecular charge transfer (ICT) state. Later, recognizing that charge separation and/or flow would be inhibited by orbital overlap between the two ends of the molecule, Grabowski and coworkers [4] suggested that the process involved an internal twisting of the dimethylamino (DMA) group. Such a motion would facilitate 'permanent' transfer of electrons from the amino nitrogen to a π^* orbital extending over the aromatic ring. This hypothesis, leading to the concept of twisted intramolecular charge transfer (TICT) states, was then tested in an extensive series of experiments by Grabowski, Rotkiewicz, Rettig and many others [5]. In the following years, other competing models of structural relaxation were proposed, including the so-called planar ICT (PICT) model advocated by Zachariasse and co-workers [6, 7].

Despite the passage of time, the intense controversy generated by these proposals, and the extensive application of ICT molecules as fluorescence markers, sensors, and 'switches' in materials science and in biology, very little is known about their electronic and geometric structures. Gas phase, fluorescence excitation spectra of DMABN in supersonic jets were first reported by Kobayashi *et al.* [8], Gibson *et al.* [9] and Bernstein and co-workers [10–13]. Significant activity of several vibrational modes lying within the first 200 cm^{-1} of the origin was detected in both the excitation and emission spectra and attributed to both DMA inversion and twisting motions. Kajimoto and coworkers [14] measured the microwave spectrum of DMABN and found the ground state to be nearly planar with an inversion angle of about 15°. They also observed a partially resolved rotational band contour of the S_1–S_0 electronic spectrum of DMABN and concluded that, in the S_1 state, the DMA group is rotated by 30° from the aromatic plane. Salgado *et al.* [15] reported on the basis of similar laser experiments on the isolated molecule that the LIF spectrum contained two types of contours, b-type bands that belonged to a 'planar' excited state and c-type bands that belonged to a 'twisted' excited state. But Saigusa *et al.* [16] suggested on the basis of a re-examination of the low resolution spectra of DMABN-h_6 and -d_6 that all bands terminate in an S_1 state that is twisted by about 26° with a small 150 cm^{-1} barrier to planarity. The structure and dynamical behavior of S_1 DMABN also have been the subject of many theoretical calculations, most recently using TDDFT methods [17].

Reported here are the results of rotationally resolved fluorescence excitation experiments on DMABN in a molecular beam. The data give information about the equilibrium geometry of the molecule in its ground electronic state, about the equilib-

rium geometry of the molecule in its excited electronic state, and about the differences in the electronic distributions of the two states. Studies of seven different vibronic bands in the S_1–S_0 spectrum show that DMABN is an essentially planar molecule in its S_0 state, that it is a slightly pyramidal, significantly twisted molecule in the S_1 state, and that significant charge transfer is facilitated by vibrational motion along these coordinates. Thereby established for the first time is a direct connection between the properties of the isolated molecule and its behavior in the condensed phase.

6.2 Experimental and Analysis

DMABN was purchased from Aldrich and used without further purification. Low resolution experiments to determine the frequencies of the transitions for subsequent examination at high resolution were performed as described elsewhere [18]. The high resolution data were obtained using two molecular beam laser spectrometers [19, 20]. The sample was heated to about 150°C, seeded into 500 torr of argon, expanded through a 150 μm quartz nozzle, skimmed once, and crossed 15 cm downstream of the nozzle by a single frequency, tunable visible laser, intracavity frequency doubled into the UV. Reduction of the Doppler width to approximately 20 MHz was accomplished by active control of the angle between the laser and molecular beams, which was as close to 90° as possible, and by spatially selective detection optics, which collects light from a ~ 0.7 mm diameter sphere located at the center of the crossing point. The laser is a Spectra-Physics Ar^+-pumped ring dye laser (Models 171 and 380D) that has been modified for intracavity frequency doubling and extended tuning over ranges (in the UV) of up to 7 cm^{-1}. The homogeneous linewidth of the laser is less than 1 MHz. In a typical experiment, the laser was scanned across the width of a single band, producing fluorescence at selected wavelengths that was detected by a PMT and photon-counting system and processed by a computer-controlled data acquisition system. As will be seen, each spectrum consists of thousands of lines which connect the populated rotational levels of the the ground state with the corresponding, accessible rotational levels of the excited electronic state.

The spectra were analyzed using the effective Hamiltonian for an asymmetric molecule with two equivalent CH_3 internal rotors discussed by Tan *et al.* [21]. An extensive initial search for the best fit parameters for each of the spectra was performed with the automated assignment technique based on genetic algorithms (GA) developed in Nijmegen [22, 23]. These results were then subsequently used to perform line assignments with Plusquellic's program jb95 [24] and a detailed fit of these assignments to the effective Hamiltonian. *Ab initio* calculations were performed using Gaussian 98 [25].
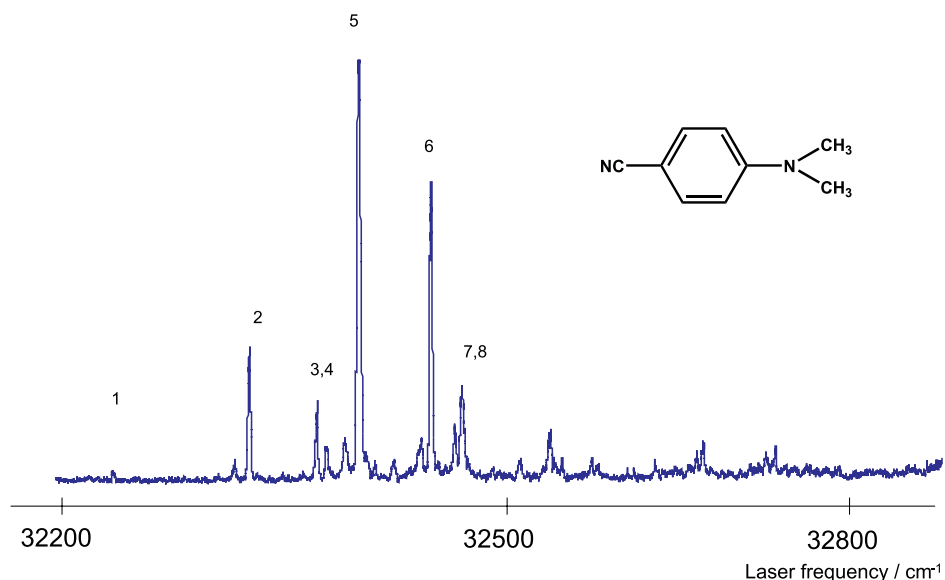
Figure 6.1: Vibrationally resolved fluorescence excitation spectrum of DMABN.

6.3   Results

Fig. 6.1 shows the low resolution fluorescence excitation spectrum of DMABN. Similar to the spectra recorded by others [8–10], the spectrum has a weak origin band at $\sim$ 32247 cm^{-1} but exhibits many strong features within the first 200 cm^{-1} of the origin. These have been assigned most recently by Saigusa *et al.* [16], as involving DMA torsional, DMA inversion, and methyl torsional motions. These assignments are listed in Table 6.1. Similar low frequency activity is built on higher energy vibronic transitions displaced by $\sim$ 600 cm^{-1}, *etc.* from the origin, as in the case of other substituted benzenes. Thus, apart from this low frequency activity, the S_1 state of DMABN in the gas phase appears to be a normal, locally excited $\pi\pi^*$ state of a typical aromatic molecule.

To date, our high resolution study has been confined to the seven strongest bands in the first low frequency progression. The origin band proved too weak to record under the present conditions. Fig. 6.2 shows the rotationally resolved spectrum of band 2, located at 32322 cm^{-1} (+ 76 cm^{-1}). The entire spectrum contains in excess of 3000 lines and spans over 3 cm^{-1} at a rotational temperature of 4 K. Initial attempts to fit this spectrum showed that it contains at least two closely spaced subbands with similar inertial parameters [26]. A weak third subband was discovered in refinements of the fit with the computer assisted GA. Thus, it was determined that three distinct

Table 6.1: Observed vibrational bands in the $S_1 \leftarrow S_0$ fluorescence excitation spectrum of $4{,}4'$-dimethylaminobenzonitrile (DMABN).

Band	Band origin $(\text{cm}^{-1})^{(a)}$	Shift from origin (cm^{-1})	Assignment[b]	ΔI avg $(\text{amu}\times\text{Å}^2)$ [c]
1	32246.73	0	Origin	(Not observed)
2	32322.33	75.6	τ_0^2	-12.27
3	32360.15	113.4	I_0^2	-12.50
4	32365.60	118.9	$\tau_0^1 Mh_0^1$	-14.22
5	32383.37	136.6	τ_0^4	-11.47
6	32423.64	176.9	τ_0^6	-11.93
7	32436.92	190.2	$\tau_0^2 I_0^2$	-13.46
8	32440.77	194.0	$\tau_0^3 Mh_0^1$	-12.11

[a] Calculated from the observed G-G subband origin frequency (Table 6.2).

[b] S_1 vibrational levels that participate in the indicated transition: τ denotes DMA torsion, I denotes DMA inversion and Mh denotes methyl torsion (see Ref. [16]).

[c] Average values for all subbands lying within the indicated band.

rotational contours, separated by ~ 3 GHz and with relative intensities of $\sim$ 1:2:1, comprise band 2. There are approximately 1000 lines in each subband.

Refined values of the rotational constants of the two states that participate in band 2 were obtained by first fitting the strong subband. A simulated spectrum of this subband was generated using the previously measured rotational constants of the ground state [14] and CIS 6-31+G values for the excited state. This was sufficient to reproduce its main features. Then, assisted by the GA results, 'copies' of this spectrum were shifted to the approximate origins of the two remaining subbands until their main features were reproduced as well. Assignments of the several transitions in each of the subbands were then made and refined values of the rotational constants were obtained, using a least squares fitting procedure.

An important result of this exercise was the discovery that only one of the three subbands, the lowest frequency one, could be fit using rigid rotor Hamiltonians for both states. The two higher frequency bands required the addition of terms linear in the angular momentum quantum numbers to the Hamiltonian of the excited state. As discussed elsewhere [21], terms of this sort arise from the coupling of overall rotation
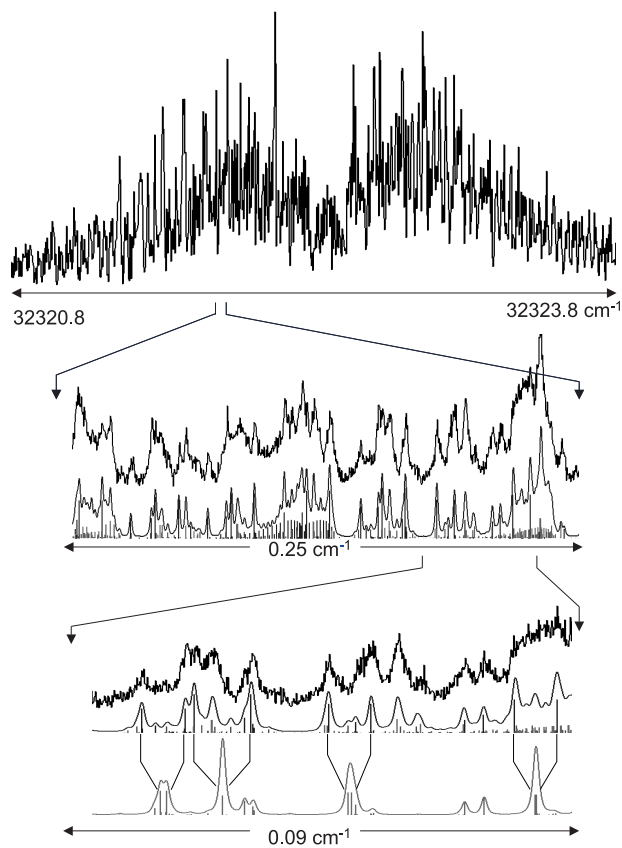
Figure 6.2: Rotationally resolved fluorescence excitation spectrum of band 2 in DMABN. Shown in the middle is a small portion of the experimental spectrum, the fitted spectrum with a convoluted lineshape function, and the individual lines of the separate subbands that contribute to the spectrum in this region. Illustrated at the bottom is a still smaller portion of the spectrum showing the first-order torsion-rotation splittings for (left to right) transitions $[J', K'_a, K'_c - J'', K_a'', K_c''] = [10,3,8 - 11,4,7]$, $[4,4,1 - 5,5,0]$, $[9,3,7 - 10,4,6]$ and $[8,3,5 - 9,4,6]$. Among the splittings shown, the one involving the degenerate pair $[4,4,1 - 5,5,0]$ and $[4,4,0 - 5,5,1]$ is the largest.

with another source of angular momentum, such as internal rotation. The principal experimental evidence for this conclusion are splittings observed in some of the lines, especially those connecting levels having K_a nearly equal to J. These transitions are near degenerate in the case of near prolate asymmetric rotor. However, addition of

Table 6.2: Ground state inertial parameters derived from fits of bands 2-8 in the S_1–S_0 electronic spectrum of DMABN. All parameters are in MHz, except for ΔI in amu$\times$Å^2.

Band		A	B	C	ΔI	Origin Freq.
2	A-A	3470.3(4)	578.7(3)	499.6(1)	-7.41(40)	968995908
	G-G	3470.5(5)	578.6(2)	499.5(1)	-7.46(20)	+3052.6
3	A-A	3470.0(5)	578.6(1)	499.7(1)	-7.76(20)	970118243
	G-G	3470.0(5)	578.6(1)	499.7(1)	-7.75(20)	+14702
4	A-A	3468.9(8)	578.6(3)	499.5(2)	-7.34(40)	970296024
	G-G	3469.6(5)	578.6(2)	499.6(2)	-7.59(40)	+372.4
5	A-A	3469.3(10)	578.6(2)	499.6(1)	-7.49(30)	970814803
	G-G	3469.4(20)	578.6(2)	499.5(1)	-7.47(30)	+14250
6	A-A	3470.9(8)	578.8(1)	499.8(1)	-7.57(20)	972035675
	G-G	3471.0(8)	578.8(1)	499.7(1)	-7.57(15)	+524.5
7	A-A	3471.2(7)	578.8(1)	499.8(1)	-7.63(20)	972422232
	G-G	3471.4(7)	578.9(1)	499.9(1)	-7.56(20)	+12092
8	A-A	3470.6(6)	578.8(1)	499.8(1)	-7.64(15)	972522977
	G-G	3470.5(6)	578.8(1)	499.8(1)	-7.57(15)	+26814

linear terms to the Hamiltonian removes this degeneracy. A specific example from the strong subband is shown in Fig. 6.2, where two fits, with and without linear terms, are compared.

The final fit of band 2 utilized 198 assigned lines for the first subband, 333 lines for the second subband and 91 lines for the third subband, with standard deviations of 10.7, 8.1 and 20.1 MHz, respectively. One possible explanation for the high (Observed – Calculated) (OMC) of the third subband is the high density of lines and low signal-to-noise. Another is that this subband (the E subband) is predicted to consists of two overlapping transitions (the E_1+E_3 subbands) [21]. For this reason, we also fit the entire spectrum using GA and the model Hamiltonian, completely reproducing the entire spectrum. The inertial constants derived from the two fits were the same, within experimental error.

All subbands in band 2 are mainly b-type bands. Owing to band congestion, the possible contributions of other band types could not be determined. The resulting inertial constants of both ground and excited state are accurate to at least ± 1 MHz. The ground state values compare favorably to the earlier microwave values [14]. Typ-

Table 6.3: Excited state inertial parameters derived from fits of bands 2-8 in the S_1–S_0 electronic spectrum of DMABN. All parameters are in MHz, except for ΔI in amu×Å^2.

Band		A	B	C	D_a	D_b	ΔI
2	A-A	3405.6(4)	575.5(3)	498.2(2)			-12.19(30)
	G-G	3405.0(5)	575.3(2)	498.1(2)	42.4(30)	24.5(400)	-12.34(20)
3	A-A	3374.5(1)	576.8(1)	498.4(5)			-12.00(30)
	G-G	3396.2(5)	575.6(1)	498.5(1)	186.0(3)	44.6(200)	-12.99(20)
4	A-A	3374.7(7)	576.0(3)	498.8(2)			-14.07(40)
	G-G	3375.8(7)	576.0(2)	499.0(1)	7.0(3)	0	-14.36(30)
5	A-A	3400.1(10)	576.3(2)	498.4(1)			-11.69(40)
	G-G	3394.6(20)	576.4(1)	498.1(1)	305.4(5)	28.2(20)	-11.25(10)
6	A-A	3401.4(7)	575.7(1)	498.3(1)			-12.17(10)
	G-G	3401.3(5)	576.1(1)	498.3(1)	118(3)	10(30)	-11.68(10)
7	A-A	3394(3)	576.6(1)	499.2(1)			-12.87(10)
	G-G	3383.1(5)	576.4(1)	499.3(1)	192.4(2)	37(20)	-14.04(20)
8	A-A	3407.3(5)	576.5(1)	498.8(1)			-11.87(10)
	G-G	3397.7(1)	576.3(1)	498.7(1)	554(4)	82.4(8)	-12.34(20)

ically, microwave values are more precise, but in this case only eight pure rotational transitions were measured, making the precision in our experiment at least as high as the microwave one. Individual lines identified in the fitting process have FWHM's of about 50 MHz. Examination of the individual lineshapes suggests approximately equal contributions to them from Doppler and lifetime broadening. The 5 ns fluorescence lifetime measured for DMABN in the gas phase by Howells *et al.* [27], suggests a Lorentzian contribution to the linewidth of 32 MHz. The results for band 2 are summarized in Tables 6.2 and 6.3, which separately list the ground and excited state parameters of all seven studied bands of DMABN. The results for the E subbands are not reported here owing to their high OMC values. Standard deviations increase for the lower intensity subband fits, as the number of readily assignable transitions is smaller.

Fig. 6.3 shows the rotationally resolved spectra of the remaining six bands, bands 3-8. Band 3, observed at $\sim$ 32360 cm^{-1} (+ 113 cm^{-1}), contains more than 2000 lines and, even though it appears to be a *b*-type band (no obvious Q branch), one can immediately see that there is significant intensity in the region where a Q-branch
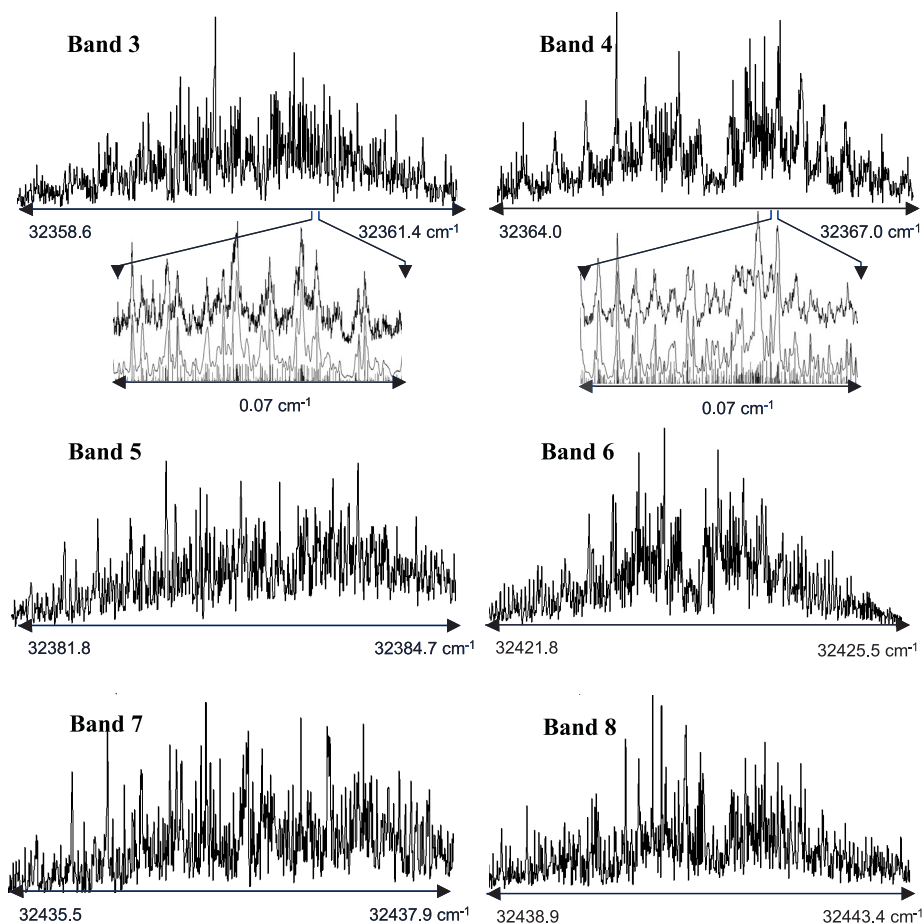
Figure 6.3: Rotationally resolved fluorescence excitation spectra of bands 3-8 in the S_1–S_0 electronic transition of DMABN.

would have been expected. This prompted us to again look for the presence of sub-bands. Using procedures similar to those described above, it was determined that three subbands are present in band 3, separated by ~ 15 GHz with relative intensities of ~ 2:5:3, and linewidths comparable to those in band 2. The final fit of band 3 utilized 41 assigned lines for the first subband, 369 lines for the second subband and 75 lines for the third subband, with standard deviations of 19.8, 5.0 and 13.1 MHz, respectively. A contour GA fit again reproduced the spectrum of the third subband.

The rotationally resolved spectrum of band 4, observed at $\sim$ 32366 cm^{-1}(+ 119 cm^{-1}), has a different appearance. It is significantly more congested than bands 2 and 3. This is due to the presence of three closely spaced subbands, separated by $\sim$ 370 MHz, with relative intensities of $\sim$ 2:6:3. As in the previous cases, we attempted to fit the spectrum with rigid rotor Hamiltonians for both electronic states. However, as before, it was required to introduce linear terms into the excited state Hamiltonian of the two higher frequency subbands. The final fit of band 4 utilized 52 assigned lines for the first subband, 272 lines for the second subband and 137 lines for the third subband, with standard deviations of 8.5, 11.3 and 7.9 MHz, respectively.

Band 5, observed at $\sim$ 32383 cm^{-1} (+ 137 cm^{-1}), is the strongest band in the studied frequency range and was obtained with the highest signal-to-noise. Despite this fact, lines of only two subbands could be assigned. These bands are separated by $\sim$ 14 GHz with a relative intensity of $\sim$ 1:2. It was sufficient to use rigid rotor Hamiltonians for the ground and excited states of the lower frequency subband, while some linear terms were required to fit the stronger, higher frequency subband. The final fit of this spectrum was based on the assignment of 112 lines for the first subband and 114 for the second, with standard deviations of 3.9 and 4.5 MHz, respectively. A GA fit of the full spectrum showed the presence of a third subband shifted another $\sim$ 14 GHz to the blue.

Band 6, observed at $\sim$ 32424 cm^{-1} (+ 177 cm^{-1}), is the second strongest band in the studied frequency range and is similar in all respects to band 5 (*cf.* Fig. 6.3). At first glance, band 6 appears to contain two subbands with relative intensity of $\sim$ 1:2. In this case, the spacing of two subbands is $\sim$ 500 MHz. Analogous to band 5, the lower intensity (low frequency) subband in band 6 could be fit using only rigid rotor Hamiltonians for both states, while the higher intensity subband required introduction of linear terms in the Hamiltonian of the excited state. The fit was based on 78 assignments for the first subband and 206 assignments for the second subband, with standard deviations of 2.9 and 1.5 MHz, respectively. A GA fit pointed to the existence of a third subband at still higher frequency about 500 MHz to the blue.

Band 7, observed at $\sim$ 32437 cm^{-1} (+ 190 cm^{-1}), appears to again contain only two subbands, split by $\sim$ 12 GHz, with a relative intensity of $\sim$ 4:7. 324 lines were assigned for the weaker subband and 225 for the stronger one, with standard deviations of 2.8 and 2.1 MHz, respectively. The lower intensity subband was fit using only rigid rotor terms in the Hamiltonian. The higher intensity subband contained characteristic internal rotation splittings, analogous to those observed in other bands, which required the addition of linear terms to the Hamiltonian of the excited state. A third subband was again shown to be present in band 7 by the GA fit.

The rotationally resolved spectrum of band 8 was observed at $\sim$ 32441 cm^{-1} (+ 194 cm $^{-1}$). Band 8 was initially identified as *b*-type, with no apparent splittings. Only after the initial fit was performed, using a Hamiltonian with internal rotation terms in the excited state, was significant additional intensity observed in the lower

frequency portion of the spectrum. This new intensity was accounted for by the introduction of a second subband, shifted by an unprecedented ~ 27 GHz to the red, with relative intensity of $\sim 1{:}2$. 196 lines were assigned for the lower intensity subband and 162 lines were assigned for the higher intensity subband, resulting in standard deviations of the fit of 2.2 and 2.4 MHz, respectively. The remaining intensity in the highest frequency part of the spectrum (not shown in Fig. 3) could be attributed to a third subband with a GA calculation.

It is important to note at this juncture that each of the rotational constants listed in Tables 6.2 and 6.3 contains second-order contributions due to the torsion-rotation interaction. However, from an estimate of the torsional barriers (*vide infra*), it can easily be shown that these contributions are small, of the order 0.01 MHz or less (except for band 8, where they approach 10 MHz). Therefore, they are neglected in what follows. We also reiterate here that all studied bands 2-8 are b-type bands and exhibit the same single rovibronic linewidths, 50 MHz or so. This demonstrates that these bands all access upper state vibrational levels which have comparable lifetimes.

The values presented in Table 6.1 are from the G-subband origins of the high resolution spectra from Table 6.2. These are the best numbers for the low resolution unresolved spectra since the weighted intensities of the A, G and E subbands coincides exactly with the G origin.

6.4   Discussion

6.4.1   Structural considerations

Examination of the ground state rotational constants in Table 6.2 reveals that the values of A, B and C of bands 2-8 are all the same, within experimental error. This shows that all seven bands originate in the same vibrational level of DMABN, presumably the zero-point level of its S_0 state. The different transitions cannot be hot bands, nor can they belong to different conformers of DMABN. Each of these possibilities would require that the ground state rotational constants of the different bands be different.

To interpret these values, we first performed a number of theoretical calculations. At the HF/6-31+G level, DMABN converges to a 'planar' structure; the CN group and the heavy atoms of the DMA group all lie in the aromatic plane. Importantly, this structure has significantly different inertial parameters from the observed one, as shown in Table 6.4. 'Planar' DMABN has an inertial defect ($\Delta I = I_c - I_a - I_b$) of -6.28 amu$\times$Å^2 whereas the experimental structure has $\Delta I = -7.56$ amu$\times$Å^2. (This is the average value for all seven bands). A large fraction of the observed inertial defect comes from the out-of-plane C-H bonds of the two methyl groups. For comparison, the inertial defect of 2,3-dimethylnaphthalene in its S_0 state is -6.55 amu$\times$Å^2 [21]. But there must be at least one other out-of-plane contribution in DMABN.

Table 6.4: Calculated and observed inertial parameters of DMABN in its ground and electronically excited states.

	Parameter	Experiment (average values)	MW [a]	HF/6-31+G	Fit
S_0	A (MHz)	$3470.3^{(d)}$	3470.0	3499.1	$3487.7^{(b)}$
	B (MHz)	$578.7^{(d)}$	578.6	580.5	$583.6^{(b)}$
	C (MHz)	$499.7^{(d)}$	499.6	501.0	$503.7^{(b)}$
	ΔI (amu×Å^2)	$-7.56^{(d)}$	-7.36	-6.28	$-7.54^{(b)}$
				CIS/6-31+G	
S_1	A (MHz)	$3405.6^{(e)}$		3395.6	$3395.4^{(c)}$
	B (MHz)	$575.5^{(e)}$		578.8	$577.4^{(c)}$
	C (MHz)	$498.2^{(e)}$		497.5	$499.1^{(c)}$
	ΔI (amu×Å^2)	$-12.19^{(e)}$		-6.14	$-11.58^{(c)}$

[a] Microwave values from Ref. [14].
[b] Modified theoretical structure of ground state with inversion angle = 18.6^o, CNC angle = 122°.
[c] Modified theoretical structure of excited state with twist angle = 25°, inversion angle = 30°.
[d] Average values for all subbands.
[e] Values for the A subband in band 2.

Additional contributions to the inertial defect may originate from pyramidalization of the N atom or twisting of the DMA group. To distinguish these contributions, one may consider also the values of the A rotational constant. Twisting the DMA group of a flat DMABN does not affect this parameter but pyramidalization does. Thus, 'best-fit' values of the degrees of pyramidalization and twist may be obtained by simultaneously changing them until the calculated values of A and ΔI match those of the experimental structure. No twist was necessary in the ground state. Pyramidalization of the DMA group by 1°, giving an inversion angle of 17.2^o, yields a structure with $\Delta I = -7.36$ amu×Å^2. Additional refinement is possible by varying the angle between methyl groups. Our 'best-fit' structure has an inversion angle of 18.5^o and an angle between the methyl groups of 122°, giving $\Delta I = -7.54$ amu×Å^2 as shown in Table 6.4. Earlier microwave studies [14] estimated an inversion angle of 15°. The corresponding angle in the ground state of aniline is $\sim 38^o$ [28].

Fig. 6.4 shows a plot of the dependence of the inertial defect of DMABN on the
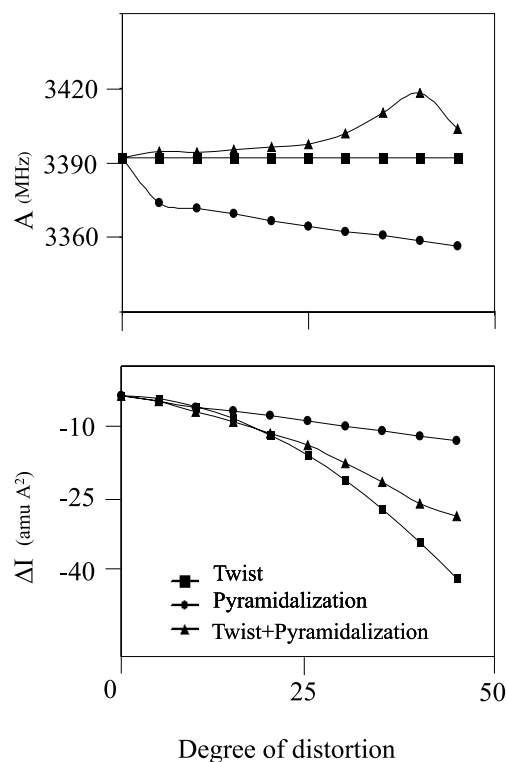
Figure 6.4: Plots of the A rotational constant (in MHz, top) and inertial defect (in amu×Å^2, bottom) of DMABN as a function of distortion along different vibrational coordinates (see legend).

inversion and twist angles of the DMA group. These data were obtained by distorting the HF/6-31+G structure along each coordinate, 'freezing' the motion along all others, and calculating the changes in ΔI and A. The magnitude of ΔI increases along both coordinates. But, for reasonable values of both parameters, ΔI is much more sensitive to the torsional motion of the DMA group owing to the presence of the 'off-axis' methyl groups.

Table 6.3 shows that the values of A, B, and C, and ΔI in the different excited state levels accessed in bands 2-8 are mostly different, even among the different sub-bands accessed within a single band. As will be seen, these differences are significant, and provide key insights into the types of nuclear motion that are produced by the absorption of light. But, taken together, all values of A are about 2% smaller in the

S_1 state of DMABN whereas the values of B and C in the S_1 state are relatively unchanged, compared to the S_0 state. The values of the inertial defects in the S_1 state (ranging from -11 to -14 amu×Å^2) are about 40% larger than that of the ground state. It is expected that aromatic molecules expand upon $\pi\pi^*$ excitation, which causes the overall decrease in rotational constants. The relatively large decrease in A indicates that the benzene ring is taking on a quinoidal shape as in the excited state of aniline [28]. However, elongation of the 'perpendicular' bonds in the benzene ring cannot explain the larger (in magnitude) inertial defect values. This value is expected to remain unchanged at -6 – 7 amu×Å^2.

While large, the decrease in the magnitude of A in S_1 DMABN is significantly smaller than that in S_1 aniline [28]. Aniline has $\Delta A \sim$ -331.2 MHz, compared to $\Delta A \sim$ -65 MHz in DMABN. 4-Aminobenzonitrile has ΔA = -316.6 MHz [29]. While these are 'smaller' molecules, with larger A values (aniline has A = 5618 MHz in the S_0 state), the *percent* change in A is also much larger in aniline and 4-aminobenzonitrile ($\sim$6%) than in DMABN ($\sim$ 2%).

To account for the smaller change in A, and for the large change in the magnitudes of the inertial defects in the S_1 state of DMABN, the contributions of pyramidalization and twist again have to be considered, as in the case of the ground state (*cf.* Fig. 6.4). Beginning with a 'planar' DMABN, pyramidalization of at least 5° (giving an inversion angle of $\sim$ 38°) is required to fit the observed values of ΔI. These angles are substantially larger than the corresponding angles in the ground state, which seems unreasonable to us. A 'quinoidal' DMABN would have a flatter DMA group. Rotation of the DMA group by a twist angle of 17° with respect to the plane gives an inertial defect of -12.2 amu×Å^2, in good agreement with experiment. (The A subband in band 2 has $\Delta I = -12.19$ gmu Å^2.) However, twist angles τ_{min} of about 26° have been estimated from Franck-Condon fits of the vibrational progression in the low resolution spectrum [16]. Additionally, neither pyramidalization nor twisting the DMA group alone explains the relatively small ΔA value.

A unique solution to this problem is revealed only when one allows for *simultaneous* twisting and pyramidalization of the attached DMA group. Thus, starting with the modified *ab initio* structure of a hypothetical 'planar' DMABN, the experimental values of *both* ΔI and A in the S_1 state can be fit by twisting the DMA group by 25° about the 'C$_2$' axis *and* by pyramidalization of the nitrogen atom by 3°. This is shown explicitly in Fig. 6.5. Such a coordinated motion is intuitively obvious on chemical grounds. If a 'flatter' DMA group is a consequence of the conjugative interaction of the nitrogen lone pair π electrons and the electrons of the ring, then rotation of the DMA group with respect to the plane of this ring should reduce this interaction, and simultaneously allow for pyramidalization of the nitrogen atom. 'Tetrahedral' nitrogen atoms are more stable than 'trigonal' ones. Additionally, rotation of the DMA group also will produce a less quinoidal structure of the ring, since that structure also is a consequence of the same conjugative interaction. S_1 DMABN *must* have a
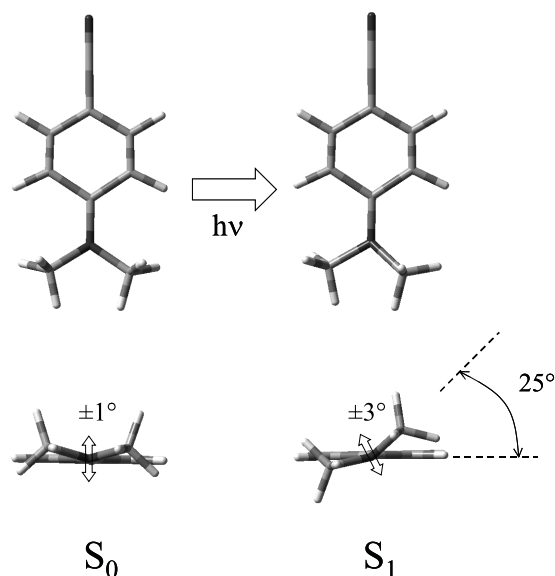
Figure 6.5: The TICT state. Schematic diagram illustrating the geometry changes that occur when DMABN absorbs light.

significantly less quinoidal structure than S_1 aniline, given the differences in their ΔA values.

6.4.2 The low resolution spectrum

That the DMA group is both twisted and pyramidalized in the S_1 state of DMABN is also apparent from its low resolution spectrum (Fig. 6.1). Saigusa *et al.* [16] have recently re-examined this spectrum, in dimethylaniline, in DMABN, and in several of their isotopomers. They also have given compelling assignments of most of the observed bands appearing in this spectrum up to an excess energy of ~ 350 cm^{-1}. A key factor in these assignments was the discovery of the DMABN-d_6 origin band, which made possible a more meaningful comparison of the frequencies and intensities of the different bands in the different isotopomers. Based on these assignments, it was concluded that the prominent low frequency progression involves the DMA torsional mode, with less significant contributions from DMA inversion and methyl group torsional motions. The S_1 state was found to be twisted by about 26°, with an effective two-fold barrier of ~ 190 cm^{-1} at the planar configuration. An inversion angle of 15° was estimated for DMABN in its S_0 state (compared to 0° for the S_1

state). The corresponding angles in dimethylaniline were estimated to be $27°$ (S_0) and $13°$ (S_1).

Our results both confirm and extend the results of Saigusa *et al* [16]. Listed in Table 6.1, in addition to the frequencies and displacements of the bands up to $\sim$ 200 cm^{-1} above the origin of DMABN, are the proposed assignments and measured inertial defects of the S_1 vibrational levels that participate in these transitions. Here, τ denotes DMA torsion, I denotes DMA inversion, and Mh denotes methyl torsion. Assignment of bands 2, 5 and 6 as the prominent progression along the DMA torsional coordinate ($\tau_0^2, \tau_0^4, \tau_0^6$; owing to symmetry, transitions are allowed only to even levels in S_1) is confirmed by their (average) inertial defects, -12.3, -11.5, and -11.9 amu$\times$Å^2, respectively. All of these values are large in magnitude compared to the ΔI value of the ground state, -7.56 amu$\times$Å^2. The data also provide further support for the presence of two minima in the S_1 potential along this coordinate. As one approaches the top of the barrier, $< \tau^2 >^{1/2}$ should first decrease and then increase, leading to a zig-zag behavior of ΔI as a function of τ [30]. This is precisely what is observed. Thus, there must be a maximum at the planar geometry along this coordinate in the S_1 state, if there is a minimum in the S_0 state. The ΔI data also quantitatively support the suggested S_1 barrier height of $\sim$ 190 cm^{-1} along this coordinate since all probed levels lie below this barrier.

Bands 3 and 4, and bands 7 and 8 also have substantially larger (in magnitude) inertial defects ($\Delta I = -12.5$ and -14.2, and -13.5 and -12.1 amu$\times$Å^2, respectively). These values are not only larger than those of the ground state, but they are also larger than the values for the τ^2, τ^4, and τ^6 torsional levels, evidencing substantial displacements along other out-of-plane coordinates. But ambiguities exist concerning the assignments of both pairs of these bands. Saigusa *et al.* [16] assigned bands 3 and 4 as I_0^2 and $\tau_0^1 Mh_0^1$, and bands 7 and 8 as $\tau_0^2 I_0^2$ and $\tau_0^3 Mh_0^1$, but noted that both assignments could be reversed. The torsional levels τ^0 (the zero-point level) and τ^1 should have increasingly negative values of ΔI, compared to the value for τ^2(-12.0 amu$\times$Å^2). Additional activity of the methyl torsional mode should not contribute greatly to ΔI. So, although it is difficult to be certain, the reversed assignment of band 3 to $\tau_0^1 Mh_0$ and band 4 to I_0^2 seems more reasonable to us. In that event, the value ΔI= -14.2 amu$\times$Å^2 seems too large in magnitude to attribute solely to the DMA twist. Additional displacement along the inversion coordinate away from 0^0 would explain the larger value. The barrier to inversion is likely to be quite small. So, the magnitude of the contribution to ΔI from inversion is expected to rise steeply with increasing displacement along this coordinate. For that reason, we are comfortable with the existing assignments of band 7 as $\tau_0^2 Mh_0^2$ (with ΔI = -13.5 amu$\times$Å^2) and band 8 as $\tau_0^3 Mh_0^1$ (with ΔI = -12.1 amu$\times$Å^2) but more data will be necessary to confirm this conclusion.

6.4.3   Methyl group torsional motions

Revealed by the high resolution spectra for the first time is additional vibrational motion along the methyl group torsional coordinate of DMABN in its S_1 electronic state. The primary evidence for this motion are the splittings that are observed in the spectra. Each observed high resolution band is split into two or more components, and the different components exhibit different splittings and different relative intensities. Importantly, these relative intensities are independent of backing pressure, showing that they are dictated primarily by the different nuclear spin statistical weights (NSSW's) of the affected levels, not by their relative temperatures, Franck-Condon factors, and/or oscillator strengths. Of the possible feasible tunneling pathways that could be responsible for these NSSW's, inversion of the DMA group would produce two subbands with the same relative intensities, rotation of a single methyl group would produce two subbands with different relative intensities, and (coordinated) rotation of two equivalent methyl groups would produce three or more subbands with different relative intensities. The last possibility is the only one that is consistent with the experimental data.

DMABN is a two-top molecule. In the absence of coupling between the two tops, the effective torsional Hamiltonian is [21]:

$$H_{eff}^T = Fp_1^2 + \frac{1}{2}V_3^*(1 - 3cos\phi_1) + Fp_2^2 + \frac{1}{2}V_3^*(1 - 3cos\phi_2), \qquad (6.1)$$

where F is the reduced rotational constant for the motion described by the angles ϕ_1 and ϕ_2, p_1 and p_2 are the angular momenta of the two rotors, and V_3^* is an effective hindering potential. A single methyl rotor governed by a potential of this type has three torsional levels for each torsional quantum number v, a single A torsional level and two E torsional levels. Degenerate in the infinite barrier limit, the three levels are split by tunneling through a finite barrier (the A-E splitting) and by torsion-rotation interactions (the E-E splitting). A similar situation exists for two equivalent methyl rotors. Here, the original nine-fold (3 x 3) degeneracy is split by tunneling into three groups of levels, labeled by A_1, G, and E_1+E_3. The different levels can be distinguished by their different NSSW's, approximately 1:2:1 for A_1:G:E_1+E_3 levels. Each of the different sub-torsional levels also has its own effective rotational Hamiltonian, since the motions (and the magnitudes of torsion-rotation coupling) that occur in each of the levels are not the same.

In general, the tunneling splitting in different electronic states also is not the same because the potentials governing the torsional motion are not the same. The separations between the A_1, G, and E_1+E_3 levels in each state are expected to be different. Thus, a single band in an electronic spectrum is split into three components, the A_1-A_1 (A) subband, the G-G (G) subband, and the $[(E_1+E_3) - (E_1+E_3)]$ (E) subband. The separations between the subbands are measures of the difference in the V_3^* values in the two states. When all three subbands are observed, the two

separations should be equal if the rotors are independent; *i.e.*, if rotor-rotor coupling is small. In favorable cases, these criteria can be used to distinguish rovibrational transitions belonging to one subband from those belonging to another. The separate subbands can be fit using their own, unique rotational Hamiltonians, and the derived values of the torsion-rotation interaction terms can be used to obtain independent estimates of the V_3^* values in both electronic states.

We proceed as follows. First, we note that the different subbands within each band of DMABN can each be identified by differences in their intensities. Next, we note that the different subbands always appear in the same energy sequence; A, G, and E in each band. This means that the three-fold barrier in the S_1 state is less than that in the S_0 state $[V_3^*(S_1) < V_3^*(S_0)]$. Next, we note that only the excited state sub-torsional levels G and E are split by the torsion-rotation interaction. D_a, D_b, and D_c are all zero (within experimental error) for the corresponding ground state sub-torsional levels. This means that the ground state barrier is on the order of 500 cm^{-1} or more, and that, to a first approximation, the A, G and E sub-torsional levels belonging to $v'' = 0$ in the ground state are degenerate. This is not a surprising result. The CH$_3$ torsional barrier in the electronic ground state of CH$_3$NH$_2$ is $\sim$ 690 cm^{-1} [31].

To proceed further, we make several assumptions. We choose F(S_0) = 5.241 and F(S_1) = 5.285 cm^{-1} based on *ab initio* calculations. We choose $\rho_a = \cos 30°$ and $\rho_b = \cos 60°$ since the axes about which the torsional motions are occurring make angles of approximately $\pm$ 30° ($\pm$ 60°) with respect to a (b). Note that this assumption is at least qualitatively consistent with the experimental finding that $D_a \gg D_b$ in all perturbed bands. And, since the spacings between the three subbands in each band are approximately equal , we also neglect the possible influence of couplings between the two rotors. We then use Eq. (2) to evaluate the first-order perturbation coefficients $W_{01}^{(1)}$ from the observed values of D_a [21],

$$D_a = F W_{01}^{(1)} \rho_a \tag{6.2}$$

These coefficients were then used to determine V_3^* from Herschbach's tables [32]. In principle, the values of D_b also should be included in this analysis, but as these are small and much less precise, they were ignored. And, finally, the derived barrier heights were used to compute tunneling splittings that could be compared to the experiment.

Table 6.5 lists the values of V_3^* that were derived in this way. The excited state values of V_3^* are all substantially less than that of the S_0 state. The different S_1 vibrational levels have substantially different V_3^* values, varying from 117 to 342 cm^{-1}.

That the excited state values of V_3^* are all substantially less than that of the ground state in DMABN is an extremely important result. Methyl groups attached to 'tetrahedral' nitrogen atoms typically have large torsional barriers, of the order

Table 6.5: Methyl group torsional parameters in the ground and electronically excited states of DMABN.

State	Band	D_a (MHz)	D_b (MHz)	V_3^* [a] (cm^{-1})	V_3^* [b] (cm^{-1})	TS [c] (GHz)	TS [d] (GHz)
S_0	All	~ 0	~ 0	> 500	543	0	
S_1	2G	42	24	222	230	3	4
	3G	186	45	153	138	15	18
	4G	7	0	342	367	0.4	0.5
	5G	305	28	117	140	14	18
	6G	118	10	165	$180^{[e]}$		9
	7G	192	37	165	148	12	15
	8G	554	82	117	107	27	31

[a] Values from D_a obtained from the assigned fit.
[b] Values from GA automated fit.
[c] Experimental tunneling splitting in GHz.
[d] Theoretical tunneling splitting in GHz.
[e] Value from D_a, see text.

of 500 cm^{-1}. Theoretical studies suggest that these large values have their origin in a 'hyperconjugative' interaction involving the nitrogen lone pair electrons and the attached methyl group [33]. If this is so, then the substantial decrease in V_3^* values in the excited state of DMABN indicates that the density of lone pair electrons on the nitrogen atom is substantially reduced, compared to the ground state. The (six-fold) CH_3 torsional barrier in the n→3s Rydberg state of CH_3NH_2 is much smaller ($V_6 = 5$ cm^{-1}) [34] than the (three-fold) barrier in the ground state ($V_3 = 690$ cm^{-1}) [31], in accord with this thinking. Thus, the smaller values of V_3^* in the S_1 state of DMABN provide firm evidence for charge transfer from the n orbital of nitrogen atom to the π^* orbital(s) of the aromatic ring. Stark effect experiments [35] to determine the dipole moment of S_1 DMABN will provide a more quantitative measure of this effect.

Variations in the V_3^* values among the different S_1 vibrational levels probed in this work may be attributed to several factors. One is the method of fitting the data. Using jb95, we fit the individual subbands separately, obtaining different values of D_a (and D_b) from which the barrier heights were determined separately, as well. In the absence of rotor-rotor coupling, the values for the different subbands belonging to a given ν should be the same. One possible explanation for the fact that they are different is the high uncertainty in the values of D_a for the weaker subbands. Another

possible explanation is rotor-rotor coupling. To address this issue, we independently fit all of the subbands together, using the GA method. The Hamiltonian used for this procedure was the full torsion-rotation Hamiltonian, as described by Tan *et al.* [21], which requires that all torsional subbands with the same ν have the same value of V_3^*. For all bands a consistent picture was found with the exception of band 6. In that band the result from D_a and the subband separation do not follow the Hamiltonian1 [21]. Table 6.5 also lists the results of these calculations. Comparing these to experiment, we see that the values obtained by the two different methods agree quite well.

Independent of the possible variations in the V_3^* values within a given ν, the different S_1 vibrational levels of DMABN also have substantially different V_3^* values. They also have very different tunneling splittings (*cf.* Table 6.5). Substantial coupling between the methyl group torsional motion and other vibrational modes, especially these involving the DMA group, may be responsible for the differences in these values. Motion along one coordinate might strongly facilitate motion along others. Indeed, higher lying S_1 levels have lower V_3^* values, and larger tunneling splittings. The possible disappearance of the E_1+E_3 subbands at higher energy also may be attributed to interactions among these degrees of freedom. Further studies of these effects are in progress.

6.5   Summary

Summarizing, an extensive study of the electronic spectrum of DMABN at high resolution has revealed new information about the properties of the ground and excited states of the isolated molecule. Ground state DMABN is 'planar' and less pyramidal; excited (S_1) state DMABN is twisted and more pyramidal. The spectra also reveal evidence for substantial methyl group torsional activity, a consequence of substantial charge transfer from the nitrogen atom to the ring. Thus, all three vibrational coordinates: DMA torsion, DMA inversion, and methyl group torsion act in concert to 'protect' against 'back' electron transfer once the photon is absorbed. Thereby created is a stable minimum on the energy landscape of the S_1 state that is responsible for the unique emissive properties of DMABN and related molecules in the condensed phase.

References

[1] E. Lippert, W. Lüder, and H. Boos. Proceedings of the 4th international meeting on advances in molecular spectroscopy. 1959.

[2] A. Mangini. pages 443–457. Pergamon Press, Oxford, 1962.

[3] E. Lippert, W. Lüder, F. Moll, W. Nägele, H. Boos, H. Prigge, and I. Seibold-Blankenstein. Transformation of electron excitation energy. *Angew. Chemie*, 73:695–706, 1961.

[4] K. Rotkiewicz, K. H. Grellmann, and Z. R. Grabowski. Reinterpretation of the anomalous fluorescense of p-N,N-dimethylamino-benzonitrile. *Chem. Phys. Lett.*, 19:315–318, 1973.

[5] W. Rettig. Charge separation in excited states of decoupled systems - TICT compounds and implications regarding the development of new laser dyes and the primary process of vision and photosynthesis. *Angew. Chemie Int. Ed. Engl.*, 25:971–988, 1986. A comprehensive review of the early work in this field.

[6] K. A. Zachariasse, T. von der Haar, A. Hebecker, U. Leinhos, and W. Kühnle. Intramolecular charge transfer in aminobenzonitriles: requirements for dual fluorescence. *Pure Appl. Chem.*, 65:1745–1750, 1993.

[7] Z. R. Grabowski, K. Rotkiewicz, and W. Rettig. Structural changes accompanying intramolecular electron transfer: focus on twisted intramolecular charge-transfer states and structures. *Chem. Rev.*, 103:3899–4032, 2003.

[8] T. Kobayashi, M. Futakami, and O. Kajimoto. 4-(N,N-dimethylamino)benzonitrile solvated by a polar molecule: Structural demand for charge-transfer state formation. *Chem. Phys. Lett.*, 130:63–66, 1986.

[9] E. M. Gibson, A. C. Jones, and D. Phillips. 4-N,N-dimethylaminobenzonitrile: the absence of a fluorescence under jet-cooled conditions. *Chem. Phys. Lett.*, 136:454–459, 1987.

[10] J. A. Warren, E. R. Bernstein, and J. I. Seeman. Chemical reactions in isolated clusters: Excited state electron transfer in 3- and 4-dimethylaminobenzonitrile. *J. Chem. Phys.*, 88:871–878, 1988.

[11] V. H. Grassian, J. A. Warren, E. R. Bernstein, and H. V. Secor. Conformational changes upon $S_1 \leftarrow S_0$ excitation in 4-dimethylaminobenzonitrile and some of its chemical analogs. *J. Chem. Phys.*, 90:3994–3999, 1989.

[12] R. D. Gordon. Comment on: The torsional potential function of dimethylaminobenzonitrile and related compounds in their S_1 states. *J. Chem. Phys.*, 93:6908–6909, 1990.

[13] E. R. Bernstein, V. H. Grassian, and J. A. Warren. Reply to the Comment on: The torsional potential function of dimethylaminobenzonitrile and related compounds in their S_1 states. *J. Chem. Phys.*, 93:6910, 1990.

[14] O. Kajimoto, H. Yokoyama, Y. Ohshima, and Y. Endo. The structure of 4-(N,N-dimethylamino)benzonitrile and its van der Waals complexes. *Chem. Phys. Lett.*, 179:455–459, 1991.

[15] F. P. Salgado, J. Herbich, A. G. M. Kunst, and R. P. H. Rettschnick. Structure and picosecond excited-states dynamics in isolated, supercooled 4-(N,N-dimethylamino)benzonitrile. *J. Phys. Chem A*, 103:3184–3192, 1999.

[16] H. Saigusa, N. Miyakoshi, C. Mukai, T. Fukagawa, S. Kohtani, R. Nakagaki, and R. Gordon. Twisted S_1 excited state geometries in 4-dimethylaminobenzonitrile and dimethylaniline: New -d6 origin bands. *J. Chem. Phys.*, 119:5414–5422, 2003.

[17] D. Rappoport and F. Furche. Photoinduced intramolecular charge transfer in 4-(dimethyl)aminobenzonitrile - a theoretical perspectiv. *J. Am. Chem. Soc.*, 126:1277–1284, 2004.

[18] J. L. Tomer, K. W. Holtzclaw, L. H. Spangler, and D. W. Pratt. Phosphorescence excitation spectroscopy in supersonic jets. The lowest triplet state of pyrazine. *J. Chem. Phys.*, 88:1528–1538, 1988.

[19] W. A. Majewski and W. L. Meerts. Near-UV spectra with fully resolved rotational structure of naphthalene and perdeuterated naphthalene. *J. Mol. Spectrosc.*, 104:271–281, 1984.

[20] W. A. Majewski, J. F. Pfanstiel, D. F. Plusquellic, and D. W. Pratt. *Laser Techniques in Chemistry*, page 101. Wiley, New York, 1995.

[21] X. Q. Tan, D. J. Clouthier, R. H. Judge, D. F. Plusquellic, J. L. Tomer, and D. W. Pratt. Torsion-rotation interactions in a two-top molecule: High resolution $S_1 \leftarrow S_0$ electronic spectrum of 2,3-dimethylnaphthalene. *J. Chem. Phys.*, 95:7862–7871, 1991.

[22] J. A. Hageman, R. Wehrens, R. de Gelder, W. Leo Meerts, and L. M. C. Buydens. Direct determination of molecular constants from rovibronic spectra with genetic algorithms. *J. Chem. Phys.*, 113:7955–7962, 2000.

[23] W. Leo Meerts, M. Schmitt, and G. Groenenboom. New applications of the genetic algorithm for the interpretation of high resolution spectra. *Can. J. Chem.*, 82:804–819, 2004.

[24] D. F. Plusquellic, R. D. Suenram, B. Maté, J. O. Jensen, and A. C. Samuels. The conformational structures and dipole moments of ethyl sulfide in the gas phase. *J. Chem. Phys.*, 115:3057–3067, 2001.

[25] M. J. Frisch, G. W. Trucks, H. B. Schlegel, P. M. W. Gill, B. G. Johnson, M. A. Robb, J. R. Cheeseman, T. Keith, G. A. Petersson, J. A. Montgomery, K. Raghavachari, M. A. Al-Laham, V. G. Zakreqewski, J. V. Ortiz, J. B. Foresman, J. Cioslowski, B. Stefanov, A. Nanayakkara, M. Challacombe, C. Y. Peng, P. Y. Ayala, W. Chen, M. W. Wong, J. L. Andres, E. S Replogle, R. Gomperts, R. L Martin, D. J. Fox, J. S. Binkley, D. J. Defrees, J. Baker, J. P. Stewart, M. Head-Gordon, C. Gonzalez, and J. A. Pople. Gaussian 98, Revision A9, 1998.

[26] J. L. Tomer. *Electronic Spectroscopy of Large Molecules in the UV*. PhD thesis, University of Pittsburgh, 1991.

[27] B. D. Howells, J. McCombie, T. F. Palmer, J. P. Simons, and A. Walters. Laser-induced fluorescence spectroscopy and structure of microsolvated molecular clusters. part 2. laser-induced fluorescence spectroscopy of jet-cooled ethyl 4-aminobenzoate, methyl 4-aminobenzoate, 4-aminobenzonitrile and their dimethylamino and pyrrolidino derivatives. *J. Chem. Soc. Farad. Trans.*, 88:2595–2601, 1992.

[28] W. E. Sinclair and D. W. Pratt. Structure and vibrational dynamics of aniline and aniline-Ar from high resolution electronic spectroscopy in the gas phase. *J. Chem. Phys.*, 105:7942–7956, 1996.

[29] W. Leo Meerts Giel Berden, Jack van Rooy and Klaas A. Zachariasse. Rotationally resolved electronic spectroscopy of 4-aminobenzonitrile. *Chem. Phys. Letters*, 278:373, 1997.

[30] S. Jagannathan and D. W. Pratt. The fluorescence excitation spectrum of 1-naphthoic acid at rotational resolution: S_0 and S_1 potential energy surfaces along the R-COOH torsional coordinate. *J. Chem. Phys.*, 100:1874–1883, 1994.

[31] D. Kivelson. Structure of the methylamine molecule. II. Theory of internal motions and application to CD_3ND_2. *J. Chem. Phys.*, 27:353–360, 1957.

[32] D. R. Herschbach. Tables of Mathieu integrals for the internal rotation problem. *J. Chem. Phys.*, 27:975, 1957.

[33] A. E. Dorigo, D. W. Pratt, and K. N. Houk. Origin of methyl conformational preferences and rotational barriers in the ground states, excited triplet states, radical cations, and radical anions of molecules having CH_3-C=X functionalities. *J. Amer. Chem. Soc.*, 109:6591–6600, 1987.

[34] S. J. Baek, K. W. Choi, Y. S. Choi, and S. K. Kim. Spectroscopy and dynamics of methylamine. I. rotational and vibrational structures of CH_3NH_2 and CH_3ND_2 in $\tilde{A}$ states. *J. Chem. Phys.*, 118:11026–11039, 2003.

[35] T. M. Korter, D. R. Borst, C. J. Butler, and D. W. Pratt. Stark effects in gas-phase electronic spectra. Dipole moment of aniline in its excited S_1 state. *J. Amer. Chem. Soc.*, 123:96–99, 2001.

SEVEN

Introduction to nanofabrication with optical laser fields

7.1 Introduction

After the discovery of lasers it was noticed that lasers tuned close to atomic resonances can transfer a significant amount of momentum to the motion of atoms. This effect allowed for optical manipulation of atoms and evolved into many fascinating branches of science, like for example high-precision atomic spectroscopy, atomic clocks, laser cooling, trapping, Bose-Einstein condensation and many others. These techniques brought a detailed understanding of the nature of the interactions between laser radiation and atoms, sometimes called atom-optics.

In 1987 Balykin and Letokhov in their theoretical paper [1] suggested for the first time that atom-optics could be applied to focus atoms into a nanometer spot size by a focused hollow 'doughnut-mode' (TEM_{01}^*) laser beam. This was never realized experimentally, but Timp *et al.* [2] replaced the idea of a TEM_{01}^* 'laser lens' with the focused standing-wave (SW) concept. The principles of laser-focused nanofabrication, for the first time performed by Timp *et al.* are shown in Fig. 7.1. An atomic beam of sodium is formed by evaporating atoms into a vacuum. Then, the beam is collimated in the transversal direction by means of laser cooling and subsequently it passes a focused SW laser beam, tuned near to the sodium resonance around $\lambda_{vac.} = 589.16$ nm (a vacuum wavelength). The atoms experience a force due to the varying intensity in the SW and are focused by an array of nanolenses (SW nodes or antinodes). A substrate is placed, such that the SW grazes across its surface. In this way, the first laser-focused fabrication of extremely parallel sodium nanolines, spaced by just $\lambda/2 = 295$ nm was realized.

The first nanostructure grown with atoms stable at ambient atmosphere were carried out by McClelland *et al.* [3], who succeeded to focus chromium and demon-
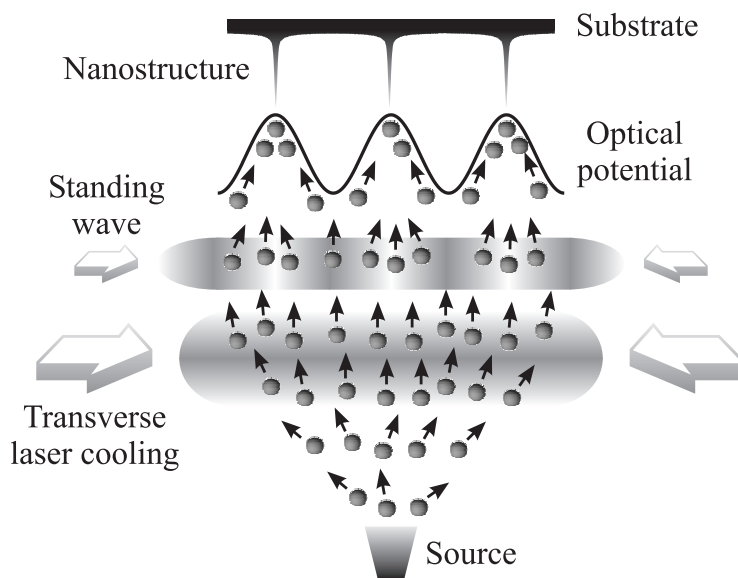
Figure 7.1: Principles of laser-focused atomic deposition.

strated the grown structures by atomic force microscopy (AFM). Afterwards, the field 'exploded' with many other examples of laser-focused structures. Manipulation of atoms in a laser SW and subsequent fabrication of nanostructures was experimentally demonstrated in the direct deposition regime with atomic beams of aluminum [4], ytterbium [5], iron [6, 7] and via lithography with a self-assembled monolayer as the resist with cesium [8]. A number of different SW geometries were used: a one-dimensional SW created from two counter-propagating laser beams resulted in periodic nanolines [2–8]; a SW composed of four laser beams at right angles yielded a square lattice of nanostructures [9] and a SW obtained by three laser beams crossing at mutual angles of 120° resulted in a hexagonal nanostructured array [10]. More complicated periodic patterns were created with more complex laser fields, such as those obtained by polarization gradients [11, 12], by reflecting a laser beam from a holographic mirror [13], by utilizing a slight misalignment of four initially orthogonal laser beams [14], by beating of two atomic resonances [15] and by superimposing five laser beams to create a quasicrystal pattern [16].

The following section briefly introduces the interactions between light and atoms, which make the laser-focused manipulation of atoms possible. In the experimental section the apparatus used in our experiments with chromium and iron is presented. The last two chapters of this thesis describe our own contributions to the laser-focused
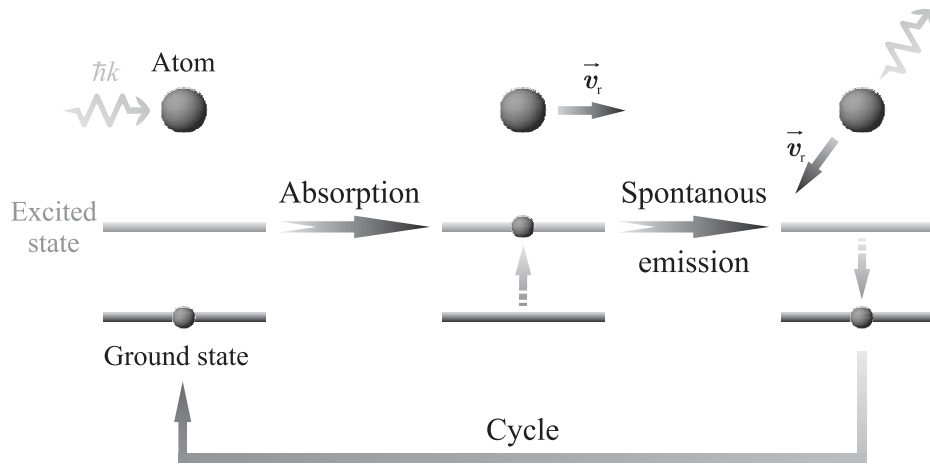
Figure 7.2: A simple mechanistic model of the spontaneous force, employed in the laser cooling or heating processes. $\vec{v}_\mathrm{r}$ denotes the recoil velocity.

experiments: quasiperiodic chromium structures and iron nanolines.

7.2 Optical forces on atoms

7.2.1 Spontaneous force and laser cooling

There are basically two types of the optical forces that can act on an atom. The first one is usually called the spontaneous force. It is the dominant force for laser frequencies tuned within the linewidth of the atomic transition. Its origin is schematically shown in Fig. 7.2. The near-resonant photon from the laser field is absorbed by a 'two-level' atom and therefore gains recoil momentum in the direction of the laser radiation. Within the lifetime τ of the excited state, the atom emits isotropically a photon, assuming that the spontaneous decay is dominant. The net effect of absorption and emission is that the atom gains momentum in the direction of the laser propagation. Since the spontaneous force is non-conservative, it can accelerate (heat) or decelerate (cool) the atoms. However, in order for this process to have a macroscopic effect on the velocity of the atoms, the absorption-emission cycle has to be repeated many times ($\sim 10^4$). This requires a closed transition.

In a simple two level picture we will now demonstrate the behaviour and magnitude of this force. For a laser beam with wave vector $k = 2\pi/\lambda$, tuned close to an atomic

resonance, the average spontaneous force can be expressed as [17, 18]:

$$< F_s >= \hbar k \Gamma f_e, \qquad (7.1)$$

where f_e is the average fraction of atoms in the excited state

$$f_e = \frac{I}{2I_s} \frac{1}{1 + I/I_s + (2\Delta/\Gamma)^2}. \qquad (7.2)$$

In these equations, I is the laser intensity, Δ is the laser detuning from the atomic resonance, Γ is the natural linewidth of the transition ($\Gamma = 1/\tau$) and I_s is the saturation intensity of the transition

$$I_s = \frac{\pi h c \Gamma}{3\lambda^3}. \qquad (7.3)$$

It is clear from these equations that the spontaneous force saturates with increasing laser intensity I and decreasing detuning Δ ($f_e \longmapsto 0.5$). Furthermore, for large detuning the force is proportional to I/Δ^2 and therefore rapidly vanishes. To illustrate the magnitude of this force, we take as an example the transition $^7P_4^o \leftarrow {}^7S_3$ in ^{52}Cr at $\lambda_{vac.} = 425.55$ nm. The transition is almost fully saturated ($f_e = 0.455$) for $I = I_s = 85$ mW/cm^2 and $\Delta = 0$. For these conditions the spontaneous force corresponds to an acceleration of 2.6×10^5 m/s $= 26000 \times g$, with g the earth's gravitational acceleration. Moreover, this example shows that one does not need high laser intensities to saturate the spontaneous force, at least for small detunings comparing to Γ.

One of the most important applications of the spontaneous force is laser cooling of a cloud of atoms [19, 20]. If the laser frequency is tuned below the atomic resonance, a so-called Doppler cooling occurs [21]. The red-shifted photons are absorbed by atoms with a velocity component towards the direction of the laser beam and subsequently these atoms reradiate the photons isotropically. Therefore, the atoms moving towards the laser source are slowed down. The laser field 'appears' to an atom as a viscous medium, sometimes called 'optical molasses' [22]. In a field of three pairs of counter-propagating beams along the x, y and z-axis a cloud of atoms can be slowed down and even trapped. The temperature reachable by the Doppler cooling is limited by the spontaneous emission. The minimum temperature T_D is given by [23]

$$T_D = \hbar\Gamma/(2k_B). \qquad (7.4)$$

In the example of the ^{52}Cr transition $^7P_4^o \leftarrow {}^7S_3$, $T_D = 120$ μK.

With other techniques the atoms can be cooled beyond the Doppler limit. For example with polarization gradient cooling (also called Sisyphus cooling) [17, 24], velocity-selective coherent population trapping (VSCPT) [25] and Raman cooling. Using this last technique a beam of sodium atoms was cooled to temperatures as low as 100 nK [26].

In the laser-focused nanofabrication transversal laser cooling is used to collimate the atomic beam without loss in flux (see Fig. 7.1).
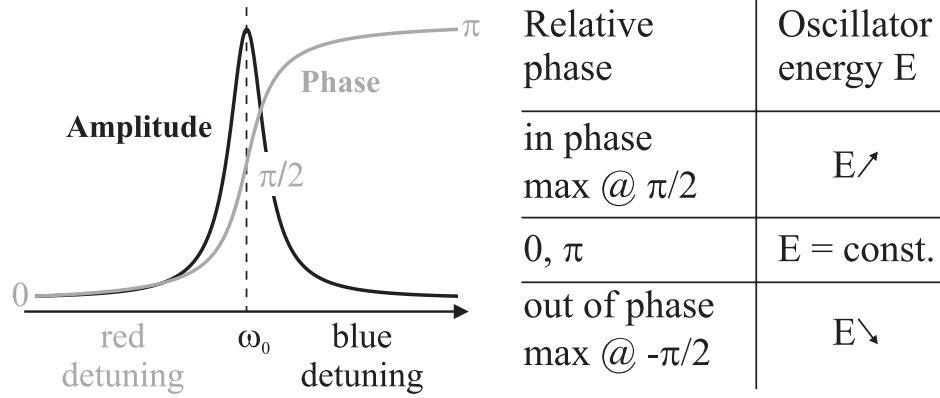
Figure 7.3: A harmonic oscillator in an external field. Illustration of the dipole force.

7.2.2   Dipole force and laser focusing

The second type of force acting on an atom in an intense, near-resonant laser field exhibiting spatial gradients (like in a SW), is often referred to as dipole force. If the atom interacts with the optical field oscillating with frequency ω, tuned close to the atomic resonance ω_0, the field induces an oscillating dipole moment in the atom. This induced dipole moment behaves like a harmonic oscillator driven by an external force (see Fig. 7.3). Therefore, it oscillates in phase with the driving frequency, if $\omega < \omega_0$ or out of phase if $\omega > \omega_0$. Because of the intensity gradient this atom-field interaction leads to a non-vanishing, time averaged potential, which governs the motion of the atom. For negative detuning $\Delta = \omega - \omega_0 < 0$, the resulting force pulls the atoms towards the intensity maxima, while for positive detuning $\Delta > 0$, the atoms are pushed to the intensity minima.

The dipole force is entirely conservative and can be properly described by the fully quantum-mechanical, dressed atom approach [27]. However, to illustrate its magnitude we use here a semiclassical model. In this approximation the averaged potential V_d of the atom-field interaction can be expressed as [17, 18]

$$V_d = \frac{\hbar\Delta}{2} \ln\left(1 + \frac{I/I_s}{1 + 4\Delta^2/\Gamma^2}\right), \tag{7.5}$$

which reduces in the limit of large detunings to

$$V_d = \frac{\hbar\Gamma^2}{8\Delta} \frac{I}{I_s} \tag{7.6}$$

and

$$F_d = -\nabla V_d. \tag{7.7}$$

The important properties of the force are:

- it does not saturate with the laser intensity I;

- it is limited only by the achievable laser intensity and the steepness of this intensity gradient;

- concerning detuning, the force has an extremum (because $V_d(\Delta = 0) = 0$ and $V_d(\Delta \longmapsto \infty) \longmapsto 0$), which can be pushed towards larger detunings by increasing the laser intensity;

- for large detunings, the force is proportional to the ratio I/Δ.

As an example we take the laser SW with frequency again tuned close to the $^7P_4^o \leftarrow {}^7S_3$ transition in ^{52}Cr, and estimate the acceleration acquired by the chromium atoms. We use the following experimental parameters: detuning $\Delta = 2\pi \times 200$ MHz and the laser intensity $I = 1000 \times I_s$ (because of the focusing of the SW laser beam). This results in a quite substantial acceleration of 1.8×10^7 m/s $= 1.8 \times 10^6 \times g$.

The ratio between dipole and spontaneous forces plays an important role in the different parts of the laser-focused nanofabrication experiments. For the transversal cooling step the spontaneous force must be dominant, while for the 'structure writing' it is the dipole force. From the presented equations and examples, it follows that the experimental parameters can be chosen such that for $\Delta \lesssim \Gamma$ and not too strong laser intensities, the spontaneous force dominates, while for $\Delta \gg \Gamma$ and high laser intensities, the dipole force governs the motion of atoms.

7.2.3   Real atoms and their interaction with light

Unfortunately, in general atoms are no two-level systems. Because of the selection rules an atomic transition always involves at least one state with angular momentum $J > 0$. Chromium and iron, used in the experiments presented in this thesis have a non-zero angular momentum in the ground and excited states. From this it follows that at oven temperatures $T \sim 1800$ °C not only the lowest J-level is populated. For example, the iron ^{56}Fe ground term ^5D has five sublevels $J = 4, 3, 2, 1, 0$, with $J = 4$ being the lowest in energy. At a temperature of $T = 1800$ °C their population is as follows: 46.3%, 27.0%, 15.8%, 8.3%, 2.6% (starting from the highest J). This implies that in the experiment, we initially loose more than half of the ^{56}Fe atoms, because they do not interact with the laser field.

Levels with $J \neq 0$, posses a magnetic sublevel structure, which is degenerated in zero magnetic field. For the iron ^{56}Fe ground state $^5D_4$, this results in splitting of this level into nine Zeeman sublevels with $|m_J| \leqslant 4$, even in the presence of the weak Earth's magnetic field ($B \sim 100 \ \mu$T) . The excited state $^5F_5^o$, splits into 11 sublevels $|m_J| \leqslant 5$. The energy difference between neighbouring sublevels equals to

$g_J \mu_B B$ and for $B = 100$ μT corresponds to 2.10 MHz and 1.96 MHz in the ground and excited states, respectively. Owing to this effect the transition $^5F_5^o \leftarrow ^5D_4$ splits into five transitions (selection rules $\Delta m_J = \pm 1, 0$): three starting from the ground state each m_J-sublevel and ending in the excited state $m_J - 1$, m_J, $m_J + 1$-sublevels, spaced by 1.96 MHz and two starting from the sublevels $m_J - 1$, $m_J + 1$ and ending at m_J-sublevel spaced by 2×2.10 MHz. It is obvious that even the weak Earth's magnetic field significantly complicates the laser cooling utilizing this transition.

Unfortunately, there are more problems caused by the magnetic sublevel structure. One originates from the fact that transition probabilities (Clebsch-Gordan coefficients [28]) are different between different m_J-sublevels. Additionally, these transition probabilities are dependent on the polarization of the light. For example if the quantization axis is along the incident direction of the laser light, the σ^+ polarized light will only induce transitions $\Delta m_J = 1$. This may also lead to the optical pumping of sublevels with the polarized laser light, because the induced transitions are polarization dependent, while the spontaneous emission is not. Another problem arises if the magnetic field is not oriented along the quantization axis. This results in a precession of the angular momentum and a time varying sublevel population, which again affect the experiment.

Closely spaced hyperfine levels might also complicate the atom-light interactions. Fortunately, the most abundant isotopes of both ^{52}Cr and ^{56}Fe used in our experiments have the nuclear spin I = 0 and therefore no hyperfine sublevels. However, this was an issue in for example the experiment with ^{23}Na [2] (I = 3/2).

For a more detailed and elaborate treatment of these topics we refer to the nanotechnology reviews and books [19, 27, 29–31].

7.3   Experimental Setup

7.3.1   Laser part

The experimental setup is presented in Fig. 7.4 and is described in details by E. Jurdik [32]. Here, we shortly discuss its main components. The pump laser is a diode-pumped, frequency-doubled Nd:YVO$_4$ laser (Spectra Physics Millennia X), which produces up to 10.5 W output power at 532 nm. It pumps the narrow-band, FWHM $\sim$ 600 kHz [33], Ti:Sapphire laser (Coherent 899-21). The frequency of this laser can be tuned by 30 GHz in the infra-red. The intensity of the infra-red is typically $1.3 - 1.5$ W at $\lambda_f^{air} = 850.872$ nm and $\lambda_f^{air} = 743.994$ nm, the fundamental wavelengths needed for chromium and iron, respectively. Small parts of this beam are utilized to monitor its frequency stability and wavelength. The wavemeter, similar to the one described in Ref. [34], serves for a determination of the fundamental beam wavelength to ± 1 pm.

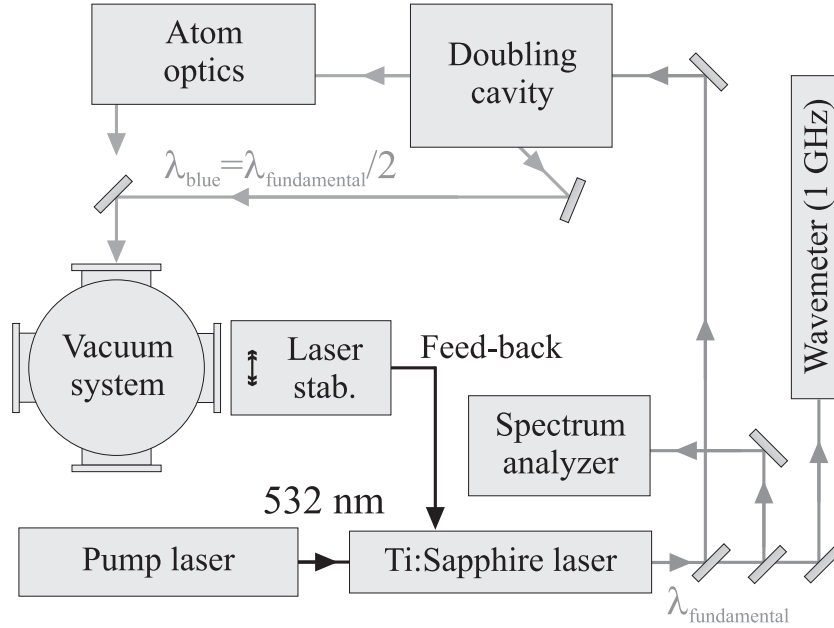The infra-red frequency is doubled in the external enhancement resonator with

Figure 7.4: The scheme of the experimental setup used for laser manipulation of chromium and iron.

a type I, critically phase-matched LBO crystal. The generation of the blue light at $\lambda_b^{air} = 425.434$ nm with this doubling cavity was described in details by E. Jurdik *et al.* [33]. For experiments with iron we replaced the mirrors and doubling crystal to $\lambda_{UV}^{air} = 371.994$ nm, corresponding to the $^5F_5^o \leftarrow {}^5D_4$ ^{56}Fe transition. The typically obtained UV powers are on the order of 400 mW behind the output coupler. The best ever achieved total power was 500 mW (sum of two UV reflections and output coupler losses) and was obtained with a fundamental power of 1.5 W, resulting in an SHG conversion efficiency $\eta = 33\%$.

The stronger blue (UV) reflection from the LBO crystal leaves the cavity from the side and is directed towards the vacuum system. This radiation is utilized for the stabilization of the Ti:Sappire laser to the atomic transition. This is done by a split-photodiode technique [35] with principles depicted in Fig. 7.5 (a). The laser induced fluorescence (LIF) from a divergent atomic beam is imaged onto a split-photodiode (see Fig. 7.5 (a)). The difference signal between the two parts of the split-photodiode results in a dispersion curve similar to the one presented in Fig. 7.5 (b). Due to the spread in the transversal atomic velocities (Doppler effect) the fluorescent spot moves across the atomic beam, if the laser frequency is scanned (see Fig. 7.5 (b)).
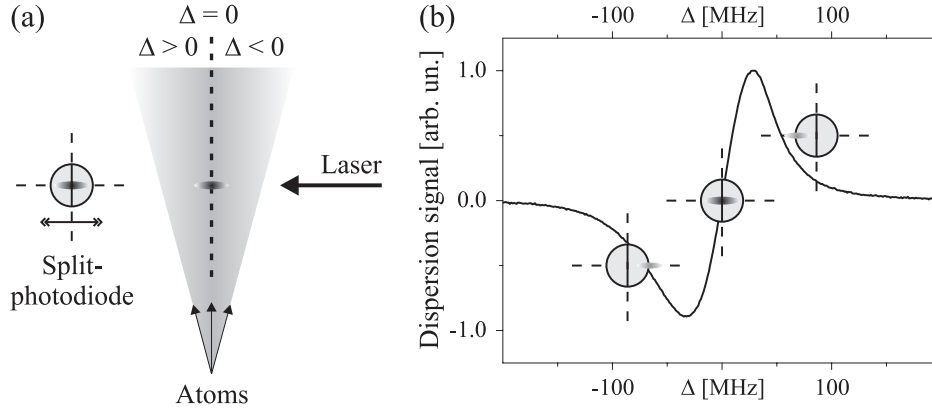
Figure 7.5: (a) The principles of the split-photodiode technique. (b) Experimentally obtained dispersion signal from a divergent iron beam. The positions of the fluorescent spot relative to the split-photodiode are depicted at the corresponding parts of the dispersion curve.

The split-photodiode is mounted on a micro-translator, which allows for a total travel of 16 mm with resolution of ± 4 μm. As described in [32] this facilitates a tuning of the laser frequency by ± 100 MHz around the atomic resonance with a resolution of ~ 100 kHz.

The main blue beam enters the atom optics section, where it is shaped and polarized as needed for the experiments. At first, the beam is split into cooling and focusing parts with the combination of a $\lambda/2$-plate and a polarization beam-splitter. This allows for an easy power ratio adjustment in both beams. The cooling beam passes another $\lambda/2$-plate, which sets the polarization required for the lin $\perp$ lin polarization gradients cooling scheme [17, 36]. The beam is expanded by a cylindrical beam expander, typically to a $1/e^2$ intensity full widths of 25×3 mm (height $\times$ width) and is directed towards the vacuum chamber.

The focusing beam is shifted in frequency by an acousto-optic modulator (AOM), optimized for operation at ± 200 MHz. The AOM is mounted on an xyz translation stage with two angular degrees of freedom. Behind the AOM the first order diffracted beam is chosen with a diaphragm, recollimated and send to the vacuum chamber. Before entering the vacuum the beam is focused by a lens to a $1/e^2$ intensity full widths of $60 - 200$ μm, with the focal point on the retro-mirror (Fig. 7.6 (b)).
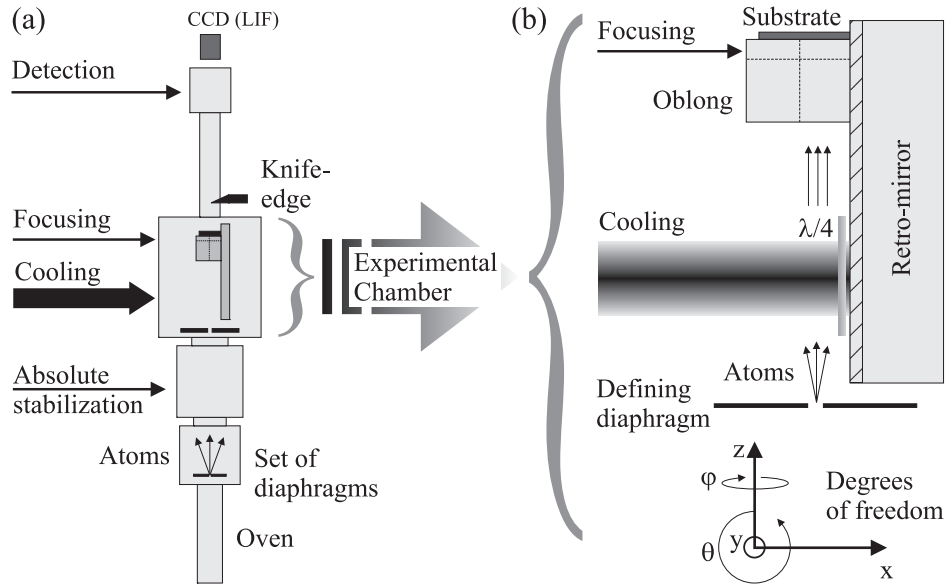
Figure 7.6: The vacuum part of the experimental setup used for growing laser-focused chromium and iron nanostructures. (a) Overall view. (b) Zoom in to the experimental chamber with shown degrees of freedom.

7.3.2   Vacuum part

The vacuum system is vertical (see Fig. 7.6 (a)) and is rigidly mounted on an optical table. The thermal atomic beam of chromium or iron atoms is evaporated from a high temperature effusion cell held at $1700 - 1875$ °C. The beam is precollimated by a set of diaphragms and enters the stabilization chamber, where it crosses the laser stabilization beam. Subsequently, the atomic beam passes the experimental chamber, which is presented in more details in Fig. 7.6 (b). Here, it is again mechanically collimated by a diaphragm with an opening of 1.5×1.5 mm. This chamber is the heart of the vacuum system and contains the *in vacuo* optics for the alignment of the cooling and focusing beams and the substrate position.

We describe here only the one-dimensional experiment resulting in the laser-focused nanolines. The unit utilized for the two-dimensional quasiperiodic structures is presented in Chapter 8. The unit has all three translational and two angular degrees of freedom. A glass oblong, cut from a prism with the right angle specified to within ± 15 μrad, serves as a sample holder. The high quality optical faces of the oblong are used as the reference for the angular adjustment of the sample with respect to the mirror. The sample is clamped to the top of the oblong. There are two

grooves cut in the oblong, vertical for the atomic beam and horizontal for the focusing beam. The focusing SW is created by reflecting the beam from the retro-mirror. The lin $\perp$ lin Sisyphus cooling scheme is applied by reflecting the cooling beam from the retro-mirror and passing twice a $\lambda/4$-plate.

To optimize the alignment of the cooling and focusing beams, the stabilization laser beam, which has passed the vacuum stabilization chamber is directed to the top of the vacuum system. There, it images the LIF from the atomic beam effected by the cooling and focusing beams onto a CCD camera. After the cooling and focusing effects are maximized, the divergence of the atomic beam can be measured utilizing the knife-edge technique [37]. Finally, the substrate can be slid in the atomic beam and nanolines with a period of $\lambda/2$ are grown.

7.4   Chromium and iron properties

In this section we summarize the most important properties of chromium and iron, the elements we used in our laser-focused nanofabrication experiments. The properties are presented in Table 7.1 [38], together with the energy diagrams for ^{52}Cr in Fig. 7.7 and ^{56}Fe in Fig. 7.8 (based on the data from Ref. [39]).
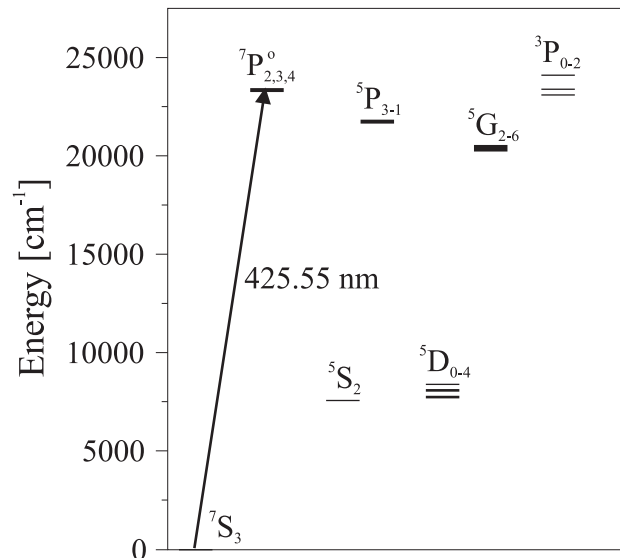
Figure 7.7: ^{52}Cr energy diagram.

Table 7.1: Selected properties of chromium and iron.

Property	Chromium	Iron
Atomic number	24	26
Electronic ground state config.	$[^{18}\text{Ar}]\ 4s^1, 3d^5$	$[^{18}\text{Ar}]\ 4s^2, 3d^6$
& the corresponding term	$^7S_3$	$^5D_4$
Atomic weight [amu]	51.9961(6)	55.845(2)
Naturally occurring isotopes	^{50}Cr: 4.34%, I $= 0$	^{54}Fe: 5.84%, I $= 0$
& their abundance	^{52}Cr: 83.79%, I $= 0$	^{56}Fe: 91.75%, I $= 0$
& nuclear spin I	^{53}Cr: 9.50%, I $= 3/2$	^{57}Fe: 2.12%, I $= 1/2$
	^{54}Cr: 2.37%, I $= 0$	^{58}Fe: 0.28%, I $= 0$
Cooling & focusing transition	$^7P_4^o \leftarrow {}^7S_3$	$^5F_5^o \leftarrow {}^5D_4$
@ $\lambda_{vac.}$ [nm]	429.09228	372.09927
Natural linewidth $\Gamma/2\pi$ [MHz]	5.0	2.6
Saturation intensity I_s [W/m^2]	85	65
Main cooling leaks & their rate	$^7P_4^o \rightarrow {}^5D_3$, $1:5267$	$^5F_5^o \rightarrow {}^5F_5$, $1:295$
	$^7P_4^o \rightarrow {}^5D_4$	$^5F_5^o \rightarrow {}^5F_4$, $1:1421$
Melting point [°C]	1907	1538
Boiling point [°C]	2671	2861
T [°C] @ 1 Torr vapour press.	1737	1857
Crystal structure	bcc	bcc
Cell parameter [Å]	2.91	2.87
Density of solid [kg/m^3]	7140	7874
Atomic magnetic moment [μ_B]	6	4
Magnetic moment in bulk [μ_B]	0.6	2.2
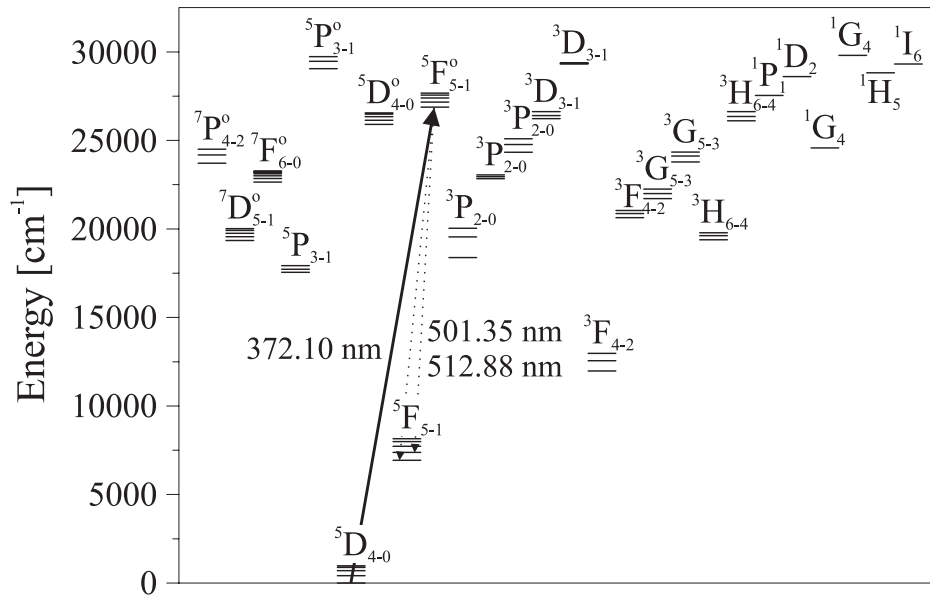
Figure 7.8: ^{56}Fe energy diagram. Transition $^5D_4 \rightarrow^5 F_5^o$ used for cooling and focusing is depicted with continuous line. The main cooling leaks are drawn with dotted lines: $^5F_5 \leftarrow^5 F_5^o$ and $^5F_4 \leftarrow^5 F_5^o$.

References

[1] V.I. Balykin and V.S. Letokhov. The possibility of deep laser focusing of an atomic beam into the Å-region. *Opt. Comm.*, 64:151–156, 1987.

[2] G. Timp and R. E. Behringer and D. M. Tennant and J. E. Cunningham and M. Prentiss and K. K. Berggren. Using light as a lens for submicron, neutral-atom lithography. *Phys. Rev. Lett.*, 69:1636–1639, 1992.

[3] J.J. McClelland and R.E. Scholten and E.C. Palm and R.J. Celotta. Laser-focused atomic deposition. *Science*, 262:877–880, 1993.

[4] R.W. McGowan and D.M. Giltner and S.A. Lee. Light force cooling, focusing, and nanometer-scale deposition of aluminum atoms. *Opt. Lett.*, 20:2535–2537, 1995.

[5] R. Ohmukai, S. Urabe, and M. Watanabe. Atom lithography with ytterbium beam. *Appl. Phys. B*, 77:415–419, 2003.

[6] G. Myszkiewicz, A. J. Toonen, A. F. van Etteger, O. I. Shklyarevskii, W. L. Meerts, Th. Rasing, J. Hohlfeld, and E. Jurdik. Laser manipulation of iron for nanofabrication. *Appl. Phys. Lett.*, 85:3842–3844, 2004.

[7] E. te Sligte, B. Smeets, K.M.R. van der Stam, R.W. Herfst, P. van der Straten, H.C.W. Beijerinck, and K.A.H. van Leeuwen. Atom lithography of Fe. *Appl. Phys. Lett.*, 85:4493–4495, 2004.

[8] F. Lison and H.-J. Adams and D. Haubrich and M. Kreis and S. Nowak and D. Meschede. Nanoscale atomic lithography with a cesium atom beam. *Appl. Phys. B*, 65:419–421, 1997.

[9] R. Gupta and J.J. McClelland and Z.J. Jabbour and R.J. Celotta. Nanofabrication of a two-dimensional array using laser-focused atomic deposition. *Appl. Phys. Lett.*, 67:1378–1380, 1995.

[10] U. Drodofsky and J. Stuhler and Th. Schulze and M. Drewsen and B. Brezger and T. Pfau and J. Mlynek. Hexagonal nanostructures generated by light mask for neutral atoms. *Appl. Phys. B*, 65:755–759, 1997.

[11] R. Gupta and J.J. McClelland and P. Marte and R.J. Celotta. Raman-induced avoided crossings in adiabatic optical potentials: Observation of $\lambda/8$ spatial frequency in the distribution of atoms. *Phys. Rev. Lett.*, 76:4689–4692, 1996.

[12] B. Brezger and Th. Schulze and P.O. Schmidt and R. Mertens and T. Pfau and J. Mlynek. Polarization gradient light masks in atom lithography. *Europhys. Lett.*, 46:148–153, 1999.

[13] M. Mützel and S. Tandler and D. Haubrich and D. Meschede and K. Peithmann and M. Flasphöhler and K. Buse. Atom lithography with a holographic light mask. *Phys. Rev. Lett.*, 88:083601, 2002.

[14] Th. Schulze and B. Brezger and R. Mertens and M. Pivk and T. Pfau and J. Mlynek. Writing a superlattice with light forces. *Appl. Phys. B*, 70:671–674, 2000.

[15] E. Jurdik and J. Hohlfeld and H. van Kempen and Th. Rasing and J.J. McClelland. Laser-focused nanofabrication: Beating of two atomic resonances. *Appl. Phys. Lett.*, 80:4443–4445, 2002.

[16] E. Jurdik, G. Myszkiewicz, J. Hohlfeld, A. Tsukamoto, A.J. Toonen, A.F. van Etteger, J. Gerritsen, J. Hermsen, S. Goldbach-Aschemann, W.L. Meerts, H. van

Kempen, and Th. Rasing. Quasiperiodic structures via atom-optical nanofabrication. *Phys. Rev. B*, 69:201102 R, 2004.

[17] J. Dalibard and C. Cohen-Tannoudji. Laser cooling below the Doppler limit by polarization gradients: simple theoretical models. *J. Opt. Soc. Am. B*, 6:2023–2045, 1989.

[18] J.P. Gordon and A. Ashkin. Motion of atoms in a radiation trap. *Phys. Rev. A*, 21:1606–1617, 1980.

[19] H.J. Metcalf and P. van der Straten. *Laser Cooling and Trapping.* Springer, New York, 1999.

[20] P.D. Lett, W.D. Phillips, S.L. Rolston, C.E. Tanner, R.N. Watts, and C.I. Westbrook. Optical molasses. *J. Opt. Soc. Am. B*, 6:2084–2107, 1989.

[21] T. Hänsch and A. Schawlow. Cooling of gases by laser radiation. *Opt. Commun.*, 13:68–69, 1975.

[22] S. Chu and L. Hollberg and J.E. Bjorkholm and A. Cable and A. Ashkin. Three-dimensional viscous confinement and cooling of atoms by resonance radiation pressure. *Phys. Rev. Lett.*, 55:48–51, 1985.

[23] C. Cohen-Tannoudji and W.D. Phillips. New mechanisms for laser cooling. *Physics Today*, 43:33–40, 1990.

[24] P.D. Lett and R.N. Watts and C.I. Westbrook and W.D. Phillips and P.L. Gould and H.J. Metcalf. Observation of atoms laser cooled below the Doppler limit. *Phys. Rev. Lett.*, 61:169–172, 1988.

[25] A. Aspect and E. Arimondo and R. Kaiser and N. Vansteenkiste and C. Cohen-Tannoudji. Laser cooling below the one-photon recoil energy by velocity-selective coherent population trapping. *Phys. Rev. Lett.*, 61:826–829, 1988.

[26] M. Kasevich and S. Chu. Laser cooling below a photon recoil with three level atoms. *Phys. Rev. Lett.*, 69:1741–1744, 1992.

[27] C. Cohen-Tannoudji J. Dupont-Roc and G. Grynberg. *Atom-Photon Interactions.* Wiley, New York, 1992.

[28] A.R. Edmonds. *Angular Momentum in Quantum Mechanics.* Princeton University Press, Princeton, 1960.

[29] J. J. McClelland. *Handbook of Nanostructured Materials and Nanotechnology*, pages 335–385. Academic Press, San Diego, CA, 2000.

[30] D. Meschede and H. Metcalf. Atomic nanofabrication: atomic deposition and lithography by laser and magnetic forces. *J. Phys. D*, 36:R17–R38, 2003.

[31] V.G. Minogin and V.S. Letokhov. *Laser Light Pressure on Atoms.* Gordon and Breach, New York, 1987.

[32] E. Jurdik. *Laser manipulation of atoms and nanofabrication.* PhD thesis, Katholieke Universiteit Nijmegen, 2001.

[33] E. Jurdik, J. Hohlfeld, A.F. van Etteger, A.J. Toonen, W.L. Meerts, H. van Kempen, and Th. Rasing. Performance optimization of an external enhancement resonator for optical second-harmonic generation. *J. Opt. Soc. Am. B*, 19:1660, 2002.

[34] P.J. Fox and R.E. Scholten and M.R. Walkiewicz and R.E. Drullinger. A reliable, compact, and low-cost Michelson wavemeter for laser wavelength measurements. *Am. J. Phys.*, 67:624–630, 1999.

[35] W.R. Anderson and C.C. Bradley and J.J. McClelland and R.J. Celotta. Minimizing feature width in atom optically fabricated nanostructures. *Phys. Rev. A*, 59:2476–2485, 1999.

[36] P.J. Ungar and D.S. Weiss and E. Riis and S. Chu. Optical molasses and multi-level atoms: theory. *J. Opt. Soc. Am. B*, 6:2058–2071, 1989.

[37] R.E. Scholten and R. Gupta and J.J. McClelland and R.J. Celotta. Laser collimation of a chromium beam. *Phys. Rev. A*, 55:1331–1338, 1997.

[38] M. Winter. WebElements Periodic Table: the periodic table on the World-Wide Web. http://www.webelements.com.

[39] National Institute of Standards and Technology. NIST Atomic Spectra Database. http://physics.nist.gov/AtData/display.ksh.

Quasiperiodic structures via atom-optical nanofabrication [1]

Abstract

We deposit a laser-collimated chromium beam onto a substrate through a quasiperiodic laser standing-wave (SW) tuned above the atomic resonance at the ^{52}Cr transition $^7S_3 \rightarrow {}^7P_4^\circ$ at 425.55 nm. This SW is created by interference of five laser beams crossing in one point at mutual angles of 72°. The resulting chromium pattern on the substrate surface mimics the geometry of the SW and it is thus itself quasiperiodic. On a surface area of $0.2{\times}0.2$ mm^2 the spatial Fourier spectrum of the measured patterns is decagonal. Besides being of fundamental interest, this quasiperiodic nanofabrication via atom optics can find its applications in photonics.

8.1 Introduction

In the past decade there has been a great deal of research devoted to photonic crystals, mainly owing to their potential applications in information and communication technology. The structure of these materials is characterized by a high degree of order (periodicity or quasiperiodicity) and is designed such as to manipulate the propagation of light in a desired way. The most common approach to the fabrication of photonic crystals relies on a periodic modulation of the refractive index with periods on the order of the wavelength of light. In this scenario a complete (non-directional and for any polarization) photonic bandgap (PBG) can be achieved only when the contrast of the refractive index becomes large. Consequently, the number of materials

(from which a complete PBG can be made) is limited to those with a large refractive index, resulting in reduced optical transparency of devices. It was demonstrated that another approach, which is based on quasiperiodic ordering of photonic crystals, can overcome these difficulties as it allows for fabrication of structures with a complete PBG even from materials with low refractive index [1]. It is this latter concept to fabrication of photonic crystals that motivated us to carry out atom-optical deposition of quasiperiodic structures.

Atom optics – a technique to manipulate atomic trajectories by the use of electromagnetic fields – can be applied to patterning of substrates or doping of materials with submicron structures. The main advantages of atom-optical fabrication are its compatibility with molecular beam epitaxy (textiti.e., the structure growth takes place *in vacuo* with no need for additional physical or chemical processing), its massiveness (textiti.e., a large surface area, in principle limited by the size of the atomic beam only, is patterned during one deposition run) and the unprecedented coherence of the deposition process [2, 3]. To date, one of the most efficient methods applied to atom-optical structuring is laser-focused atomic deposition. This approach relies on interaction of atoms, prior to their deposition onto a substrate, with a far-off-resonant laser beam that exhibits gradients in the light intensity. In order to obtain gradients on a sub-wavelength scale, two or more laser beams can be allowed to interfere and thus to create a laser standing-wave (SW). Atoms, when they cross the laser SW, experience a spatially varying optical potential that, in the first approximation, follows the SW intensity profile [4]. When the laser frequency is tuned above an atomic resonance, the atomic beam is focused in each of the nodes of the SW. In contrast, negative detunings cause the atoms to gather in the regions of high light intensities. A substrate is then placed into the modulated atomic beam and sub-wavelength structures are grown.

Manipulation of atoms in a laser SW and subsequent fabrication of nanostructures was experimentally demonstrated in the direct deposition regime with atomic beams of sodium [5], chromium [6] and aluminum [7], and via lithography with a self-assembled monolayer as the resist with cesium [8]. A number of different SW geometries were used: a onedimensional SW created from two counter-propagating laser beams resulted in periodic nanolines [5–8]; a SW composed of four laser beams at right angles resulted in a square lattice of nanostructures [9]; and a SW obtained by three laser beams crossing at mutual angles of 120° resulted in a hexagonal nanostructured array [10]. More complicated periodic patterns were written by using more complex laser fields, such as those obtained by making use of polarization gradients [11, 12], by reflecting a laser beam from a holographic mirror [13], by utilizing a slight misalignment of four initially orthogonal laser beams [14] or by beating of two atomic resonances [3]. All nanostructures fabricated via atom optics so far exhibited "allowed" symmetries, videlicet two-, four- and six-fold symmetries [15].

In this paper, we extend the technique of laser-focused atomic deposition to a quasiperiodic geometry. Five laser beams crossing at mutual angles of 72° are em-

ployed to create the SW. A chromium atomic beam is used and the SW laser frequency is tuned above the ^{52}Cr transition $^7S_3 \rightarrow {^7P_4^\circ}$ at 425.55 nm. The optical potential exhibits a "forbidden" ten-fold symmetry as does also the surface structure. The absence of translational symmetry and a noncrystallographic orientational order, that is associated with the decaganal symmetry axis, result in a structure with striking geometry and with potentially intriguing optical properties.

8.2 Calculation of laser-focused chromium structures

Prior to carrying out the experiment, we performed numerical calculations of the atomic flux distribution in a quasiperiodic optical potential. In Fig. 8.1(a) the optical intensity, $I(\mathbf{r})$, at the center of a Gaussian laser SW is shown. In the first approximation, the optical potential, $U(\mathbf{r})$, is proportional to $I(\mathbf{r})$ [4],

$$U(\mathbf{r}) = \frac{\hbar\Gamma^2}{8\Delta} \frac{I(\mathbf{r})}{I_S}. \tag{8.1}$$

Here, $\hbar$ is Planck's constant divided by 2π, $\Gamma/2\pi = 5$ MHz is the natural linewidth of the $^7S_3 \rightarrow {^7P_4^\circ}$ ^{52}Cr atomic line, Δ is the detuning of the laser frequency from the atomic resonance, and $I_S = 85$ W/m^2 is the atomic saturation intensity. Using this potential, the Newton equation of motion was integrated for 10^8 random atoms with initial conditions corresponding to the Maxwell-Boltzmann statistics of a thermal chromium beam that is collimated in the transverse directions to 0.3 mrad at full-width at half maximum (FWHM). The "oven" temperature was adjusted to 1900 K. The single-wave, travelling laser power was set to 90 mW. The five laser beams, that create the SW, were all focused down to a $1/e^2$ radius of 200 μm. The ground-state magnetic sublevel structure of ^{52}Cr as well as the presence of other chromium isotopes were taken into account [16].

The atomic flux distributions calculated at the center of the SW are shown in Figs. 8.1(b) and (c) for $\Delta/2\pi = -200$ and 200 MHz, respectively. The corresponding spatial Fourier spectra (or, equivalently, the far-field optical diffraction patterns) are also presented in Fig. 8.1. They clearly exhibit a ten-fold symmetry. We must note here that an experimental structure can differ from these calculations, because in reality it is extremely challenging to obtain a SW profile as that from Fig. 8.1. This is due to the physics of Gaussian laser beams as well as due to unavoidable diffraction on the substrate surface and possible phase fluctuations of the five laser beams. One can, however, approach such an ideal situation by properly tweaking alignment of the experiment. Then, the decagonal symmetry of the structure should become apparent, at least from the spatial Fourier spectra.
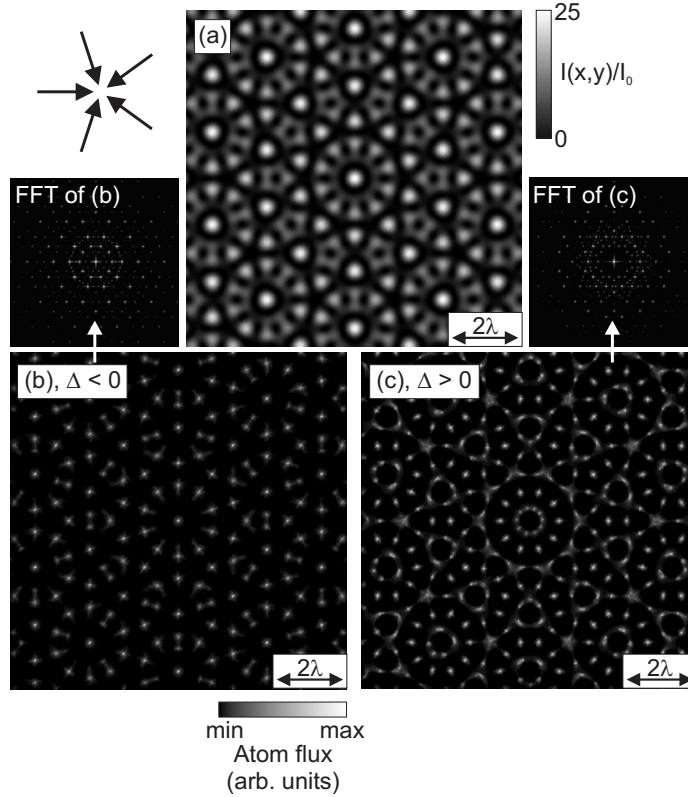
Figure 8.1: Calculation of laser-focused deposition of a chromium beam. (a) Quasiperiodic SW intensity resulting from interference of five laser beams crossing at mutual angles of $72°$. (b,c) Atomic flux distributions for $\Delta < 0$ (b) and $\Delta > 0$ (c). Spatial Fourier spectra of (b) and (c) are also shown. Calculation parameters: $P = 90$ mW, $W_0 = 200$ μm, $|\Delta|/2\pi = 200$ MHz. 10^8 atomic trajectories were traced to obtain these results. For more details, see text.

8.3 Experimental section

For our experiment, laser light at 425.55 nm was obtained by frequency doubling the output of a titanium-doped sapphire laser in an external enhancement doubling cavity [17]. A thermal beam of neutral chromium atoms was produced from a high-temperature effusion cell held at 1900 K. The vacuum pressure during the deposition was below 10^{-8} Pa. After passing a defining diaphragm (1.5×1.5 mm^2), the atomic beam was transversally collimated by means of laser cooling to an FWHM divergence
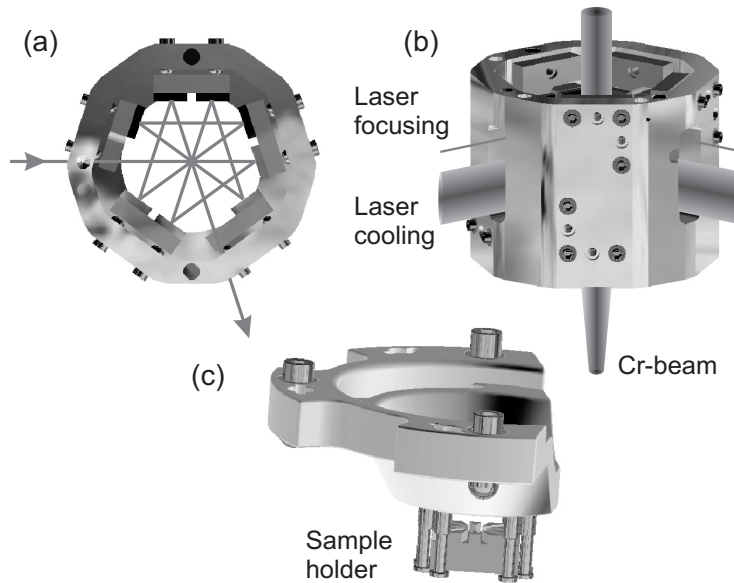
Figure 8.2: *In vacuo* optical setup for fabrication of laser-focused quasiperiodic structures: (a) top view, (b) isometric view, (c) sample holder. The sample holder is placed on top of the unit from (b).

angle of 0.3 ± 0.1 mrad.[1] Then, it was deposited onto a glass-ceramic substrate (rms surface roughness < 5 Å) through a quasiperiodic laser SW. The laser cooling beam and the SW were respectively tuned 10 MHz below and 200 MHz above the involved chromium resonance.

In order to assure mutual phase stability of the five laser beams creating the SW as well as respective alignement between the SW and the laser cooling beam, we designed a monolithic *in vacuo* unit made of high-strength aluminum (Fig. 8.2). Onto this unit eight dielectric mirrors (8 mm wide, 40 mm high) were mounted. These mirrors served to create both the laser molasses and the SW interference pattern. The optical path of the SW laser beam inside the unit is 466 mm. For this long distance, the $1/e^2$ laser beam radius, W_0, should not vary significantly in order to create an optical intensity distribution similar to that from Fig. 8.1(a). In contrast, tight focusing of the SW laser beam is required for high resolution, high contrast fabrication. Both these criteria cannot be realized simultaneously and thus a compromise must be reached.

---

[1]All quoted uncertainties are intended to be interpreted as one standard deviation combined random and systematic errors.

Therefore, we used a spherical lens with a long focal length of 2 m.[2] The SW laser beam was then focused to $W_0 \simeq 200~\mu$m and its confocal distance was $\simeq 340$ mm. It contained a power of 90 mW and was s-polarized.

Using a highly accurate, specially fabricated alignment unit, the mutual angles of $72°$ of the five laser beams were adjusted to within 0.1 mrad. The substrate rested on a glass oblong (cut from a prism with optical quality faces) with grooves for the SW. This oblong was mounted into a holder that fits onto the main monolithic block (Fig. 8.2). The substrate was placed above the center of the SW beam such that only 30% of the total laser power was cut. This arrangement minimizes the diffraction problems and, following atom-optical calculations, still results in a higher density of the atoms near the SW nodes due to the effect of channeling [16]. The deposition time was set to 30 minutes, corresponding to an average thickness of the chromium film of ~ 10 nm.

8.4   Quasiperiodic structures

We investigated the fabricated sample by means of atomic force microscopy (AFM) *ex vacuo*. A surface area of roughly 1.0×1.0 mm^2 exhibited modulation due to the presence of the SW during the deposition. Because at different positions the local intensities of the five laser beams differed, the SW pattern changed and so did also the sample morphology. For example, at those places where two of the five beams were dominant, the resulting structure consisted of nanolines with only a very slight modulation superimposed over them (due to the presence of the other three laser beams with low local intensities). At other places, more than two laser beams dominated and thus the modulation in both spatial directions became more pronounced. A more dot-like structure was grown. Spatial Fourier spectra of all these patterns showed a few very pronounced peaks positioned on circles. The angle spanned by any two of the peaks on the same circle was always an integer multiple of $36°$ to within a measurement uncertainty of $1.0°$.

When the five local intensities were comparable, the surface symmetry and the corresponding Fourier spectrum became almost decagonal. The term "almost decagonal" refers here to the fact that not all the Fourier peaks are equally intense. These decagonal structures covered a surface area of 0.2×0.2 mm^2. In Fig. 8.3(a) an AFM scan of such a structure is shown. From this raw AFM image with no pronounced modulation, the ten-fold symmetry is not immediately apparent. However, a spatial Fourier spectrum calculated from this image, shown in Fig. 8.3(a'), reveals ten clear peaks with different intensities on an inner circle and eight other peaks (plus additional two

---

[2]Alternatively, the SW laser beam could have been refocused within the *in vacuo* optical unit. However, this solution resulted in a considerably more difficult alignment procedure and did not prove to be useful for a first demonstrative set of experiments.
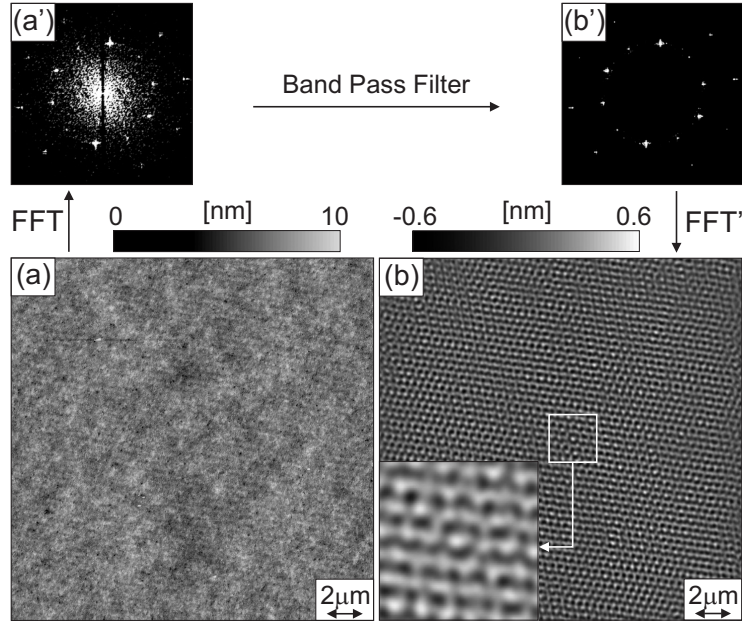
Figure 8.3: Quasiperiodic chromium structures formed by laser-focused atomic deposition. (a) AFM scan of 20×20 μm^2 surface area. (a') Spatial Fourier spectrum of the structure from (a). (b') Filtered spatial Fourier spectrum of (a') – bandpass filter. (b) Inverse spatial Fourier spectrum of (b') – quasiperiodic surface modulation. Inset in (b): Zoom-in view of 2.5×2.5 μm^2 of the surface area enclosed in the white square.

peaks with very low intensities) on an outer circle. The radii of these two circles correspond to wave vectors with magnitudes of 16.82 ± 0.31 μm^{-1} and 27.18 ± 0.31 μm^{-1}, respectively. The ratio of these magnitudes evaluates to 1.614 ± 0.090, well agreeing with the golden ratio of the Fibonnaci sequence of $\simeq 1.618$. In Fig. 8.3(b') a spatial Fourier spectrum "cleaned" from low (background, slow modulation) and high (noise) frequencies, employing a band-pass filter, is presented. An inverse spatial Fourier transform of this last spectrum shows a real space image of the quasiperiodic pattern on the substrate [Fig. 8.3(b)]. We note that the amplitude of the quasiperiodic surface modulation did not exceed 1.2 nm, corresponding to less than 5 monolayers of chromium.

8.5 Summary

In conclusion, we have demonstrated fabrication of quasiperiodic chromium structures on a sub-wavelength scale by means of laser-focused atomic deposition. Our first experiment shows that this atom-optical technique can be mastered to pattern a fairly large surface area with intriguing features that exhibit non-crystallographic symmetry. Although the contrast and the resolution of the sample fabricated by us remained limited, mainly owing to current experimental difficulties, the trend towards a decagonal symmetry is undisputable. Further technical improvements of our *in vacuo* optics will result in a better control of the SW interference pattern – a sharp focus and equal intensities of the laser beams that create it – allowing us to manipulate more efficiently the atomic trajectories in a quasiperiodic optical potential. Then, the result will be a high quality nanostructured array with the desired ten-fold symmetry. The fact that atom-optical deposition is compatible with molecular beam epitaxy, combined with the extreme coherence of the fabrication process, makes it an attractive tool for fabrication of structures for photonic manipulation of light. By this work we added a new dimension to this technique, thereby extending the gallery of its possible applications.

References

[1] M.E. Zoorob and M.D.B. Charlton and G.J. Parker and J.J. Baumberg and M.C. Netti. Complete photonic bandgaps in 12-fold symmetric quasicrystals. *Nature*, 404:740–743, 2000.

[2] J.J. McClelland and W.R. Anderson and C.C. Bradley and M. Walkiewicz and R.J. Celotta and E. Jurdik and R.D. Deslattes. Accuracy of nanoscale pitch standards fabricated by laser-focused atomic deposition. *J. Res. Natl. Inst. Stand. Technol.*, 108:99–113, 2003.

[3] E. Jurdik and J. Hohlfeld and H. van Kempen and Th. Rasing and J.J. McClelland. Laser-focused nanofabrication: Beating of two atomic resonances. *Appl. Phys. Lett.*, 80:4443–4445, 2002.

[4] J.P. Gordon and A. Ashkin. Motion of atoms in a radiation trap. *Phys. Rev. A*, 21:1606–1617, 1980.

[5] G. Timp and R. E. Behringer and D. M. Tennant and J. E. Cunningham and M. Prentiss and K. K. Berggren. Using light as a lens for submicron, neutral-atom lithography. *Phys. Rev. Lett.*, 69:1636–1639, 1992.

[6] J.J. McClelland and R.E. Scholten and E.C. Palm and R.J. Celotta. Laser-focused atomic deposition. *Science*, 262:877–880, 1993.

[7] R.W. McGowan and D.M. Giltner and S.A. Lee. Light force cooling, focusing, and nanometer-scale deposition of aluminum atoms. *Opt. Lett.*, 20:2535–2537, 1995.

[8] F. Lison and H.-J. Adams and D. Haubrich and M. Kreis and S. Nowak and D. Meschede. Nanoscale atomic lithography with a cesium atom beam. *Appl. Phys. B*, 65:419–421, 1997.

[9] R. Gupta and J.J. McClelland and Z.J. Jabbour and R.J. Celotta. Nanofabrication of a two-dimensional array using laser-focused atomic deposition. *Appl. Phys. Lett.*, 67:1378–1380, 1995.

[10] U. Drodofsky and J. Stuhler and Th. Schulze and M. Drewsen and B. Brezger and T. Pfau and J. Mlynek. Hexagonal nanostructures generated by light mask for neutral atoms. *Appl. Phys. B*, 65:755–759, 1997.

[11] R. Gupta and J.J. McClelland and P. Marte and R.J. Celotta. Raman-induced avoided crossings in adiabatic optical potentials: Observation of $\lambda/8$ spatial frequency in the distribution of atoms. *Phys. Rev. Lett.*, 76:4689–4692, 1996.

[12] B. Brezger and Th. Schulze and P.O. Schmidt and R. Mertens and T. Pfau and J. Mlynek. Polarization gradient light masks in atom lithography. *Europhys. Lett.*, 46:148–153, 1999.

[13] M. Mützel and S. Tandler and D. Haubrich and D. Meschede and K. Peithmann and M. Flasphöhler and K. Buse. Atom lithography with a holographic light mask. *Phys. Rev. Lett.*, 88:083601, 2002.

[14] Th. Schulze and B. Brezger and R. Mertens and M. Pivk and T. Pfau and J. Mlynek. Writing a superlattice with light forces. *Appl. Phys. B*, 70:671–674, 2000.

[15] For more details on recent developments in the field of atom-optical nanofabrication, see reviews: D. Meschede and H. Metcalf, J. Phys. D: Appl. Phys. **36**, R17 (2003); M.K. Oberthaler and T. Pfau, J. Phys.: Condens. Matter **15**, R233 (2003).

[16] W.R. Anderson and C.C. Bradley and J.J. McClelland and R.J. Celotta. Minimizing feature width in atom optically fabricated nanostructures. *Phys. Rev. A*, 59:2476–2485, 1999.

[17] E. Jurdik, J. Hohlfeld, A.F. van Etteger, A.J. Toonen, W.L. Meerts, H. van Kempen, and Th. Rasing. Performance optimization of an external enhancement resonator for optical second-harmonic generation. *J. Opt. Soc. Am. B*, 19:1660, 2002.

NINE

Laser manipulation of iron for nanofabrication [1]

Abstract

We fabricate iron nanolines by depositing an atomic beam of iron through a far-off-resonant laser standing-wave (SW) onto a glass-ceramic substrate. The laser SW is tuned 200 MHz above the $^5D_4 \rightarrow {}^5F_5^o$ ^{56}Fe transition at a vacuum wavelength of 372.099 nm. The resulting nanolines exhibit a period of 186 nm, a height above the background of 8 nm and a full-width at half maximum of 95 nm. These nanostructures cover a surface area of $\simeq 1.6 \times 0.4$ mm^2, corresponding to $\simeq 8,600$ iron lines with a length of $\simeq 400$ μm.

9.1 Introduction

One of the most important topics of modern magnetism concerns the fabrication of periodic magnetic nanostructures. These structures constitute model systems for the study of magnetic interactions and switching behavior [1], show novel phenomena like magnetic photonic band gaps [2] and will be required for future magnetic data storage at ultra-high areal densities. Despite the fundamental and technological interest, the fabrication of macroscopic, uniform arrays of well-defined, high-resolution magnetic nanostructures remains a challenge. It is in this spirit that nanofabrication via atom optics attracted our interest as it allows for an inherently parallel, ultra-high vacuum (UHV) compatible fabrication of nanostructures with unprecented periodicity [3, 4].

Nanofabrication via atom optics is based on the interaction between an atomic beam and a far-off resonant laser standing-wave (SW). The atoms, when crossing the

laser SW, experience a spatially-varying optical potential that, in the first approximation, follows the SW intensity profile [5]. When the laser frequency is tuned above (below) an atomic resonance, the atoms gather in the regions of low (high) light intensities. A substrate is then placed into the modulated atomic beam and nanostructures with a subwavelength period are grown. However, the structure width deteriorates fast with an increasing divergence of the atomic beam [6]. Moreover, the SW optical potential is extremely shallow and so the atomic velocities along the SW direction must be low for the atoms to be "trapped" in SW nodes (antinodes). For these two reasons, a high degree of collimation of the atomic beam is required. In practice, laser cooling schemes are applied as they lead to extremely well-collimated atomic beams with no loss of flux [7]. It is this laser cooling requirement that has limited nanofabrication via atom optics to just a few atomic species with a suitable optical transition. So far, laser-focused nanofabrication was demonstrated only with sodium [8], chromium [3] and aluminum [9] and ytterbium [10] in the direct deposition regime, and with cesium [11] via lithography with a self-assembled monolayer as the resist. We note that all these atoms possess a closed (or almost closed) optical transition that allows for efficient laser collimation [7].

In this paper we demonstrate atom-optical nanofabrication with iron. An iron atomic beam is deposited onto a glass-ceramic substrate through a one-dimensional laser SW tuned 200 MHz above the $^5D_4 \rightarrow {}^5F_5^o$ ^{56}Fe transition at a vacuum wavelength of 372.099 nm. The nanoscopically corrugated surface consists of highly-uniform iron nanolines with a period of 186 nm, a full-width at half maximum (FWHM) of 95 nm and a height (above the background) of 8 nm. About 8,600 iron lines with a length of $\simeq 400\ \mu$m are grown in a single deposition run of 30 minutes. We mention here that a different approach to the fabrication of periodic iron nanowires was applied by Tulchinsky *et al.* [12], who employed laser-focused chromium nanolines as a shadow mask for an iron evaporator. In contrast, our nonlithographic approach relies on direct deposition of laser-manipulated iron.

For laser manipulation, iron is a considerably more difficult element than any of the atoms used for atom-optical nanofabrication so far. Naturally occurring isotopes of iron are: ^{54}Fe (abundance 5.8%), ^{56}Fe (91.8%), ^{57}Fe (2.1%) and ^{58}Fe (0.3%). The dominant isotope ^{56}Fe has a nuclear spin $I = 0$ and thus no hyperfine structure. The most suitable optical transition for laser collimation and SW focusing is the $^5D_4 \rightarrow {}^5F_5^o$ resonance with a transition wavelength of $\lambda = 372.099$ nm, a natural linewidth $\Gamma/2\pi = 2.6$ MHz and a saturation intensity $I_S = 62$ W/m^2. However, this is not a closed transition as considerable, dipole-allowed leaks exist from the upper state to the metastable states $^5F_5$ and $^5F_4$. Repumping from these two states back into $^5F_5^o$ at 501.35 nm and 512.88 nm is an option to enhance the collimation efficiency.

9.2   Experiment

For our experiment, the ultraviolet laser light was obtained by frequency doubling the output of a titanium-doped sapphire laser in an external enchancement doubling cavity based on a lithium triborate (LBO) crystal. This optical system for iron was built by upgrading the optics and replacing the LBO crystal in our earlier chromium setup (425 nm $\rightarrow$ 372 nm) [13]. A thermal beam of iron atoms was produced from a high temperature effusion cell held at 2150 K. At these high temperatures iron becomes extremely corrosive and reactive. A beryllium oxide crucible filled with iron powder was used. The fraction of ^{56}Fe atoms that remain in the ground state $^5D_4$ at 2150 K is 46%. The other atoms are thermally excited into the other ^5D levels. The vacuum pressure in the course of deposition was below 10^{-6} mbar. After the iron beam passed a defining diaphragm of 1.5×1.5 mm^2, it entered the deposition chamber.

In the deposition chamber an *in vacuo* optical unit is mounted. It is schematically shown in Fig. 9.1. The required degrees of freedom of the unit are three translations along x, y and z, and two rotations around y and z, respectively. The mirror is a zerodur substrate coated with enhanced aluminum. A glass oblong serves as the sample holder. This oblong was cut from a prism with the right angle specified to within ± 0.015 mrad. The high quality optical faces of the oblong are used as the reference for the angular adjustment of the sample with respect to the mirror. The sample rests on the top face of the oblong. The atom beam is along z and the laser SW along x. Two grooves – one for the atoms and the other one for the laser SW – were cut into the oblong. A quarter-wave ($\lambda/4$) plate is located in front of the mirror at the position where laser collimation takes place. Using this $\lambda/4$-plate a polarization gradient scheme of laser cooling can be created. The optical parts of the *in vacuo* unit are mounted into a holder made of high-strength aluminum that is in turn mounted onto a vacuum manipulator. This manipulator provides all degrees of freedom required to align the experiment.

The laser is stabilized at a frequency near the $^5D_4 \rightarrow {}^5F_5^o$ ^{56}Fe transition for which laser collimation is optimized. In our iron experiment, the detuning from the resonance was determined to $(-2 \pm 0.5)\Gamma$. The frequency stabilization scheme is based on the detection of a laser-induced fluorescence (LIF) signal from the iron beam crossing a probe laser. The fluorescence from the intersection is then imaged onto a split-photodiode that provides a dispersion signal for the locking electronics [6]. The collimation angle of the laser-cooled iron beam was optimized empirically. We found out that the best results were obtained with no polarization gradients and no magnetic fields applied. The laser beam used for cooling contained a power of 24 mW and its $1/e^2$ intensity full-widths were 20 mm along z and 3 mm along y. The fraction of the atomic beam we were able to detect by LIF after cooling exhibited an FWHM collimation angle $\alpha = 0.95 \pm 0.10$ mrad. We note here that these "detectable"
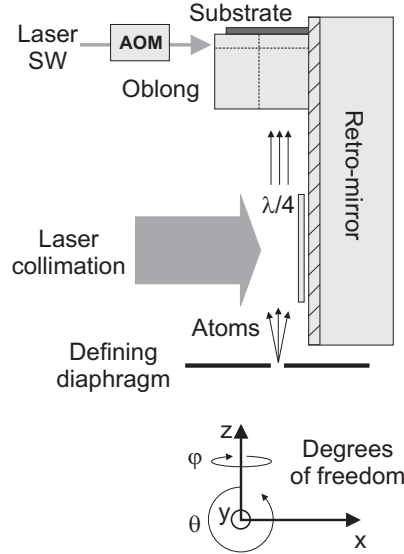
Figure 9.1: *In vacuo* optics including the sample holder. The required degrees of freedom of the unit are also shown.

atoms are those ones that then couple to the SW laser field. No repumping scheme back to $^5F_5^o$ was applied.

The SW laser beam was tuned $\simeq 200$ MHz above the involved iron resonance by an acousto-optic modulator. The SW contained a laser power of 84 mW and was focused down to $1/e^2$ intensity full-widths of $\simeq 200$ μm along y and $\simeq 80$ μm along z. At this SW optical intensity, the effect of the SW on the atoms was clearly visible by LIF-imaging of the iron beam following a free propagation distance of $\simeq 700$ mm from the SW. The *in vacuo* optical unit is moved into the iron beam such that the atoms can pass through the vertical groove in the sample holder (Fig. 9.1). A glass-ceramic substrate was used with a root-mean-square surface roughness of < 5 Å. While the deposition was in progress, the SW was cut by the substrate surface at its center. The deposition time was 30 minutes.

9.3   Iron nanolines

The fabricated sample was subsequently investigated by means of atomic force microscopy (AFM) *ex vacuo*. A 5×5 μm^2 AFM-scan taken at the center of the iron patch is shown in Fig. 9.2(a). A highly-uniform array of iron nanolines with a period of $\lambda/2 \simeq 186$ nm is apparent. In Fig. 9.2(b) a 1×1 μm^2 AFM-scan of the surface area
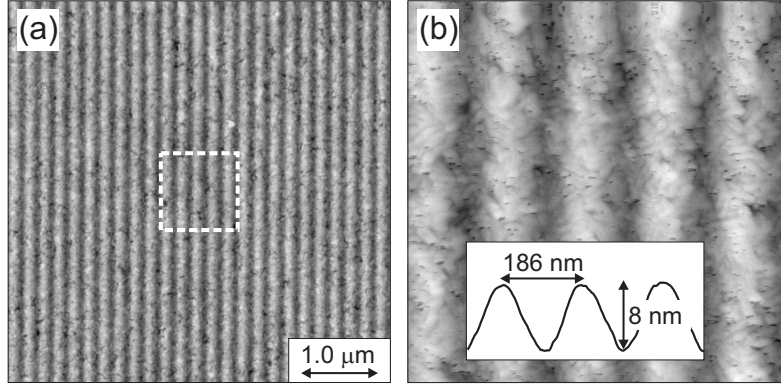
Figure 9.2: Laser-focused nanolines of iron. AFM scans: (a) 5×5 μm^2, (b) 1×1 μm^2. (b) corresponds to the surface area encapsulated in the white square in (a). Inset in (b): Structure profile averaged over 1 μm along the lines.

encapsulated in the white square in Fig. 9.2(a) is presented. The structure profile averaged over 1 μm along the lines is shown in the inset of Fig. 9.2(b). The average structure FWHM and height (above the background) evaluate to $\simeq$ 95 nm and 8 nm, respectively. Neither the images nor the line profiles were corrected for the AFM tip effects as their contribution to the measured structure broadening is estimated to be negligible, akin to earlier studies of laser-focused chromium nanolines by Anderson *et al.* [6]. In addition, the thickness of the background layer was measured to be 25 ± 5 nm using an ellipsometer. This implies a height-to-background ratio of $\simeq$ 1:3.

At this point it is interesting to compare the fabricated nanostructures with the iron flux distribution expected from theoretical considerations. To this end, we calculated the atomic trajectories in a laser SW. The Newton equation of motion with a force due to the SW optical potential was integrated for 10^6 random iron atoms with initial conditions corresponding to the Maxwell-Boltzmann statistics of a thermal (2150 K) iron beam that is collimated in the transverse direction to 0.95 mrad. The laser SW parameters were also set equal to those of the experiment. We estimate that only about 11% of atoms from the iron beam are affected by the SW [1]. The final flux distribution at the substrate surface then exhibits an FWHM of 30 nm and a height-to-background ratio of 1:3. The discrepancy between the measured and mod-

---

[1] About 46% of ^{56}Fe atoms remain in the ground state $^5D_4$ at an oven temperature of 2150 K. Since the probability for the atoms to decay to the metastable states ^5F is 1:243 for every scattered photon, only $\simeq$ 12% of ^{56}Fe atoms leave the laser cooling region in the ground state, provided a completely saturated transition [E. te Sligte *et al.*, Microelectronic Engineering **67-68**, 664 (2003)]. In addition, there are 8.2% of other iron isotopes that do not couple to the SW laser field. This implies that only $\simeq$ 11% of all atoms are affected by the SW.

eled structure widths can most likely be attributed to surface growth effects [6]. In addition to iron-on-substrate and iron-on-iron growth, the presence of different contaminants during the deposition and subsequent investigation of the sample *ex vacuo* could also have contributed to a considerable structure broadening.

We also performed magnetic measurements on the fabricated sample. However, taking into account the large background layer, no signature of individual iron nanolines was expected. Indeed, both magnetic force microscopy and magneto-optical Kerr measurements revealed a ferromagnetic behavior with in-plane easy axis that was independent from the position on the iron patch (irrespective of the presence of nanolines). The drawback of the background layer could be overcome by nanofabrication of magnetic materials with periodically varying composition and thus magnetic properties. This can be achieved by selective manipulation of iron during simultaneous deposition of a number of other species. At this moment, we are performing a study that will allow us to engineer a material with periodically modulated magnetization that might be of interest for applications in magnetic data storage.

9.4   Summary

In conclusion, we have demonstrated nanofabrication via atom optics with iron. The iron nanostructures exhibited a period of 186 nm, a height above the background of 8 nm and an FWHM of 95 nm as determined with an AFM. The thickness of the background layer was estimated to about 25 nm. Considerably narrower structures with a smaller background are feasible from both atom-optical and surface growth perspectives. Repumping from the metastable states ^5F back into the upper atomic level $^5F_5^o$ would certainly help to achieve better collimation angles and higher populations in the ground state $^5D_4$. Then, atom optics would work better and considerably narrower nanostructures could be grown. In addition, experiments carried out in a clean UHV environment would allow for a better control of the surface growth processes with a possibly positive impact on the ultimate abilities of the technique. Probably the most limiting factor of all is the thermal population of the ^5D states, other than the ground state $^5D_4$, at oven temperatures that are required for a reasonably fast experiment. In order to solve this problem a considerable investment into the laser infrastructures would be required that can only hardly be justified at the present stage of development of nanofabrication via atom optics.

We note here that, independently from us, the group of Prof. K.A.H. van Leeuwen from the Eindhoven University of Technology recently succeeded to fabricate iron nanolines via atom optics [14].

References

[1] Z.K. Wang and H.M. Kuok and S.C. Nig and D.J. Lockwood and M.G. Cottam and K. Nielsch and R.B. Wehrspohn and U. Gösele. Spin-wave quantization in ferromagnetic nickel nanowires. *Phys. Rev. Lett.*, 89:027201, 2002.

[2] A. Saib and D. Vanhoenacker-Janvier and I. Huynen and A. Encinas and L. Piraux and E. Ferain and R. Legras. Magnetic photonic band-gap material at microwave frequencies based on ferromagnetic nanowires. *Appl. Phys. Lett.*, 83:2378–2380, 2003.

[3] J.J. McClelland and R.E. Scholten and E.C. Palm and R.J. Celotta. Laser-focused atomic deposition. *Science*, 262:877–880, 1993.

[4] J.J. McClelland and W.R. Anderson and C.C. Bradley and M. Walkiewicz and R.J. Celotta and E. Jurdik and R.D. Deslattes. Accuracy of nanoscale pitch standards fabricated by laser-focused atomic deposition. *J. Res. Natl. Inst. Stand. Technol.*, 108:99–113, 2003.

[5] J.P. Gordon and A. Ashkin. Motion of atoms in a radiation trap. *Phys. Rev. A*, 21:1606–1617, 1980.

[6] W.R. Anderson and C.C. Bradley and J.J. McClelland and R.J. Celotta. Minimizing feature width in atom optically fabricated nanostructures. *Phys. Rev. A*, 59:2476–2485, 1999.

[7] R.E. Scholten and R. Gupta and J.J. McClelland and R.J. Celotta. Laser collimation of a chromium beam. *Phys. Rev. A*, 55:1331–1338, 1997.

[8] G. Timp and R. E. Behringer and D. M. Tennant and J. E. Cunningham and M. Prentiss and K. K. Berggren. Using light as a lens for submicron, neutral-atom lithography. *Phys. Rev. Lett.*, 69:1636–1639, 1992.

[9] R.W. McGowan and D.M. Giltner and S.A. Lee. Light force cooling, focusing, and nanometer-scale deposition of aluminum atoms. *Opt. Lett.*, 20:2535–2537, 1995.

[10] R. Ohmukai, S. Urabe, and M. Watanabe. Atom lithography with ytterbium beam. *Appl. Phys. B*, 77:415–419, 2003.

[11] F. Lison and H.-J. Adams and D. Haubrich and M. Kreis and S. Nowak and D. Meschede. Nanoscale atomic lithography with a cesium atom beam. *Appl. Phys. B*, 65:419–421, 1997.

[12] D.A. Tulchinsky and M.H. Kelley and J.J. McClelland and R. Gupta and R.J. Celotta. Fabrication and domain imaging of iron magnetic nanowire arrays. *J. Vac. Sci. Technol. A*, 16:1817–1819, 1998.

[13] E. Jurdik and J. Hohlfeld and H. van Kempen and Th. Rasing and J.J. McClelland. Laser-focused nanofabrication: Beating of two atomic resonances. *Appl. Phys. Lett.*, 80:4443–4445, 2002.

[14] E. te Sligte, B. Smeets, K.M.R. van der Stam, R.W. Herfst, P. van der Straten, H.C.W. Beijerinck, and K.A.H. van Leeuwen. Atom lithography of Fe. *Appl. Phys. Lett.*, 85:4493–4495, 2004.

Summary

This thesis combines two at first glance different techniques: High Resolution Laser Induced Fluorescence Spectroscopy (LIF) of small aromatic molecules and Laser Focusing of atoms for Nanofabrication.

The main objectives for studying the molecules by LIF were to gain more insight into their structure in both probed by the experiment electronic states (ground – S_0 and first excited – S_1) and explain how the 'molecular shape' changes upon an electronic excitation and what kind of processes the absorption of a photon may trigger. Also other properties of the excited states were probed, like for example their lifetimes or the magnitude and the direction of the transition dipole moment.

In contrast to the 'spectroscopic' part focused more on studying the fundamental properties of the molecules, the 'nanofabrication' experiments were directed more towards application of laser manipulation of atoms by near resonant (laser cooling) and far-of resonant (laser focusing) laser fields to the fabrication of extremely uniformly corrugated surfaces. These deposited structures were hoped to posses some interesting and useful properties like photonic band gap or ferromagnetic properties.

The thesis starts with the introduction to the high resolution LIF technique of small aromatic molecules seeded in molecular beams. It contains a description of the experimental setup and describes the upgrade from the intra-cavity frequency doubling of the 'visible' dye laser to the doubling in an external resonator. This greatly facilitates the experiments by decoupling the dye laser operation from the UV generation step and by increasing the obtained UV power available for the experiment. The latter enables studies of molecules previously unaccessible for the LIF due to their too weak fluorescence signal (like for example bio-molecules). The introduction is closed with the description of the extremely useful method of automated assignment of the rotationally resolved LIF spectra by genetic algorithm (GA).

In the following chapters: 2 to 6, different studies on molecules and molecular clusters are presented, namely the weakly bound van der Waals complexes of tetracene with Ar and Kr atoms (Chapter 2), o-, m-cresols (Chapter 3), p-cresol (4-methylphenol) and its binary water cluster (Chapter 4), resorcinol (Chapter 5) and 4,4′-dimethylaminobenzonitrile (DMABN, Chapter 6). Every molecule presents some interesting points, which are underlined in aforementioned chapters.

Chapter 7 contains an introduction to the laser-focused nanofabrication technique. It briefly describes the used experimental setup, laser cooling and focusing of atoms and it also gives a short overview of what other groups have done in the area. It finishes with some important characteristics of chromium and iron – the elements used by me in the laser-focused nanofabrication experiments.

The last two chapters present nanofabrication of an intriguing quasiperiodic chromium structures (Chapter 8) and extension of the technique to another technologically important material – iron (Chapter 9). Both experiments provided technical challenges and after realization, if still perfected, can promise materials with interesting physical properties: complete photonic band gap – quasiperiodic chromium structures and extremely coherent ferromagnetic iron nanolines.

Acknowledgements

Many people have helped me during my research time in Nijmegen. In particular I would like to thank the following of them:

Erich Jurdik for teaching me a lot about physics and keeping me awaken during the experiments;

Michael Schmitt for his understanding of spectroscopy and a really nice and fruitful time spent in Düsseldorf;

Christian Ratzer for his enthusiasm and speed during our measurements in Düsseldorf;

Alexei Nikolaev and David Pratt for the cooperation on the 'twisted' DMABN molecule;

Izabela Szydłowska, Karen Remmers and Giel Berden for introducing me to the world of high resolution spectroscopy;

Leo Meerts and Theo Rasing for their supervision and the possibility to perform exciting experiments within Molecular & Laser Physics and Solid State Physics II Departments;

   No researcher can work without the help of the technical stuff, which makes possible to build and repair all these small and large, electronic and mechanical devices necessary in the laboratory. Special thanks go to:

Technicians of the Molecular & Laser Physics Department: Cor Sikkens who always had the time to solve my different technical problems, Peter Claus for his touch for the electronics, Leander Gerritsen for the work on the 'cooling box' and Andre van Roij for help with the vacuum system;

Technicians of the Solid State Physics II Department: Albert van Etteger for his knowledge of optics, Tonnie Toonen for always being nice to me and the help with all the mechanical problems I had, Jan Gerritsen for teaching me the secrets of AFM and Jan Hermsen for solving problems with the vacuum system;

Technicians from the 'electronics workshop', especially Peter Dolron for his deep un-

derstanding of electronics and development of the stabilization electronics for the doubling cavity and all others who helped him with the actual realization of that project;

Technicians from the 'mechanical workshop' for the realization of the doubling cavity; Technicians from the 'glass workshop' for their kindness and fast help with fitting crucibles to my oven and making a nice glass nozzles for my spectroscopy experiments;

No PhD student can survive without the everyday help from the secretaries. Many thanks to:

Magda Speijers, Erna Gouwens van Oss, Ine Meijer, Marilou van Bremen and Riki Gommers not only for help with all the papers I had to fill in during my PhD but all their everyday kindness and patience;

I would like to thank all the stuff and PhD students from both Molecular & Laser Physics and Solid State Physics II Departments for a nice atmosphere during my PhD time. Especially, I thank Violetta Bednarska and Anna Zawadzka for discussions not only about the experiments, Stephanie Goldbach-Aschemann for sharing the difficulties in the 'quasi' experiment, Oleg Shklyarevskii for his comments on iron and life, my roommates: Martina Kunze, Hans Naus and Ivo Kalkman for all the time spent together in one room, Ivo I also wish you many successes with 'my old' high resolution setup;

I thank Wiesiek Szweryn for his sincere help at the beginning of my stay in Nijmegen and his advices throughout my PhD time;

Of course I would also like to thank very much my wife Monika and daughter Izabela for their patience, understanding and support.

Grzegorz Myszkiewicz,   Nijmegen, June 2005

Curriculum vitae

Grzegorz Myszkiewicz
born on 29 May 1974
in Warsaw, Poland

1989 – 1993	Prince Józef Poniatowski High School, Warsaw
1993 – 1998	Chemistry studies at University of Warsaw
29 June 1998	'Master of Science' diploma with title:
	'*Ab initio* study of the van der Waals interactions
	between nitric oxide and water'
9 July 1998	Married with Monika Biernacka, Warsaw
1998 – 1999	One year of Ph.D. position at Warsaw University
	within Molecular Spectroscopy Institute
March 1999 – September 1999	Part-time job as an insurance agent;
	sales of the life insurances and pension funds
	of Nationale-Nederlanden Polska S.A.
	(the part of the ING corporation)
2000 – 2004	Ph.D. position at Radboud University Nijmegen,
	research at both: Solid State Physics
	and Molecular and Laser Physics Departments
20 May 2000	Became a happy father of Izabela Myszkiewicz,
	Nijmegen
1 March 2005 –	Postdoc position on the laser nanofabrication project
	in the group of Prof. Theo Rasing,
	Radboud University Nijmegen

Publications

- *Ab initio study for the intermolecular potential of the water – nitric oxide complex.*
  G. Myszkiewicz and J. Sadlej,
  Chemical Physics Letters **318** (2000) 232-239

- *Structure of tetracene – argon and tetracene – krypton complexes from high resolution laser experiments at 450 nm.*
  I. Szydłowska, G. Myszkiewicz and W. L. Meerts,
  Chemical Physics **283** (2002) 371-377

- *Quasiperiodic structures via atom-optical nanofabrication.*
  E. Jurdik, G. Myszkiewicz, J. Hohlfeld, A. Tsukamoto, A. J. Toonen, A. F. van Etteger, J. Gerritsen, J. Hermsen, S. Goldbach-Aschemann, W. L. Meerts, H. van Kempen and Th. Rasing,
  Physical Review B (Rapid Communications) **69** (2004) 201102(R)

- *Laser manipulation of iron for nanofabrication.*
  G. Myszkiewicz, J. Hohlfeld, A. J. Toonen, A. F. van Etteger, O. I. Shklyarevskii, W. L. Meerts, Th. Rasing and E. Jurdik,
  Applied Physics Letters **85** (2004) 3842-3844

- *Twisted intramolecular charge transfer (TICT) states. Rotationally resolved fluorescence excitation spectra of 4,4'-dimethylaminobenzonitrile (DMABN) in a molecular beam.*
  A. E. Nikolaev, G. Myszkiewicz, G. Berden, W. L. Meerts, J. F. Pfanstiel and D. W. Pratt,
  Journal of Chemical Physics **122** (2005) 084309-1–10

- *Rotational isomers of hydroxy deuterated o- and m-cresols studied by ultraviolet high resolution experiments.*
  G. Myszkiewicz, W. L. Meerts, Ch. Ratzer and M. Schmitt,
  Physical Chemistry Chemical Physics **7** (2005) 2142-2150

- *The structure of 4-methylphenol and its water cluster revealed by rotationally resolved UV-spectroscopy using a genetic algorithm approach.*
  G. Myszkiewicz, M. Schmitt, Ch. Ratzer and W. L. Meerts,
  Accepted for publication in Journal of Chemical Physics (2005)

- *Structure determination of resorcinol rotamers by high resolution UV spectroscopy.*
  G. Myszkiewicz, Ch. Ratzer, M. Schmitt and W. L. Meerts,
  Accepted for publication in ChemPhysChem (2005)